Master's thesis

NTNU
Norwegian University of Science and Technology
Faculty of Engineering
Department of Marine Technology

Nicolas Fredhall Holguin

Rigid body modeling and motion control of offshore cranes performing heavy lift operations

Master's thesis in Marine Technology
Supervisor: Eilif Pedersen
June 2019

NTNU
Norwegian University of
Science and Technology

Nicolas Fredhall Holguin

Rigid body modeling and motion control of offshore cranes performing heavy lift operations

Master's thesis in Marine Technology
Supervisor: Eilif Pedersen
June 2019

Norwegian University of Science and Technology
Faculty of Engineering
Department of Marine Technology

NTNU
Norwegian University of
Science and Technology

MASTER'S THESIS IN MARINE CYBERNETICS

SPRING 2019

FOR

STUD. TECH. NICOLAS FREDHALL HOLGUIN

RIGID BODY MODELING AND MOTION CONTROL OF OFFSHORE CRANES PERFORMING HEAVY LIFT OPERATIONS

Work description

During installation of subsea structures or offshore wind turbines, the structure or equipment is lifted off the deck of the installation vessel and lowered through the splash zone and further down to the seabed or hoisted towards the top of the structure for mounting. Safe handling and control of the operation is heavily influenced by weather conditions, integrated vessel and crane dynamics and the motion control and compensation capability of the crane system. Improved motion control for such operations are believed to extend the operability and hence lead to more cost-efficient marine operations. The most common methods for motion control during offshore lifts are the use of tugger wires and tag lines, bumper bars/walls and pivot points.

At the Marine Computational Mechanics Research Lab (MCMR Lab) at the Department of Marine Technology a model crane developed for carrying out heavy lift operations is available. Hence, the purpose of this thesis is to extend the work done in the project thesis and develop simulation models with tugger wire attached to the model crane. A controller scheme should be developed to prevent snap loads and limit the pendulum motion of the payload during heavy lift operations. Furthermore, the mathematical simulation model should be extended to include the additional six degrees of freedom that are present during an offshore operation when the crane is mounted onto a floating vessel. Thereafter, if time permits, tugger winches should be designed and included to the model crane to verify the simulation model.

Scope of work:

- Develop a simulation model of a payload restricted by tugger wires in 3D space.
- Add a tugger wire and winch model into the crane simulation model and implement a controller scheme to prevent snap loads in the system. Ideally pendulum motion should be limited.
- The scaling of dynamic models is of importance and should be investigated.
- Verify the results by comparing the data to a SIMA model provided by Subsea 7.
- Extend the crane simulation model to include the additional six degrees of freedom that would be present when a crane is mounted onto a floating vessel.
- If time permits: Implement the tugger winch system onto the model crane and perform tests to verify the simulation results.

The report shall be written in English and edited as a research report including literature survey, description of mathematical models, description of control algorithms, simulation results, model test results, discussion and a conclusion including a proposal for further work. Source code should be provided on a CD or equivalent with code listing enclosed in appendix. It is supposed that Department of Marine Technology, NTNU, can use the results freely in its research work, unless otherwise agreed upon, by referring to the student's work. The master's thesis report should be submitted in two copies within a date announced by the Department of Marine Technology.

Supervisor: Associate Professor Eilif Pedersen

Trondheim 28.01.19

Eilif Pedersen
Supervisor

Preface

This master's thesis is submitted to the Norwegian University of Science and Technology in fulfillment of one of the requirements for the degree Master of Science in Marine Engineering. The thesis aims to further develop and extend the capabilities of the crane simulation model that is based on the crane available at the Department of Marine Technology. It was written with the intention of presenting a comprehensive introduction to the applied theory and systematic description of the features added to the crane simulation model. The research has been conducted under the supervision of Eilif Pedersen to whom I would like to extend my special thanks for the help and guidance during the completion of the master's thesis. Furthermore, I would like to express my gratitude towards Petter Moen and Øystein Døskeland at Subsea 7 for their support and knowledge related to offshore operations.

Nicolas Fredhall Holguin
Trondheim, June 7, 2019

Abstract

This thesis is a continuation of the work carried out in Gyberg (2017) regarding the modeling of offshore cranes and seeks to further improve the crane simulation model that was developed. Hence, it presents a comprehensive description of the theory that facilitates the extension and development of the simulation model. The additional features include an improved payload model, an inverse dynamics control system, a tugger winch system, and an interconnected crane and vessel dynamics model.

Rigid body assumptions and Lagrangian mechanics lay the foundation for the modeling of the crane, the payload, and the floating vessel, while the wire dynamics are approximated by a series of mass-spring-damper systems. To control the motion of the crane tip, an inverse dynamics controller is designed to calculate the required actuator forces. Tugger winches with active tension control are attached to the payload to prevent snap loads and limit pendulum motion. The coefficients related to the hydrodynamic loads are obtained through available experimental data and methods of approximation. All the models are developed with respect to implementation in a bond graph environment.

A case study is carried out to validate the implemented tugger winch system and to evaluate the performance of the control algorithm. To begin with, the implemented wire dynamics are proven to behave similarly to the acknowledged simulation tool SIMA. It is proven through a comparison of the loads that are induced in two tugger wires during a sea state with $H_s = 2.5m$ and $T_p = 10s$. Then, tension controllers are employed to prevent snap loads, and they show promising results. However, the control algorithm is suboptimal in regard to limiting the pendulum motion of the payload. Hence, more sophisticated controllers are required to both prevent snap loads and limit pendulum motions. Note that due to delays in the progress of the simulation model and in the MCMR Lab, the tugger winch system was not implemented on the model crane in the lab.

A second case study is performed to further extend the simulation model to include the degrees of freedom that are introduced when the crane is mounted onto a floating vessel. The dynamic model of the crane and vessel is developed with the framework of Lagrangian mechanics and is suited to a bond graph environment by applying quasi-coordinates. Relevant hydrodynamic loads such as restoring forces and torques, added mass, damping and wave excitation loads are included in the model. The crane and vessel behavior is compared with data from a ship model in SIMA. With the approximation of hydrodynamic coefficients and ship parameters in mind, the results regarding the model response are deemed satisfactory.

Sammendrag

Denne avhandlingen er en fortsettelse av arbeidet utført i Gyberg (2017) relatert til modellering av offshore-kraner, og har som formål å videreutvikle kransimuleringsmodellen. Derfor presenteres en omfattende beskrivelse av teorien som tilrettelegger for utvidelsen og utviklingen av simuleringsmodellen. Tilleggsfunksjonene inkluderer en forbedret lastmodell, et kranstyringssystem basert på invers dynamikk, et tuggervinsjsystem og en dynamisk modell av et koblet kran- og fartøyssystem.

Stivt legeme-antagelser og Lagrange-mekanikk legger grunnlaget for modelleringen av kranen, lastmodellen, og det flytende fartøyet, mens wiredynamikken er tilnærmet med serier av masse-fjær-demper-systemer. For å kontrollere bevegelsen til krantuppen er en invers dynamikkregulator designet for å kalkulere de nødvendige aktuatorkreftene. Tuggervinsjer med aktiv kraftkontroll er festet til lasten for å forhindre rykklaster og begrense pendelbevegelser. Koeffisientene som er relatert til de hydrodynamiske lastene er gitt av tilgjengelig data fra eksperimenter og approksimeringsmetoder. Alle modellene er utviklet med hensyn til implementering i et miljø tilpasset bond graph modellering.

Et case-studie ble utført for å validere det implementerte tuggervinsjsystemet og for å evaluere ytelsen til kontrollalgoritmen. Den implementerte wiredynamikken viser å samsvare med det velkjente simuleringsverktøyet SIMA. Dette framkommer gjennom en sammenligning av lastene som oppstår i tuggerwirene når de er utsatt for en sjøtilstand med $H_s = 2.5m$ og $T_p = 10s$. Deretter brukes kraftkontrollere til å forhindre rykklaster, og de indikerer lovende resultater. Imidlertid er kontrollalgoritmen ikke gunstig med tanke på å begrense pendelbevegelsen til lasten. Derfor er mer sofistikerte kontrollere nødvendige for å både forhindre rykklaster og begrense pendelbevegelser. Legg merke til at grunnet forsinkelser både i utviklingen av simuleringsmodellen og på MCMR Laben, ble tuggervinsjsystemet ikke implementert på kranmodellen i laben.

Et annet case-studie ble gjennomført for å utvide simuleringsmodellen til å inkludere frihetsgradene som introduseres når kranen monteres på et flytende fartøy. Den dynamiske kran- og fartøysmodellen er utviklet med Lagrange-mekanikk og er tilpasset et bond graph miljø ved bruk av kvasikoordinater. Relevante hydrodynamiske laster som gjenopprettende krefter og momenter, tilleggsmasse, dempning og bølgeeksitasjonskrefter er inkludert i modellen. Kran- og fartøysoppførselen er sammenlignet med data fra en skipsmodell i SIMA. Med tanke på et sett av tilnærmede hydrodynamiske koeffisienter og skipsparametere, er resultatene relatert til modellresponsen ansett som tilfredsstillende.

Contents

List of Figures

List of Tables

1 Introduction

Cranes play a central role in the execution and safety of offshore operations. They are suitable for a wide range of operations such as deck handling, subsea installations, construction work, and ship-to-ship transfer. Due to the vast diversity of offshore operations, there exists a variety of requirements that the cranes must fulfill with respect to a specific task. Therefore, multiple crane types and control schemes are developed by crane suppliers. They are tailored to acquire the required performance for different operations and scenarios. By examining companies that deliver offshore cranes, such as National Oilwell Varco, Palfinger, and Liebherr, it becomes evident that offshore operations are dependent on different crane types. Table 1.1 gives an overview of the offshore cranes that are available from the companies that provide offshore cranes.

Table 1.1: Common crane types

Company	**Available crane types**
National Oilwell Varco	• Stiff boom crane • Knuckle boom crane • Telescopic boom crane • Lattice boom crane • Heavy lift crane
Liebherr	• Stiff boom crane • Knuckle boom crane • Heavy lift crane • Lattice boom crane
Palfinger	• Stiff boom crane • Knuckle boom crane • Telescopic boom crane • Lattice boom crane • Travelling cranes

With respect to the model crane available at the Marine Computational Mechanics Research Lab (MCMR Lab) at the Department of Marine Technology, stiff boom cranes, telescopic boom cranes, and knuckle boom cranes are of relevance. These crane types are mounted to ships on rotating platforms, and the crane arms and platform are positioned with the use of hydraulic actuators. The telescopic boom cranes and knuckle boom cranes differ from the stiff boom cranes with their additional degree of freedom. In addition to rotation and adjustable inclination, a telescopic boom crane can increase its operational radius by extending the length of its crane boom. This allows it to obtain an increased operational radius without occupying extra space on the vessel. When it comes to the knuckle boom crane, instead of an extendable crane boom, it consists of two connected crane booms that both can adjust their inclination independent of each other. Therefore, in addition to

an increased operational radius similar to the telescopic boom crane, the knuckle boom crane is foldable and occupies less space on deck. All crane types utilize a winch in combination with the movement of the crane booms to move and position the payload towards the desired location.

(a) Stiff boom crane

(b) Telescopic boom crane

(c) Knuckle boom crane

Figure 1.1: Common crane types

Due to environmental loads acting on the vessel, such as wind, waves and current, six degrees of freedom motion is induced on the floating vessel. Evidently, the motion affects the crane movement and payload behavior. Traditionally, the offshore crane lift operations are performed manually through input from the crane operator and crew. Hence, the seas states that are permitted when carrying out an offshore operation are influenced by the skill of the crane operator. Therefore, crane suppliers provide different control techniques to autonomously compensate for the vessel motion and limit the pendulum motion of the payload. Conventional control techniques consist of active and passive heave compensation, active and passive constant tension, and auxiliary tugger winch systems. Note that the control method that is employed in this thesis to limit the pendulum motion is the inclusion of tugger winch systems. However, a combination of different control techniques could provide an optimal performance regarding the restriction of the payload motion. Hence, the concepts revolving heave compensation and constant tension are presented in Section 2.5. The inclusion of control systems provides additional safety, efficiency, and accuracy during offshore operations. Furthermore, it limits the likelihood of human errors.

In relation to the tugger winch systems, it is important to monitor the loads that are induced in the tugger wires. With varying loads due to the six degrees of freedom pendulum motion of the payload, the tugger wires fluctuate in between slack and engaged configurations. Note that the slack configuration appears due to the wires inability to take on pressure loads. Consequently, the occurrence of snap loads is a common issue when the payload motion is restricted by tugger wires. The snap loads are characterized by a spike in tension over a short period of time when a slack wire reengages tension. These spikes in tension can cause the wires to break and lead to dangerous situations during offshore operations. Thus, the tugger winch systems must be designed with the ability to pay in and out wire in accordance with the tension levels that are present in the tugger wires. By controlling the tension in the wires, snap loads are prevented by avoiding slack wire configurations. Hence, by attaching controlled tugger wires to the payload to limit the pendulum motion, offshore operations can be performed in even rougher sea states.

In Gyberg (2017), a model crane was designed and built in the Marine Computational Mechanics Research Lab (MCMR Lab) at the Department of Marine Technology (IMT). The design was developed such that the model crane could be modified to behave similarly to either of the previously stated crane types. Considering that the current configuration is as a knuckle boom crane, the previously developed crane simulation models are designed accordingly. The first step in this thesis is to implement tugger wires and develop a control system that prevents snap loads and limits the pendulum motions of the payload. Consequently, it is important to implement a wire model that reflects the dynamics of a real wire. Therefore, the wire models are based on proven mathematical

models and are verified through a comparison with data from the acknowledged simulation tool SIMA. Note that the inclusion of tugger winch systems and their impact on the crane system is the focus in the development of the crane simulation model that is evaluated in this master's thesis. Furthermore, the crane simulation model is extended to include the six degrees of freedom that are introduced when the crane is mounted onto a floating vessel. That implies that the interconnected dynamics of the crane and vessel system are derived in addition to the effect of hydrodynamic loads.

1.1 Exposition of the problem

The research conducted in this thesis is intended to further develop the simulation models that have been made in accordance with the model crane in the MCMR Lab. Hence, the previously applied dynamics related to the crane, wires, and payloads will be examined and necessary improvements are carried out. In that regard, Lagrangian mechanics and wire modeling are essential topics of the thesis. Note that all the different models will be developed in a bond graph environment.

After evaluating the available simulation model, tugger winch systems will be implemented to limit the motion of the payload while preventing snap loads from appearing in the tugger wires. The payload will be modeled as a rigid body attached to the main wire of the crane. To validate the results, a simulation model of an offshore operation is provided by Subsea 7 in the SIMA software. The parameters in the crane simulation model will be adjusted to comply with the SIMA model. Note that the ship modeled in SIMA is given in full-scale. Hence, scaling laws are proposed and implemented to ensure that the dynamic response is correct in the model scale that is related to the model crane in the MCMR Lab. Furthermore, considering that the model crane in the MCMR Lab is fixed to the floor, the motion in six degrees of freedom must be imitated by moving the crane tip similarly to the data retrieved from the SIMA model. All the steps in the derivation of the simulation model and the simplifications that are applied during the testing are presented in this thesis.

A combined vessel and crane simulation tool is proposed in relation to the limitations of the model crane regarding motion in six degrees of freedom. Hence, the crane simulation model is extended to account for the motion in six degrees of freedom that is induced by hydrodynamic loads. The results are verified through a comparison of the developed simulation model and the SIMA model provided by Subsea 7. Note that deviations are expected since not all parameters are available and because that the implementation of the hydrodynamic loads is simplified.

1.2 Related work

In the development of the simulation models, a variety of important references are utilized. The theory regarding rigid body modeling and the framework of the Lagrangian mechanics is based on the work done in Ginsberg (1995) and Siciliano et al. (2009). Furthermore, the application of Lagrangian mechanics in the development of the crane simulation model is inspired by the previous master's theses Gyberg (2017) and Rokseth (2014). The theory regarding bond graph modeling is taken from Pedersen and Engja (2014) and Borutzky (2010). They provided insight into the fundamental concepts of bond graph modeling and the design of models in different physical disciplines. When developing wire models for the system, the work carried out in Skjong and Pedersen (2014) and Pedersen and Pedersen (2005) are the main sources of information. Regarding scaling laws, Groesen and Molenaar (2007) and Ghosh (2011) provide the basic concepts related to the scaling of dynamic systems. All the previously mentioned sources of information are central to the development of the crane simulation model.

When deploying the crane onto a floating vessel, the interaction between the fluid and rigid body system is based on the theory presented in Faltinsen (1990) and Fossen (2011). They provide the theory regarding hydrodynamic loads and methods for approximating their magnitudes. Furthermore, Rokseth et al. (2017) provide the procedure related to the extension of a crane model to include the combined vessel and crane dynamics. It presents the application of quasi-coordinates to simplify the process of implementing the system dynamics in a bond graph environment. The previously mentioned references are crucial in regard to understanding and implementing the combined crane and vessel system dynamics.

1.3 Structure of the thesis

This section provides a brief description of the main topics contained in the chapters that are presented in this thesis. Hence, an overview of the structure and progression of the thesis is given below.

Chapter 2 provides an introduction to rigid body modeling, Lagrangian mechanics, bond graph modeling, hydrodynamic loads, wire modeling and motion compensation methods. It presents the theory that is applied in the development of the simulation models.

Chapter 3 shows the implementation of the crane simulation model and is based on the method presented in Gyberg (2017). It provides insight into the inner working of the previously developed crane simulation model.

Chapter 4 presents a case study where the crane simulation model is compared to an offshore operation in an attempt to verify the implemented tugger winch system. A rigid body payload model, reference model, inverse dynamics controller, and tension controllers are implemented to imitate the offshore operation with the limitations of the model crane in mind.

Chapter 5 extends the crane simulation model to include the six degrees of freedom that are introduced when the crane is mounted on a floating vessel. Combined vessel and crane dynamics are developed and hydrodynamics loads are included in the model.

Chapter 6 concludes the work carried out in the thesis and suggests further work regarding improvements of the simulation models and model crane.

2 | Background material

The purpose of this chapter is to give an overview of the theory that is utilized when developing a mathematical model of a crane and its auxiliary equipment. Since the model crane available at the MCMR Lab currently is configured as a knuckle boom crane, this is the crane type that will be of interest. Considering that the model crane has been the main focus of the previous master's theses Gyberg (2017) and Evang (2017), a crane simulation model has already been developed. However, the modeling approach and theory will be presented and explained to give insight to the inner workings of the modeling procedure. Furthermore, another evaluation of the relevant theory could lead to improvements in the development of the simulation model.

2.1 Rigid body modeling

To fully develop the dynamics of the crane model, both the kinematics and kinetics of the crane must be derived. Kinematics is the description of the path, position, velocity, and acceleration of a point or a body when disregarding the forces that caused the motion. Kinetics is the description of bodies and the forces that act on them. It is most often described by classical mechanics with Newton's second law or through the use of Lagrangian mechanics. Since Lagrangian mechanics are applied to describe the crane dynamics in this thesis, it is important to note that positions and velocities of particular interest are those at the joints and centers of gravity of the crane components. These positions and velocities will be expressed as functions of a set of generalized coordinates. In addition, the positions where loads are applied to the system are of interest when expressing the generalized forces that act on the system.

2.1.1 Rigid body kinematics

The different parts of a crane are most often characterized by a set of rigid bodies. This assumption is a simplification since all materials deform when forces are applied to them. However, the rigid body assumption is useful when the motion of the object due to deformations is negligible compared to its total movement (Ginsberg, 1995). To show the usefulness of this assumption, the equations describing the position, velocity, and acceleration of a point in a moving frame relative to an inertial reference frame are shown below

$$\begin{aligned}
\mathbf{r}^0_{p/0} &= \mathbf{r}^0_{1/0} + \mathbf{r}^0_{p/1} \\
\mathbf{v}^0_{p/0} &= \mathbf{v}^0_{1/0} + \mathbf{v}^0_{p/1} + \boldsymbol{\omega}^0_{1/0} \times \mathbf{r}^0_{p/1} \\
\mathbf{a}^0_{p/0} &= \mathbf{a}^0_{1/0} + \mathbf{a}^0_{p/1} + \boldsymbol{\alpha}^0_{1/0} \times \mathbf{r}^0_{p/1} + \boldsymbol{\omega}^0_{1/0} \times (\boldsymbol{\omega}^0_{1/0} \times \mathbf{r}^0_{p/1}) + 2\boldsymbol{\omega}^0_{1/0} \times \mathbf{v}^0_{p/1}
\end{aligned} \tag{2.1}$$

Here $\mathbf{r}$ is a position vector, $\mathbf{v}$ a velocity vector, $\mathbf{a}$ an acceleration vector, $\boldsymbol{\omega}$ a rotational velocity vector, and $\boldsymbol{\alpha}$ a rotational acceleration vector. The notation $\mathbf{x}^i_{j/k}$ indicates that the vector $\mathbf{x}$ is given in reference frame i where j is a point relative to the origin of reference frame k. In this

case, the 0-frame is the inertial frame while the 1-frame is some arbitrary moving frame. The point moving in the 1-frame is denoted p.

If the point p is located at a rigid body, the velocity of the point relative to the moving frame that is attached to the rigid body will be zero with the assumption of no deformation. This implies that $\mathbf{v}^1_{p/1} = 0$ and $\mathbf{a}^1_{p/1} = 0$, and consequently $\mathbf{v}^0_{p/1} = 0$ and $\mathbf{a}^0_{p/1} = 0$ since they are related through a coordinate transformation, which will be discussed in the next section. The previous equations are therefore simplified to the general expressions of a point on a rigid body expressed in an inertial reference frame.

$$\begin{aligned}
\mathbf{r}^0_{p/0} &= \mathbf{r}^0_{1/0} + \mathbf{r}^0_{p/1} \\
\mathbf{v}^0_{p/0} &= \mathbf{v}^0_{1/0} + \boldsymbol{\omega}^0_{1/0} \times \mathbf{r}^0_{p/1} \\
\mathbf{a}^0_{p/0} &= \mathbf{a}^0_{1/0} + \boldsymbol{\alpha}^0_{1/0} \times \mathbf{r}^0_{p/1} + \boldsymbol{\omega}^0_{1/0} \times (\boldsymbol{\omega}^0_{1/0} \times \mathbf{r}^0_{p/1})
\end{aligned} \tag{2.2}$$

2.1.2 Rotational matrices

As previously mentioned, there is a relationship between the inertial reference frame and the moving body-fixed frame that can be expressed through a coordinate transformation. In Equation 2.2, the position vector that describes the position of point p relative to the origin of the body-fixed frame is most often found in the body-fixed frame due to its simplicity. It is then transformed into the inertial frame by coordinate transformations. When operating in the three-dimensional space, there are three axes of rotation, indicating that a body-fixed frame needs a set of rotational transformations into the inertial frame. In this thesis, the Euler angles ϕ, θ, and ψ are used in the transformation, but other approaches such as the use of unit quaternions are viable. Note that the Euler angles are intuitive to work with as opposed to the quaternions. The simplicity of applying the Euler angles comes with a cost as there exists a singularity when the pitch angle is at $\pm 90°$, in which case the yaw angle is not defined. This singularity is often referred to as the gimbal lock (Beard, 2012). The singularity is avoided by applying quaternions (Fossen, 2011), but the Euler angles suffice by assuming that the pitch angles are within a range that does not include the value that causes the singularity.

With Euler angles, the coordinate transformation is done through three basic rotations around the three coordinate axes z, y and x independently of each other. To follow the zyx convention, the rotation transformation starts with the z-axis, continues with the y-axis and ends with the x-axis. These rotations are shown in Figure 2.1, where the three Euler angles are used to move from reference frame 0 to reference frame 1. The matrices of the principal rotations in the counter clockwise direction are shown in Equation 2.3.

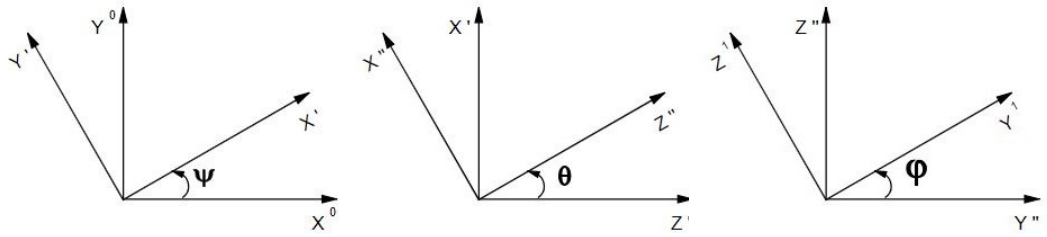

(a) Rotation about the z^1 axis (b) Rotation about the y' axis (c) Rotation about the x" axis

Figure 2.1: Visualization of the rotational transformation

$$\mathbf{R}_z(\psi) = \begin{bmatrix} c\psi & -s\psi & 0 \\ s\psi & c\psi & 0 \\ 0 & 0 & 1 \end{bmatrix}, \quad \mathbf{R}_y(\theta) = \begin{bmatrix} c\theta & 0 & s\theta \\ 0 & 1 & 0 \\ -s\theta & 0 & c\theta \end{bmatrix}, \quad \mathbf{R}_x(\phi) = \begin{bmatrix} 1 & 0 & 0 \\ 0 & c\phi & -s\phi \\ 0 & s\phi & c\phi \end{bmatrix} \tag{2.3}$$

Here $c(\cdot) = cos(\cdot)$ and $s(\cdot) = sin(\cdot)$. Looking back at the position vector $\mathbf{r}^0_{p/1}$ in Equation 2.2, it can be expressed through $\mathbf{r}^1_{p/1}$ by rotating it from the body-fixed frame into the inertial frame as follows

$$\mathbf{r}^0_{p/1} = \mathbf{R}_z(\psi)\mathbf{R}_y(\theta)\mathbf{R}_x(\phi)\mathbf{r}^1_{p/1} = \mathbf{R}(\Theta)^0_1 \cdot \mathbf{r}^1_{p/1} \tag{2.4}$$

Another interesting aspect of the rotation matrices is their orthonormality. It implies that they satisfy the equation $\mathbf{R}^T\mathbf{R} = \mathbf{R}\mathbf{R}^T = I_{3x3}$, which furthermore implies that $\mathbf{R}^T = \mathbf{R}^{-1}$ (Ginsberg, 1995). With this, Equation 2.4 can be inverted to perform the transformation from the inertial frame to the body-fixed frame, as shown in Equation 2.5.

$$\mathbf{r}^1_{p/1} = \mathbf{R}^T(\Theta)^0_1 \cdot \mathbf{r}^0_{p/1} = \mathbf{R}(\Theta)^1_0 \cdot \mathbf{r}^0_{p/1} \tag{2.5}$$

Hence, any two reference frames can be related to each other. A rotation transformation is thus a powerful tool when analyzing the kinematics of a system with the use of Lagrangian mechanics.

The derivative of a rotation matrix

Since a rotation matrix most often depends on time-varying angles, it is of interest to derive its time derivative. By utilizing the orthonormal property of the rotation matrix, the time derivative can be written as

$$\dot{\mathbf{R}}(\boldsymbol{\Theta})^0_1\mathbf{R}^T(\boldsymbol{\Theta})^0_1 + \mathbf{R}(\boldsymbol{\Theta})^0_1\dot{\mathbf{R}}^T(\boldsymbol{\Theta})^0_1 = \mathbf{0} \tag{2.6}$$

Since the sum of the two terms generated by the time derivative of the rotation matrix is equal to zero while being the transpose of one another, they are by definition skew-symmetric matrices

$$\mathbf{S}(\boldsymbol{\omega}^0_{1/0}) + \mathbf{S}^T(\boldsymbol{\omega}^0_{1/0}) = \mathbf{0} \Rightarrow \mathbf{S}(\boldsymbol{\omega}^0_{1/0}) = \dot{\mathbf{R}}(\boldsymbol{\Theta})^0_1\mathbf{R}^T(\boldsymbol{\Theta})^0_1 \tag{2.7}$$

where the skew-symmetric matrix is defined as below

$$\mathbf{S}(\boldsymbol{\omega}^0_{1/0}) = \begin{bmatrix} 0 & -\omega_3 & \omega_2 \\ \omega_3 & 0 & -\omega_1 \\ -\omega_2 & \omega_1 & 0 \end{bmatrix}, \quad \boldsymbol{\omega}^0_{1/0} = [\omega_1, \omega_2, \omega_3]^T \tag{2.8}$$

By post-multiplying the rotation matrix to the expression in Equation 2.7, it is shown that the time derivative of the rotation matrix is related to the rotation matrix itself through the skew-symmetric operator $\mathbf{S}(\boldsymbol{\omega})$

$$\dot{\mathbf{R}}(\boldsymbol{\Theta})^1_0 = \mathbf{S}(\boldsymbol{\omega}^0_{1/0})\mathbf{R}(\boldsymbol{\Theta})^1_0 \tag{2.9}$$

Furthermore, it is stated in Siciliano et al. (2009) that the following relation holds for a rotation matrix

$$\mathbf{R}(\boldsymbol{\Theta})_0^1 \mathbf{S}(\boldsymbol{\omega}_{1/0}^0)\mathbf{R}^T(\boldsymbol{\Theta})_0^1 = \mathbf{S}(\mathbf{R}(\boldsymbol{\Theta})_0^1 \cdot \boldsymbol{\omega}_{1/0}^0) \tag{2.10}$$

which is a useful definition later on.

2.1.3 Lagrangian mechanics

The equations of motion of a system of rigid bodies can be derived by Lagrange's equations. It is an energy-based formulation that looks at the kinetic and potential energy of a system. Since Lagrange derived the equations directly from Newton's laws (Ginsberg, 1995), the importance of the coordinate transformations comes to light. Newton's laws only hold in inertial reference frames, meaning that the motion of a body must be referenced to a fixed reference frame (Beard, 2012). In the same manner, Lagrangian mechanics requires that all the positions and velocities are given in an inertial reference frame when calculating the kinetic and potential energy of a system. Furthermore, the velocities and positions must be expressed in terms of the selected generalized coordinates $\mathbf{q}_i$, $i = 1, 2, ..., k$, where k is the number of generalized coordinates. Moreover, the forces acting on the system must be defined as generalized forces. Hence, the following sections explain the basic concepts related to the derivation of the equations of motion of a general system through the use of Lagrangian mechanics.

Generalized coordinates

Firstly, a set of parameters are defined such that the position and orientation of the system are uniquely described. This requires that the number of generalized coordinates as a minimum is equal to the number of degrees of freedom in the system. In the case where number of generalized coordinates exceeds the number of degrees of freedom, the generalized coordinates are constrained. This implies that the generalized coordinates must satisfy additional conditions to those that arise from the kinetics principles (Ginsberg, 1995). These constraints could be configuration constraints that limit the overall position the system can obtain and velocity constraints that limit the velocity the system can have in a given configuration. In general, the number of constraint equations can be found by the definition

$$\eta_{dof} = \eta_{ce} - \eta_{gc} \tag{2.11}$$

where η_{gc}, η_{dof} and η_{ce} are the number of generalized coordinates, degrees of freedom and constraint equations, respectively (Rokseth, 2014). It should be noted that the chosen generalized coordinates are not a unique set, implying that other parameters could describe the system equally well. Therefore, the choice of generalized coordinates should be taken into careful consideration when describing the system to make the process as simple as possible.

Potential and kinetic energy of rigid bodies

As previously mentioned, Lagrangian mechanics are based on the potential and kinetic energy of a system. Furthermore, a set of generalized coordinates given in the same reference frame must define the system. A rigid body can have both linear and rotational velocity, meaning that each component will have two terms representing its kinetic energy. In Ginsberg (1995) it is shown that the position vector $\mathbf{r} = \mathbf{r}(q_1, ...q_k, t)$ is a function of the generalized coordinates and time. The velocity vector $\mathbf{v} = \mathbf{v}(q_1, ..., q_k, \dot{q}_1, ..., \dot{q}_k, t)$ is given by the generalized coordinates, the generalized velocities and time. In that regard, the potential and kinetic energy of a system of $j = 1, .., n$ rigid

bodies are explicit functions of the generalized coordinates $\mathbf{q}_i$, the generalized velocities $\dot{\mathbf{q}}_i$ and the time t. The kinetic and potential energy is expressed as follows

$$\begin{aligned} T_j(\mathbf{q}, \dot{\mathbf{q}}, t) &= \frac{1}{2} m_j \mathbf{v}^T(\mathbf{q}, \dot{\mathbf{q}})^0_{cg_j/0} \mathbf{v}(\mathbf{q}, \dot{\mathbf{q}})^0_{cg_j/0} + \frac{1}{2} \boldsymbol{\omega}^T(\mathbf{q}, \dot{\mathbf{q}})^0_{j/0} \mathbf{I}^0_j \boldsymbol{\omega}(\mathbf{q}, \dot{\mathbf{q}})^0_{j/0} \\ T(\mathbf{q}, \dot{\mathbf{q}}, t) &= \sum_{j=1}^{n} T_j(\mathbf{q}, \dot{\mathbf{q}}, t) \end{aligned} \tag{2.12}$$

$$V(\mathbf{q}, t) = \sum_{j=1}^{n} (m_j \mathbf{g}^T \mathbf{r}(\mathbf{q})^0_{cg_j/0}) + f(\mathbf{q}) \tag{2.13}$$

Here cg_j, m_j, and I^0_j are referring to the center of gravity, the mass and the inertia tensor, given in the inertial frame, of the jth rigid body, respectively. $f(\mathbf{q})$ is a function that takes into account the energy that the system can store as potential energy, e.g. in springs, and $\mathbf{g}^T = [0 \ 0 \ -g]$ contains the gravitational acceleration.

Inertia tensor

The inertia tensor of a rigid body is constant when it is given in a body-fixed frame, but is dependent on the body configuration in an inertial frame (Sciavicco and Siciliano, 2000). It can be shown that the inertia tensor given in a body-fixed frame can be related to an inertial reference frame through the following rotation transformation

$$\mathbf{I}^0_j = \mathbf{R}(\Theta)^0_j \mathbf{I}^j_j \mathbf{R}^T(\Theta)^0_j = \mathbf{R}(\Theta)^0_j \mathbf{I}^j_j \mathbf{R}(\Theta)^j_0 \tag{2.14}$$

where $\mathbf{I}^j_j$ and $\mathbf{I}^0_j$ are the inertia tensors defined in the center of gravity of the jth rigid body in the body-fixed frame and the inertial frame, respectively. $\mathbf{R}(\Theta)^0_j$ is the rotation matrix between the body-fixed frame and inertial frame.

Generalized forces

To develop the equations of motion of the system, in addition to the potential and kinetic energy, the generalized forces acting on the system must be defined. In Ginsberg (1995), a generalized force Q_i is derived by giving an arbitrary particle a virtual displacement δr and then evaluating the virtual work δW done by the forces $\mathbf{F}_j$ acting on the particle. These forces are represented by dissipative forces, which in classical dynamics are defined as "all types of interactions where the energy is lost when motion takes place" (Razavy, 2006), e.g. friction. The virtual work is found by taking the dot product of the virtual displacement with the sum of the dissipative forces acting on the particle (Ginsberg, 1995)

$$\delta W = \left(\sum F \right) \cdot \delta r \tag{2.15}$$

The virtual displacement due to the dissipative forces is related to the virtual displacement in the generalized coordinates and is given as follows (Ginsberg, 1995)

$$\delta r = \sum_{i=1}^{n} \frac{\partial r}{\partial q_i} \delta q_i \tag{2.16}$$

The virtual work done by the dissipative forces can additionally be described in terms of the generalized forces since they are defined as the coefficients of the corresponding increments δq_i (Ginsberg, 1995)

$$\delta W = \sum_{i=1}^{n} Q_i \delta q_i \tag{2.17}$$

Hence, the expression of the generalized force due to dissipative forces is given as follows

$$Q_i = \left(\sum F \right) \cdot \frac{\partial r}{\partial q_i} \tag{2.18}$$

2.1.4 Lagrange's equation of motion

When the potential energy, kinetic energy, and the generalized forces have been defined, the equations of motion of the system are found through Lagrange's equation of motion, as derived from Hamilton's principle in Ginsberg (1995).

$$\frac{d}{dt}\left(\frac{\partial T}{\partial \dot{q}_i}\right) - \frac{\partial T}{\partial q_i} + \frac{\partial V}{\partial q_i} = Q_i, \ i = 1, 2, ..., k \tag{2.19}$$

From Equation 2.19 it becomes obvious that the number of second order differential equations correspond to the number of generalized coordinates. If the number of generalized coordinates is equal to the number of degrees of freedom in the system, the number of equations of motion corresponds to the minimum number of equations required to solve the problem.

2.1.5 Jacobian matrix

It was stated that the position vector $\mathbf{r}$ is a function of the generalized coordinates, meaning that it can be expressed as shown in Equation 2.20.

$$\mathbf{r}^0_{p_j/0} = f_j(\mathbf{q}) \tag{2.20}$$

Here the point of interest is referred to an inertial reference frame by applying the previously defined notations. By employing the chain rule when taking the derivative of the position vector with respect to time, the relationship between the linear velocities of a point on the rigid body j and the generalized coordinates are obtained as follows

$$\mathbf{v}^0_{p_j/0} = \dot{\mathbf{r}}^0_{p_j/0} = \frac{\partial f_j(\mathbf{q})}{\partial \mathbf{q}} \dot{\mathbf{q}} = \mathbf{J}_{v_{p_j}}(\mathbf{q}) \dot{\mathbf{q}} \tag{2.21}$$

Here $\mathbf{J}$ is the Jacobian matrix that defines the transformation between the generalized coordinates and the linear velocities. Similarly to the linear velocities, the rotational velocities are related to the generalized coordinates through a Jacobian matrix as follows

$$\boldsymbol{\omega}^0_{j/0} = \mathbf{J}_{\omega_j}(\mathbf{q}) \dot{\mathbf{q}} \tag{2.22}$$

Open chain of linked rigid bodies

Cranes are frequently compared to a robot manipulator that consists of rigid bodies connected through joints. Therefore, inspired by robot arm theory, a general expression of the Jacobian matrix is developed. Since the velocities at the centers of gravity are required in the equations of motion, the expression in Equation 2.1 is used as a basis for finding the Jacobian matrix. By defining the arbitrary point p as the center of gravity of the jth rigid body, the expression becomes

$$\begin{aligned} \mathbf{r}^0_{cg_j/0} &= \mathbf{r}^0_{j/0} + \mathbf{r}^0_{cg_j/j} \\ \mathbf{v}^0_{cg_j/0} &= \mathbf{v}^0_{j/0} + \mathbf{v}^0_{cg_j/j} + \boldsymbol{\omega}^0_{j/0} \times \mathbf{r}^0_{cg_j/j} \end{aligned} \tag{2.23}$$

The first term is the linear velocity of the system at joint i. Consequently, the first term can be expanded and related to each rigid body prior to the jth rigid body until the last body is reached. This is shown in the general expression given in Equation 2.24, which is derived from a generic rigid body in the open chain of links. An arbitrary rigid body in the open chain of links is illustrated in Figure 2.2.

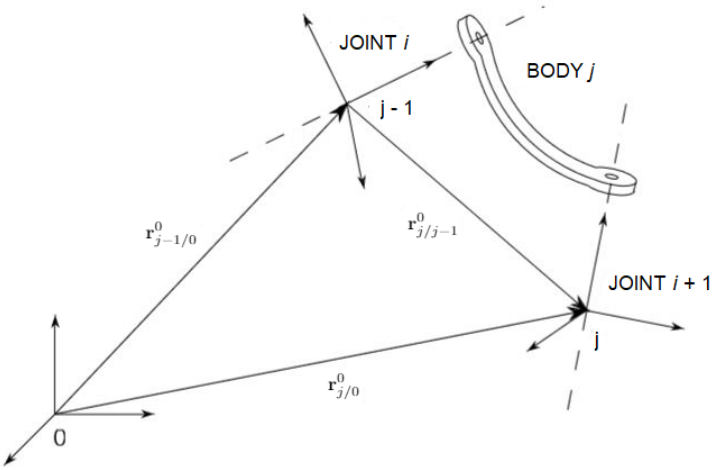

Figure 2.2: Generic rigid body in an open chain of links.
Taken from Siciliano et al. (2009)

$$\begin{aligned} \mathbf{r}^0_{j/0} &= \mathbf{r}^0_{j-1/0} + \mathbf{r}^0_{j/j-1} \\ \mathbf{v}^0_{j/0} &= \mathbf{v}^0_{j-1/0} + \mathbf{v}^0_{j/j-1} + \boldsymbol{\omega}^0_{j-1/0} \times \mathbf{r}^0_{j/j-1} \end{aligned} \tag{2.24}$$

The angular velocity is derived by examining the rotation composition (Siciliano et al., 2009)

$$\mathbf{R}^0_j = \mathbf{R}^0_{j-1}\mathbf{R}^{j-1}_j \tag{2.25}$$

By taking the time derivative, the following is shown by applying Equation 2.9

$$\mathbf{S}(\boldsymbol{\omega}^0_{j/0})\mathbf{R}^0_j = \mathbf{S}(\boldsymbol{\omega}^0_{j-1/0})\mathbf{R}^0_{j-1}\mathbf{R}^{j-1}_j + \mathbf{R}^0_{j-1}\mathbf{S}(\boldsymbol{\omega}^{j-1}_{j/j-1})\mathbf{R}^{j-1}_j \tag{2.26}$$

Since the rotation matrices are orthonormal, the last term in the previous equation is written as

$$\mathbf{R}^0_{j-1}\mathbf{S}(\boldsymbol{\omega}^{j-1}_{j/j-1})\mathbf{R}^{j-1}_j = \mathbf{R}^0_{j-1}\mathbf{S}(\boldsymbol{\omega}^{j-1}_{j/j-1})\mathbf{R}^{j-1}_0\mathbf{R}^0_{j-1}\mathbf{R}^{j-1}_j \tag{2.27}$$

and by the relation stated in Equation 2.10, the full expression is rewritten to

$$\mathbf{S}(\boldsymbol{\omega}_{j/0}^{0})\mathbf{R}_{j}^{0} = \mathbf{S}(\boldsymbol{\omega}_{j-1/0}^{0})\mathbf{R}_{j}^{0} + \mathbf{S}(\mathbf{R}_{j-1}^{0}\boldsymbol{\omega}_{j/j-1}^{j-1})\mathbf{R}_{j}^{0} \tag{2.28}$$

The angular velocity of rigid body j is then written as

$$\boldsymbol{\omega}_{j/0}^{0} = \boldsymbol{\omega}_{j-1/0}^{0} + \mathbf{R}_{j-1}^{0}\boldsymbol{\omega}_{j/j-1}^{j-1} = \boldsymbol{\omega}_{j-1/0}^{0} + \boldsymbol{\omega}_{j/j-1}^{0} \tag{2.29}$$

which implies that the angular velocity of rigid body j is the sum of the angular velocity of rigid body j-1 with respect to the inertial frame and the angular velocity of rigid body j with respect to rigid body j-1.

With the definitions of both the linear and angular velocities, two separate cases must be considered. These cases are related to the last two terms in the expression of the linear velocity given in Equation 2.23. The two terms are associated with the elongation and rotation of joint i and are relevant depending on whether it is a prismatic or revolute joint. Note that both the elongation and angles of the joints commonly are selected as the generalized coordinates for robot manipulators when considering prismatic and revolute joints, respectively.

Prismatic joint

In this case, the angular velocity of body j with respect to rigid body j-1 is zero since the joint connecting them does not rotate

$$\boldsymbol{\omega}_{j/j-1}^{0} = 0 \tag{2.30}$$

The contribution from the elongation of rigid body j by joint i gives

$$\mathbf{v}_{j/j-1}^{0} = \dot{q}_{i}\mathbf{e}_{i}^{0} \tag{2.31}$$

where $\mathbf{e}_{i}^{0}$ is the unit vector defined in the direction in which the joint displaces. Due to the simplicity of expressing the direction in a body-fixed frame, the unit vector in the inertial frame is later found as follows

$$\mathbf{e}_{i}^{0} = \mathbf{R}_{i}^{0}\mathbf{e}_{i}^{i} \tag{2.32}$$

where $\mathbf{e}_{i}^{i}$ is given by the combination of the relevant unit vectors $\mathbf{i} = [1,\ 0,\ 0]$, $\mathbf{j} = [0,\ 1,\ 0]$ and $\mathbf{k} = [0,\ 0,\ 1]$ in regard to the directions in which the joint is able to displace. The resulting linear and angular velocities of the center of gravity then become

$$\begin{aligned} \boldsymbol{\omega}_{j/0}^{0} &= \boldsymbol{\omega}_{j-1/0}^{0} \\ \mathbf{v}_{cg_j/0}^{0} &= \mathbf{v}_{j/0}^{0} + \dot{q}_{i}\mathbf{e}_{i}^{0} + \boldsymbol{\omega}_{j/0}^{0} \times \mathbf{r}_{cg_j/j}^{0} \end{aligned} \tag{2.33}$$

Revolute joint

When evaluating revolute joints, the angular velocity of rigid body j with respect to rigid body j-1 is the rotational velocity of joint i

$$\boldsymbol{\omega}_{j/j-1}^{0} = \dot{q}_{i}\mathbf{e}_{i}^{0} \tag{2.34}$$

As there is no elongation, the second term in the equation of the linear velocity becomes zero. The resulting expressions of the linear and angular velocities of the center of gravity then become

$$\begin{aligned} \boldsymbol{\omega}^0_{j/0} &= \boldsymbol{\omega}^0_{j-1/0} + \dot{q}_i \mathbf{e}^0_i \\ \mathbf{v}^0_{cg_j/0} &= \mathbf{v}^0_{j/0} + \boldsymbol{\omega}^0_{j/0} \times \mathbf{r}^0_{cg_j/j} \end{aligned} \tag{2.35}$$

A general expression of the Jacobian matrix

With the use of the definition of linear velocities given in Equation 2.23 and Equation 2.24, and the properties of prismatic and revolute joints, the contribution to the linear velocity due to the generalized coordinate $\dot{q}_i$ is described in Equation 2.36. It should be noted that for the cases where i > j, joint i has no contribution to the linear velocity of rigid body j.

$$\mathbf{v}^{(\dot{q}_i)}_{cg_j/0} = \begin{cases} \dot{q}_i \mathbf{e}^0_i \times (\mathbf{r}^0_{cg_j/0} - \mathbf{r}^0_{i/0}), & \text{if joint i is revolute and i} \leq \text{j} \\ \dot{q}_i \mathbf{e}^0_i, & \text{if joint i is prismatic and i} \leq \text{j} \\ \dot{q}_i \mathbf{0}_{3x1}, & \text{if joint i} > \text{j} \end{cases} \tag{2.36}$$

From the definition of the relation between the linear velocity and the generalized coordinates in Equation 2.21, the Jacobian matrix of the contribution by a generalized coordinate is defined as follows

$$\mathbf{J}^{(\dot{q}_i)}_{v_{cg_j}} = \begin{cases} \mathbf{e}^0_i \times (\mathbf{r}^0_{cg_j/0} - \mathbf{r}^0_{i/0}), & \text{if joint i is revolute and i} \leq \text{j} \\ \mathbf{e}^0_i, & \text{if joint i is prismatic and i} \leq \text{j} \\ \mathbf{0}_{3x1}, & \text{if i} > \text{j} \end{cases} \tag{2.37}$$

The contribution to the angular velocity due to the generalized coordinate $\dot{q}_i$ is found in a similar manner

$$\boldsymbol{\omega}^{(\dot{q}_i)}_{j/0} = \begin{cases} \dot{q}_i \mathbf{e}^0_i, & \text{if joint i is revolute and i} \leq \text{j} \\ \dot{q}_i \mathbf{0}_{3x1}, & \text{if joint i is prismatic and i} \leq \text{j} \\ \dot{q}_i \mathbf{0}_{3x1}, & \text{if i} > \text{j} \end{cases} \tag{2.38}$$

and consequently, the Jacobian matrix of the contribution by a generalized coordinate is defined as follows

$$\mathbf{J}^{(\dot{q}_i)}_{\omega_j} = \begin{cases} \mathbf{e}^0_i, & \text{if joint i is revolute and i} \leq \text{j} \\ \mathbf{0}_{3x1}, & \text{if joint i is prismatic and i} \leq \text{j} \\ \mathbf{0}_{3x1}, & \text{if i} > \text{j} \end{cases} \tag{2.39}$$

With this, the total linear and angular velocity of the center of gravity of rigid body j is found by taking the sum of all the individual contributions from n rigid bodies

$$\begin{aligned} \mathbf{v}^0_{cg_j/0} &= \mathbf{J}^{(\dot{q}_1)}_{v_{cg_j}} \dot{q}_1 + \mathbf{J}^{(\dot{q}_2)}_{v_{cg_j}} \dot{q}_2 + ... + \mathbf{J}^{(\dot{q}_j)}_{v_{cg_j}} \dot{q}_j + \mathbf{0}_{3x1} \dot{q}_{j+1} + ... + \mathbf{0}_{3x1} \dot{q}_n \\ &= \begin{bmatrix} \mathbf{J}^{(\dot{q}_1)}_{v_{cg_j}} & \mathbf{J}^{(\dot{q}_2)}_{v_{cg_j}} & ... & \mathbf{J}^{(\dot{q}_j)}_{v_{cg_j}} & \mathbf{0}_{3x(n-j)} \end{bmatrix} \dot{\mathbf{q}} \\ &= \mathbf{J}_{v_{cg_j}}(\mathbf{q}) \dot{\mathbf{q}} \end{aligned} \tag{2.40}$$

$$\begin{aligned} \boldsymbol{\omega}^0_{j/0} &= \mathbf{J}^{(\dot{q}_1)}_{\omega_j} \dot{q}_1 + \mathbf{J}^{(\dot{q}_2)}_{\omega_j} \dot{q}_2 + ... + \mathbf{J}^{(\dot{q}_j)}_{\omega_j} \dot{q}_j + \mathbf{0}_{3x1} \dot{q}_{j+1} + ... + \mathbf{0}_{3x1} \dot{q}_n \\ &= \begin{bmatrix} \mathbf{J}^{(\dot{q}_1)}_{\omega_j} & \mathbf{J}^{(\dot{q}_2)}_{\omega_j} & ... & \mathbf{J}^{(\dot{q}_j)}_{\omega_j} & \mathbf{0}_{3x(n-j)} \end{bmatrix} \dot{\mathbf{q}} \\ &= \mathbf{J}_{\omega_j}(\mathbf{q}) \dot{\mathbf{q}} \end{aligned} \tag{2.41}$$

Lastly, the linear and rotational velocities are related to the generalized coordinates in a compact form as follows

$$\boldsymbol{\nu}_{cg_j} = \begin{bmatrix} \mathbf{v}^0_{cg_j/0} \\ \boldsymbol{\omega}^0_{j/0} \end{bmatrix} = \begin{bmatrix} \mathbf{J}_{v_{cg_j}}(\mathbf{q}) \\ \mathbf{J}_{\omega_j}(\mathbf{q}) \end{bmatrix} \dot{\mathbf{q}} = \mathbf{J}(\mathbf{q})\dot{\mathbf{q}} \tag{2.42}$$

where $\mathbf{J}$ is the Jacobian matrix that defines the transformation of both the linear and rotational velocities.

Inverting the Jacobian matrix

A matrix is invertible if it is a square and non-singular matrix, meaning that in most cases the inverse of the Jacobian matrix does not exist. However, a right pseudo-inverse matrix $\mathbf{J}^\dagger$ is developed as follows for the general case of inverting the Jacobian matrix (Siciliano et al., 2009)

$$\mathbf{J}^\dagger = \mathbf{J}^T(\mathbf{J}\mathbf{J}^T)^{-1} \tag{2.43}$$

It is denoted right pseudo-inverse since it satisfies the following condition

$$\mathbf{J}\mathbf{J}^\dagger = \mathbf{I} \tag{2.44}$$

Close to a singularity, the inverse of the Jacobian matrix can result in large joint velocities. To reduce this issue, a damping term is included in the definition of the pseudo-inverse, leading to the damped least-squares inverse (Siciliano et al., 2009)

$$\mathbf{J}^\dagger = \mathbf{J}^T(\mathbf{J}\mathbf{J}^T + k^2\mathbf{I}) \tag{2.45}$$

where k is the damping coefficient. A variety of methods have been developed to determine the value of the damping coefficient and a common approach is to base it on a Jacobian-dependent variable. In Nakamura and Hanafusa (1986), the damping coefficient is defined through the definition of the manipulability measure expressed as

$$w = \sqrt{det(\mathbf{J}\mathbf{J}^T)} \tag{2.46}$$

Since the manipulability measure is equal to zero at singular points, but it increases as the manipulator moves away from singular configurations, it represents a measure of the proximity to singular points. It is therefore suggested by Nakamura and Hanafusa (1986) to express the damping coefficient as follows

$$k = \begin{cases} k_0(1 - \frac{w}{w_0})^2, & w < w_0 \\ 0, & w \geq w_0 \end{cases} \tag{2.47}$$

where k_0 is a scaling factor while w_0 is the boundary threshold defined around the singularities. Note that the approach suggested in Nakamura and Hanafusa (1986) does not yield an optimal solution as the joint velocities can be dampened in configurations were it is not required. Therefore, optimization methods can be applied as proposed in Deo and Walker (1992).

Differentiation of the Jacobian matrix

The definition of the derivative of the Jacobian matrix follows from the general definition of the Jacobian matrix for an open chain of linked rigid bodies. For the linear and angular velocity contributions induced by the generalized coordinate q_i at the arbitrary point p_j on the jth rigid body, the derivative of the Jacobian matrix becomes

$$\dot{\mathbf{J}}^{(q_i)}_{v_{p_j}/0} = \begin{cases} \dot{\mathbf{e}}^0_i \times (\mathbf{r}^0_{cg_j/0} - \mathbf{r}^0_{i/0}) + \mathbf{e}^0_i \times (\dot{\mathbf{r}}^0_{cg_j/0} - \dot{\mathbf{r}}^0_{i/0}), & \text{if joint i is revolute and i} \leq \text{j} \\ \dot{\mathbf{e}}^0_i, & \text{if joint i is prismatic and i} \leq \text{j} \\ \mathbf{0}_{3x1}, & \text{if i} > \text{j} \end{cases}$$
$$\dot{\mathbf{J}}^{(q_i)}_{\omega_j/0} = \begin{cases} \dot{\mathbf{e}}^0_i, & \text{if joint i is revolute and i} \leq \text{j} \\ \mathbf{0}_{3x1}, & \text{if joint i is prismatic and i} \leq \text{j} \\ \mathbf{0}_{3x1}, & \text{if i} > \text{j} \end{cases} \tag{2.48}$$

The unit vector $\mathbf{e}^0_i$ was previously defined in Equation 2.32 and consequently, its derivative becomes the following

$$\dot{\mathbf{e}}^0_i = \dot{\mathbf{R}}^0_i \mathbf{e}^i_i + \mathbf{R}^0_i \dot{\mathbf{e}}^i_i \tag{2.49}$$

By applying the definition of the derivative of the rotation matrix given in Equation 2.9 and the fact that the derivative of a unit vector equals zero, the expression is simplified to the following

$$\dot{\mathbf{e}}^0_i = \mathbf{S}(\boldsymbol{\omega}^0_{j/0})\mathbf{R}^0_i \mathbf{e}^i_i = \mathbf{S}(\boldsymbol{\omega}^0_{j/0})\mathbf{e}^0_i = \boldsymbol{\omega}^0_{j/0} \times \mathbf{e}^0_i \tag{2.50}$$

The derivative of the position vectors in the Jacobian matrix is given by the definition in Equation 2.2.

$$\dot{\mathbf{r}}^0_{cg_j/0} - \dot{\mathbf{r}}^0_{i/0} = \dot{\mathbf{r}}^0_{cg_j/0} + \boldsymbol{\omega}^0_{j/0} \times \mathbf{r}^0_{cg_j/0} - (\dot{\mathbf{r}}^0_{i/0} + \boldsymbol{\omega}^0_{i/0} \times \mathbf{r}^0_{i/0}) \tag{2.51}$$

It becomes obvious that taking the derivative of the Jacobian matrix results in complex expressions that are prone to mistakes as the number of generalized coordinates increases. Therefore, another approach is considered since the Jacobian matrix is a function of the generalized coordinates. By applying the chain rule, the following is true

$$\dot{\mathbf{J}}(\mathbf{q}) = \frac{\partial \mathbf{J}(\mathbf{q})}{\partial \mathbf{q}} \dot{\mathbf{q}} \tag{2.52}$$

Consequently, Equation 2.52 provides an approach less susceptible to errors in the case where the expressions in the Jacobian matrix are available for calculation of the partial derivatives.

2.1.6 State-space model

With the development of the Jacobian matrix, the tools that are required to generate the state-space model of the system have been defined. Sciavicco and Siciliano (2000) show that the rigid body dynamics can be rewritten into a more conventional form than the one given by Lagrange's equation of motion. Equation 2.53 shows the proposed state-space model

$$\mathbf{B}(\mathbf{q})\ddot{\mathbf{q}} + \mathbf{C}(\mathbf{q}, \dot{\mathbf{q}})\dot{\mathbf{q}} + \mathbf{g}(\mathbf{q}) = \boldsymbol{\tau} \tag{2.53}$$

where $\mathbf{B}(\mathbf{q})$, $\mathbf{C}(\mathbf{q}, \dot{\mathbf{q}})$, and $\mathbf{g}(\mathbf{q})$ are the mass-inertia matrix, the centripetal and Coriolis matrix and the restoring force and moment vector, respectively. $\boldsymbol{\tau}$ is directly connected to the generalized forces that were denoted Q_i, i.e. actuator forces and friction forces that act on the system.

The mass-inertia matrix is obtained directly from the expression of the kinetic energy in the system. If the connection between the generalized coordinates and the linear and angular velocities are given by the Jacobian matrix as shown in Equation 2.42, the expression of the kinetic energy given in Equation 2.12 can be rewritten to the following

$$\begin{aligned} T_j(\mathbf{q},\dot{\mathbf{q}},t) &= \frac{1}{2}\boldsymbol{\nu}_j^T\mathbf{M}_j\boldsymbol{\nu}_j, \quad \mathbf{M}_j = \begin{bmatrix} m_j\mathbf{I}_{3x3} & \mathbf{0}_{3x3} \\ \mathbf{0}_{3x3} & \mathbf{I}_j \end{bmatrix} \\ T_j(\mathbf{q},\dot{\mathbf{q}},t) &= \frac{1}{2}\dot{\mathbf{q}}^T\mathbf{J}_j^T(\mathbf{q})\mathbf{M}_j\mathbf{J}_j(\mathbf{q})\dot{\mathbf{q}} = \frac{1}{2}\dot{\mathbf{q}}^T\mathbf{B}_j(\mathbf{q})\dot{\mathbf{q}} \\ T(\mathbf{q},\dot{\mathbf{q}},t) &= \frac{1}{2}\dot{\mathbf{q}}^T\sum_{j=1}^{n}(\mathbf{B}_j(\mathbf{q}))\dot{\mathbf{q}} = \frac{1}{2}\dot{\mathbf{q}}^T\mathbf{B}(\mathbf{q})\dot{\mathbf{q}} \end{aligned} \tag{2.54}$$

The centripetal and Coriolis matrix cannot be chosen uniquely, but a suggested method is given by Sciavicco and Siciliano (2000) as

$$c_{ij} = \frac{1}{2}\sum_{k=1}^{n}\left(\frac{\partial b_{ij}}{\partial q_k} + \frac{\partial b_{ik}}{\partial q_j} - \frac{\partial b_{jk}}{\partial q_i}\right),\ i = 1,2,...,n,\ j = 1,2,...,n \tag{2.55}$$

where c_{ij} is the ijth element in the **C**-matrix and b_{ij} is the ijth element in the **B**-matrix. In Rokseth (2014), it is shown that the **C**-matrix can be found by differentiating the kinetic energy with respect to the generalized coordinates

$$\mathbf{C}(\mathbf{q},\dot{\mathbf{q}})\dot{\mathbf{q}} = \frac{1}{2}\dot{\mathbf{q}}^T\frac{\partial\mathbf{B}(\mathbf{q})}{\partial\mathbf{q}}\dot{\mathbf{q}} \tag{2.56}$$

where

$$\mathbf{q}^T\frac{\partial\mathbf{B}(\mathbf{q})}{\partial\mathbf{q}}\mathbf{q} = \begin{bmatrix} \mathbf{q}^T\frac{\partial\mathbf{B}(\mathbf{q})}{\partial q_i} \\ \vdots \\ \mathbf{q}^T\frac{\partial\mathbf{B}(\mathbf{q})}{\partial q_n} \end{bmatrix}\mathbf{q} \tag{2.57}$$

The $\mathbf{g}(\mathbf{q})$-vector is determined by differentiating the potential energy term in Lagrange's equation with respect to the generalized coordinates

$$\mathbf{g}(\mathbf{q}) = \frac{\partial V}{\partial\mathbf{q}} \tag{2.58}$$

2.2 Bond graph modeling

Bond graph modeling is an energy based-method that is applied in the development of mathematical models of physical systems. It is based on the intuitive approach where a dynamic system can be divided into a set of subsystems, components and basic elements that interact through the exchange of energy (Borutzky, 2010). Since bond graph modeling is based on the conservation of energy, the exchange of energy is described by basic elements that represent storage, supply, dissipation or transformation of energy in the system. These basic elements interact through power bonds that are connected between the power ports of elements. The power ports represent a point of energetic interaction between different parts of a system and the power bonds that connects them to each other are considered to transmit power, i.e. energy flow, instantaneously and without

loss (Pedersen and Engja, 2014). The power that is transmitted over a power bond is represented by the product of the two power variables effort and flow denoted e and f, respectively.

$$P(t) = e(t)f(t) \tag{2.59}$$

The concept of energy exchange between subsystems and the transformations from one form to another is what makes bond graph modeling suitable for multidisciplinary systems (Borutzky, 2010). For a mechanical system, the effort and flow are force and velocity, respectively, while they are voltage and current in an electrical system. The transformation from one discipline to another is done through transformations that will be explained later on.

Similar to other modeling approaches, bond graph modeling requires the correct sign convention for positive and negative directions. In this case, the sign convention is related to the definition of the positive direction of the power transmission between elements. In Figure 2.3, the energy flow between two subsystems is assigned positive in the direction of the half-arrow. It should be noted that the half-arrow convention is used to distinguish energy flow from signal inputs, which are given by whole arrows. The vertical line denoted causality stroke that is placed on the half-arrow defines which system that has an effort input and which system that has a flow input. The effort input is defined to always be on the side of the power bond to which the causality is assigned, which in this case would indicate an effort input to subsystem 1 and a flow input to subsystem 2.

Figure 2.3: Power bond describing the energy flow between two systems

Two additional physical quantities are central in the description of the energy flow in a system and they are related to the effort and flow variables defined earlier. They are called generalized momentum, p, and generalized displacement, q, and are found through the integration of the effort and flow, respectively, with respect to time (Borutzky, 2010)

$$p(t) = \int_0^t e(\tau)d\tau + p(t_0) \tag{2.60}$$

$$q(t) = \int_0^t f(\tau)d\tau + q(t_0) \tag{2.61}$$

Here $p(t_0)$ and $q(t_0)$ are the initial conditions. As mentioned earlier, these variables can be related to multiple disciplines and Table 2.1 shows what they represent when modeling systems in different physical domains[1].

[1]Only the systems that could be relevant in the master's thesis are presented

Table 2.1: Identification of variables (Pedersen and Engja, 2014)

Energy domain	**Effort (e)**	**Flow (f)**	**Momentum (p)**	**Displacement (q)**
Electrical	Voltage [V]	Current [i]	Flux linkage [Vs]	Charge [As] or [C]
Mechanical translation	Force [N]	Velocity [m/s]	Linear momentum [kgm/s]	Distance [m]
Mechanical rotation	Torque [Nm]	Angular velocity [rad/s]	Angular momentum [Nms]	Angle [rad]
Hydraulic	Pressure [Pa]	Volume flow rate [m^3/s]	Pressure momentum [N/m^2s]	Volume [m^3]

It was mentioned that a set of basic ideal elements are used to represent energy storage, dissipation, supply and transformation in the system. These elements and their constitutive relations will be discussed in the upcoming sections.

2.2.1 Storage elements

Storage elements are divided into two types: inertia elements, I, and compliance elements, C. In mechanical systems the I-element represents kinetic energy while the C-element represents potential energy. As stated in Borutzky (2010), the C-element is characterized by a constitutive relation between the effort and displacement given by the one-to-one function Φ_C

$$q(t) = \Phi_C(e(t)) \tag{2.62}$$

where Φ_C must have a unique single-valued inverse Φ_C^{-1}. The same is true for the I-element, which is characterized by a constitutive relation between the flow and momentum given by the one-to-one function Φ_I

$$p(t) = \Phi_I(f(t)) \tag{2.63}$$

where Φ_I must have a unique single-valued inverse Φ_I^{-1}. The requirement related to a unique single-valued inverse of the one-to-one functions is given such that Equation 2.62 and Equation 2.63 can be solved for the effort and flow, respectively

$$e(t) = \Phi_C^{-1}(q(t)) = \Phi_C^{-1}(\int_0^t f(\tau)d\tau) \tag{2.64}$$

$$f(t) = \Phi_I^{-1}(p(t)) = \Phi_I^{-1}(\int_0^t e(\tau)d\tau) \tag{2.65}$$

Here the importance of proper causality assignment comes to light. If the effort is assigned as input to a C-element, the flow must be calculated from the differentiation of the effort. Since differentiation is problematic in situations where there are step signals, a differential causality is not preferred. An identical issue arises with a flow input to an I-element since the effort must be calculated from the differentiation of the flow. The constitutive relations of the C-element and the I-element with derivative causalities are given in Equation 2.66 and Equation 2.67, respectively.

$$f(t) = \frac{d}{dt}[\Phi_C(e(t))] \tag{2.66}$$

$$e(t) = \frac{d}{dt}[\Phi_I(f(t))] \tag{2.67}$$

To avoid these problems, integral causality is preferred, implying flow input to a C-element and effort input to an I-element. With this causality assignment, the expressions in Equation 2.64 and Equation 2.65, which contain integration rather than differentiation, can be applied. A C-element and an I-element with integral causalities are shown in Figure 2.4

(a) Capacitor element

(b) Inertia element

Figure 2.4: Storage elements

2.2.2 Resistor elements

The element that represents the dissipation of energy is the resistor element R. The causality assignment of the R-element is indifferent as no differentiation appears regardless of the choice of flow or effort input. As stated in Borutzky (2010), the R-element is characterized by a constitutive relation between the effort and flow given by the one-to-one function Φ_R

$$e(t) = \Phi_R(f(t)) \iff f(t) = \Phi_R^{-1}(e(t)) \tag{2.68}$$

where Φ_R must have a unique single-valued inverse Φ_R^{-1}. R-elements with effort and flow input are illustrated in Figure 2.5

(a) Resistor element with effort input

(b) Resistor element with flow input

Figure 2.5: Resistor elements

2.2.3 Source elements

Source elements are used to represent the supply of energy to a system either in the form of a flow from a flow source, *Sf*, or an effort from an effort source, *Se*. These elements describe the boundary conditions and can provide a power variable that is either constant or time-varying. As the source elements are assumed ideal, the flow source imposes a flow input regardless of the effort and the effort source imposes an effort input regardless of the flow (Pedersen and Engja, 2014).

(a) Effort source

(b) Flow source

Figure 2.6: Source elements

2.2.4 Transformer elements

The last set of basic elements are the ones that most often, but not exclusively, are used to transform the energy from one domain to another. They differ from the previously presented basic elements by being 2-port elements that transmit the power from the power bond at one side to the power bond on the other side, as shown in Figure 2.7.

(a) Transformer element (b) Gyrator element

Figure 2.7: Transformer elements

As stated in Pedersen and Engja (2014), they are assumed to transmit the power instantaneously without storing or dissipation of energy, meaning that the power remains unchanged through the transformation. Therefore, there are two cases of constitutive relations between the flows and efforts at either side of the transformation element as shown below

$$\begin{aligned} e_1 &= me_2 \\ mf_1 &= f_2 \end{aligned} \tag{2.69}$$

$$\begin{aligned} e_1 &= rf_2 \\ rf_1 &= e_2 \end{aligned} \tag{2.70}$$

Here m and r represent the transformation modulus for the transformer element, TF, the gyrator element, GY, respectively. It should be noted that the modulus r always has physical dimensions while the modulus m can be dimensionless. The TF-element is often used to represent the reduction in gearboxes or belt transmissions but is additionally applied to relate the two mechanical energy domains. The GY-element is most commonly utilized to describe the transformation of energy from one domain to another, which is observed in electric motors and centrifugal pumps.

2.2.5 Modulated elements

The resistor, source and transformation elements can have constitutive relations that are dependent on variables that are not directly accessible. In that case, the elements are modulated by having input signals sent to the respective elements. A modulated element is denoted by placing an M in front of the abbreviation of the element name. This is illustrated in Figure 2.8

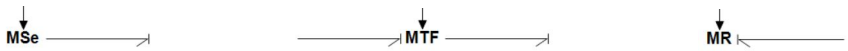

(a) Modulated effort source (b) Modulated TF-element (c) Modulated resistor element

Figure 2.8: Modulated elements

2.2.6 Power conserving junctions

Power conserving junctions are employed in addition to the previously described elements to connect the different elements together in the correct manner with respect to the system that is modeled. They are designed to distribute the energy instantaneously through the connected power bonds without storing or dissipating energy. This implies that they are based on the concept of conservation of energy and that the power entering should be equal to the power leaving the power conserving junction. This condition can be implemented by requiring either equal flows or equal efforts in the power bonds that are connected to the power conserving junction. The junction where the efforts are set equal is called a 0-junction. Consequently, only a single causality stroke can be placed such that it defines an effort input to the 0-junction. The constitutive relation is given by

$$\begin{aligned} e_1 = e_2 = ... = e_n \\ f_1 + f_2 + ... + f_n = 0 \end{aligned} \tag{2.71}$$

The junction where the flows are set identical is denoted a 1-junction. Consequently, only one of the causality strokes can be set such that it defines a flow input to the 1-junction. The constitutive relation is given by

$$\begin{aligned} f_1 &= f_2 = ... = f_n \\ e_1 &+ e_2 + ... + e_n = 0 \end{aligned} \tag{2.72}$$

Figure 2.9 shows the two types of junctions for n connected power bonds

(a) 0-junction (b) 1-junction

Figure 2.9: Power conserving elements

2.2.7 IC-field

IC-fields are suitable when implementing a model into the bond graph language when utilizing the Lagrangian equations of motion. This is because an IC-field accumulates the total energy contribution from both the kinetic and potential energy terms, which the Lagrangian equations of motion are based on. Additionally, it facilitates the removal of the problem related to differential causalities since IC-fields are defined with integral causalities. This is shown in Figure 2.10 where the power bond going to the I-element sets the effort input and the power bond directed from the C-element defines the flow input to the IC-field. Note that an IC-field can be interfaced with multiple 1-junctions.

Figure 2.10: Illustration of an IC-field

In Rokseth (2014), it is shown that the state-space model derived in Section 2.1.6 can be written with both the momentum and the generalized coordinates as the system states. This is derived through the term $\frac{\partial T}{\partial \dot{q}_i}$, which is equal to the momentum p_i.

$$\mathbf{p} = \frac{\partial T}{\partial \dot{\mathbf{q}}} = \mathbf{B}(\mathbf{q})\dot{\mathbf{q}} \iff \dot{\mathbf{q}} = \mathbf{B}^{-1}(\mathbf{q})\mathbf{p} \tag{2.73}$$

$$\dot{\mathbf{p}} = \frac{d}{dt}\frac{\partial T}{\partial \dot{\mathbf{q}}} = \mathbf{B}(\mathbf{q})\ddot{\mathbf{q}} + \dot{\mathbf{B}}(\mathbf{q})\dot{\mathbf{q}} = \mathbf{B}(\mathbf{q})\ddot{\mathbf{q}} + \dot{\mathbf{q}}^T\frac{\partial \mathbf{B}(\mathbf{q})}{\partial \mathbf{q}}\dot{\mathbf{q}} \tag{2.74}$$

By solving the state-space model given in Equation 2.53 for $\mathbf{B}(\mathbf{q})\ddot{\mathbf{q}}$ and utilizing the definition of the centripetal and Coriolis matrix given in Equation 2.56, the expression of the derivative of the momentum can be rewritten to

$$\begin{aligned}\dot{\mathbf{q}} &= \mathbf{B}^{-1}(\mathbf{q})\mathbf{p} \\ \dot{\mathbf{p}} &= \mathbf{f}(\mathbf{q}, \dot{\mathbf{q}}) + \boldsymbol{\tau}\end{aligned} \tag{2.75}$$

where

$$\mathbf{f}(\mathbf{q}, \dot{\mathbf{q}}) = \frac{1}{2}\dot{\mathbf{q}}^T \frac{\partial \mathbf{B}(\mathbf{q})}{\partial \mathbf{q}}\dot{\mathbf{q}} - \mathbf{g}(\mathbf{q}) \tag{2.76}$$

As derived in Rokseth (2014) the resulting Equation 2.75 is equal to the constitutive relation that is employed in an IC-field.

2.3 Marine vessel dynamics

In Rokseth et al. (2017), a generic method for deriving vessel dynamics with the use of Lagrangian mechanics was developed and the process is presented here. To begin with, it is common to relate the position and orientation of the vessel to an inertial reference frame, which in terms of Lagrangian mechanics is a necessity in regard to establishing the equations of motion. In addition, a body-fixed reference frame is attached to the rigid body that represents the vessel. The vessel position is given by the position vector $\mathbf{r}^0_{b/0}$ while the orientation is given by the Euler angles $\boldsymbol{\Theta} = [\phi,\ \theta,\ \psi]^T$. Hence, the generalized coordinates of the vessel are chosen as

$$\mathbf{q} = \begin{bmatrix} \mathbf{r}^0_{b/0} \\ \boldsymbol{\Theta} \end{bmatrix} \tag{2.77}$$

since they uniquely describe the position and orientation of the vessel.

2.3.1 Vessel kinetic energy

As shown in Equation 2.12, the kinetic energy of the vessel can be expressed as follows

$$T_b(\mathbf{q}, \dot{\mathbf{q}}, t) = \frac{1}{2} m_b \mathbf{v}^T(\mathbf{q}, \dot{\mathbf{q}})^b_{cg_b/0} \mathbf{v}(\mathbf{q}, \dot{\mathbf{q}})^b_{cg_b/0} + \frac{1}{2}\boldsymbol{\omega}^T(\mathbf{q}, \dot{\mathbf{q}})^b_{b/0} \mathbf{I}^b_b \boldsymbol{\omega}(\mathbf{q}, \dot{\mathbf{q}})^b_{b/0}$$

Since the kinetic energy must be expressed by generalized coordinates given in an inertial reference frame, a relation between the generalized coordinates and the linear and angular velocities given in the body-fixed frame must be derived. From the general expression of the linear velocity of a rigid body, given in Equation 2.2, the following is defined

$$\begin{aligned}\mathbf{v}^b_{cg_b/0} &= \mathbf{v}^b_{b/0} + \boldsymbol{\omega}^b_{b/0} \times \mathbf{r}^b_{cg_b/b} \\ &= \mathbf{R}^b_0(\boldsymbol{\Theta})\dot{\mathbf{r}}^0_{b/0} + \mathbf{T}^{-1}_{\Theta}(\boldsymbol{\Theta})\dot{\boldsymbol{\Theta}} \times \mathbf{r}^b_{cg_b/b}\end{aligned} \tag{2.78}$$

Here, the relation between position vectors expressed in the body-fixed and inertial reference frames is given by the rotation matrix $\mathbf{R}(\boldsymbol{\Theta})$. Furthermore, the body-fixed angular velocities are related to the Euler angles through the transformation matrix $\mathbf{T}_\Theta(\boldsymbol{\Theta})$. The transformation matrix is required as the angular velocities given in the body-fixed frame cannot be integrated directly to obtain

the angular coordinates. This is because the integration has no immediate physical interpretation (Fossen, 2011). Hence, it is necessary to develop a link between the angular rates and the Euler rates since the Euler angles represent actual generalized coordinates. With the use of the zyx-convention, the body-fixed angular velocities can be related to the Euler rates as follows

$$\boldsymbol{\omega}^b_{rb/0} = \begin{bmatrix} \dot{\phi} \\ 0 \\ 0 \end{bmatrix} + \mathbf{R}^T_x(\phi) \begin{bmatrix} 0 \\ \dot{\theta} \\ 0 \end{bmatrix} + \mathbf{R}^T_x(\phi)\mathbf{R}^T_y(\theta) \begin{bmatrix} 0 \\ 0 \\ \dot{\psi} \end{bmatrix} \tag{2.79}$$

By combining the terms, the angular rates and Euler rates are related through a transformation matrix as follows

$$\boldsymbol{\omega}^b_{rb/0} = \underbrace{\begin{bmatrix} 1 & 0 & -s\theta \\ 0 & c\phi & c\theta s\phi \\ 0 & -s\phi & c\theta c\phi \end{bmatrix}}_{\mathbf{T}^{-1}_{\Theta}(\Theta)} \begin{bmatrix} \dot{\phi} \\ \dot{\theta} \\ \dot{\psi} \end{bmatrix} \Rightarrow \mathbf{T}_{\Theta}(\Theta) = \begin{bmatrix} 1 & t\theta s\phi & t\theta c\phi \\ 0 & c\phi & -s\phi \\ 0 & s\phi/c\theta & c\phi/c\theta \end{bmatrix} \tag{2.80}$$

Consequently, the angular rates of the rigid body have a physical interpretation and can be related to the inertial frame by applying the transformation matrix $\mathbf{T}_{\Theta}(\Theta)$. The Euler angles that are required in the calculation of the rotation matrix at every time step can be found by integration

$$\Theta = \begin{bmatrix} \phi \\ \theta \\ \psi \end{bmatrix} = \int_0^t (\mathbf{T}_{\Theta}(\Theta)\boldsymbol{\omega}^0_{rb/0})dt \tag{2.81}$$

With this, the body-fixed linear and rotational velocities can be related to the generalized coordinates as follows

$$\boldsymbol{\omega} = \begin{bmatrix} \mathbf{v}^b_{b/0} \\ \boldsymbol{\omega}^b_{b/0} \end{bmatrix} = \begin{bmatrix} \mathbf{R}^b_0(\boldsymbol{\Theta}) & \mathbf{0}_{3x3} \\ \mathbf{0}_{3x3} & \mathbf{T}^{-1}_{\Theta}(\boldsymbol{\Theta}) \end{bmatrix} \begin{bmatrix} \dot{\mathbf{r}}^0_{cg_b/0} \\ \dot{\boldsymbol{\Theta}} \end{bmatrix} = \boldsymbol{\alpha}^T \dot{\mathbf{q}} \tag{2.82}$$

By the development of the quasi-coordinates $\boldsymbol{\omega}$, the resulting equations of motion are dependent on the body-fixed velocities rather than the velocities given in the inertial frame. This is a useful attribute when developing a bond graph model of the vessel dynamics, as explained in Rokseth et al. (2017).

A set of Jacobian matrices that define the relationship between the linear and rotational velocities in the body-fixed frame and the quasi-coordinates can be derived. First, the expression of the linear velocity in Equation 2.78 yields

$$\begin{aligned} \mathbf{v}^b_{cg_b/0} &= \begin{bmatrix} \mathbf{I}_{3x3}, & \mathbf{i}_b \times \mathbf{r}^b_{cg_b/b}, & \mathbf{j}_b \times \mathbf{r}^b_{cg_b/b}, & \mathbf{k}_b \times \mathbf{r}^b_{cg_b/b} \end{bmatrix} \boldsymbol{\omega} \\ &= \mathbf{J}_{v_{cg_b}} \boldsymbol{\omega} \end{aligned} \tag{2.83}$$

where $\mathbf{i}_b$, $\mathbf{j}_b$, and $\mathbf{k}_b$ represent the unit vectors in the x-, y- and z-directions in the body-fixed frame, respectively. For the rotational velocity, the relation is simply expressed as

$$\begin{aligned} \boldsymbol{\omega}^b_{b/0} &= \begin{bmatrix} \mathbf{0}_{3x3}, & \mathbf{I}_{3x3} \end{bmatrix} \boldsymbol{\omega} \\ &= \mathbf{J}_{\omega_b} \boldsymbol{\omega} \end{aligned} \tag{2.84}$$

By collecting the linear and angular velocities as shown below

$$\boldsymbol{\nu}_b = \begin{bmatrix} \mathbf{v}^b_{cg_b/0} \\ \boldsymbol{\omega}^b_{b/0} \end{bmatrix} = \begin{bmatrix} \mathbf{J}_{v_b} \\ \mathbf{J}_{\omega_b} \end{bmatrix} \boldsymbol{\omega} = \mathbf{J}_b \boldsymbol{\omega} \tag{2.85}$$

the kinetic energy in terms of the quasi-coordinates becomes

$$\begin{aligned} T_b(\mathbf{q}, \boldsymbol{\omega}) &= \frac{1}{2} \boldsymbol{\omega}^T \mathbf{J}_b^T \mathbf{M}_b \boldsymbol{\omega} \mathbf{J}_b, \qquad \mathbf{M}_b = \begin{bmatrix} m_b \mathbf{I}_{3x3} & \mathbf{0}_{3x3} \\ \mathbf{0}_{3x3} & \mathbf{I}_b^b \end{bmatrix} \\ &= \frac{1}{2} \boldsymbol{\omega}^T \mathbf{B}_b \boldsymbol{\omega}, \qquad\qquad\quad \mathbf{B}_b = \mathbf{J}_b^T \mathbf{M}_b \mathbf{J}_b \end{aligned} \tag{2.86}$$

2.3.2 Quasi-equations of motion

With the use of quasi-coordinates, Lagrange's equation of motion must be differentiated by applying the chain rule since the quasi-coordinates are functions of the generalized coordinates and their rates, as explained in Rokseth et al. (2017). Consequently, the quasi-equations of motion are derived as

$$\frac{d}{dt}\left(\frac{\partial T}{\partial \boldsymbol{\omega}}\right) + \boldsymbol{\beta}^T \boldsymbol{\gamma} \frac{\partial T}{\partial \boldsymbol{\omega}} - \boldsymbol{\beta}^T \frac{\partial T}{\partial \mathbf{q}} = \boldsymbol{\beta}^T \boldsymbol{\tau} \tag{2.87}$$

where

$$\boldsymbol{\beta} = (\boldsymbol{\alpha}^T)^{-1} = \begin{bmatrix} \mathbf{R}(\boldsymbol{\Theta})^0_b & \mathbf{0}_{3x3} \\ \mathbf{0}_{3x3} & \mathbf{T}_\Theta(\boldsymbol{\Theta}) \end{bmatrix} \tag{2.88}$$

and

$$\boldsymbol{\gamma} = \begin{bmatrix} \xi_{11} & \cdots & \xi_{1k} \\ \vdots & \ddots & \vdots \\ \xi_{k1} & \cdots & \xi_{kk} \end{bmatrix} - \begin{bmatrix} \boldsymbol{\omega}^T \boldsymbol{\beta}^T \frac{\partial \boldsymbol{\alpha}}{\partial q_1} \\ \vdots \\ \boldsymbol{\omega}^T \boldsymbol{\beta}^T \frac{\partial \boldsymbol{\alpha}}{\partial q_k} \end{bmatrix}, \qquad \xi_{ij} = \boldsymbol{\omega}^T \boldsymbol{\beta}^T \frac{\partial \alpha_{ij}}{\partial \boldsymbol{q}} \tag{2.89}$$

In the $k \times k$ matrix $\boldsymbol{\gamma}$, the term $\frac{\partial \boldsymbol{\alpha}}{\partial q_i}$ is found by differentiating every element α_{ij} with respect to the generalized coordinate q_i, resulting in a square matrix. On the other hand, the term $\frac{\partial \alpha_{ij}}{\partial \mathbf{q}}$ is a column vector given by the differentiation of element α_{ij} with respect to each of the generalized coordinates. Note that k refers to the number of generalized coordinates and that the contribution from the potential energy is not included in the equations of motion as only the kinematics are of interest at this point.

By the definition of momentum, the term $\frac{\partial T}{\partial \boldsymbol{\omega}}$ is equal to the momentum of the system. Hence, the procedure of developing the constitutive relations with respect to the momentum and generalized coordinates, which was derived in Section 2.2.7, can be utilized in the case of quasi-coordinates as well. Consequently, by comparing the expression of the momentum to Equation 2.86, the following is shown

$$\mathbf{p} = \frac{\partial T}{\partial \boldsymbol{\omega}} = \mathbf{B}_b \boldsymbol{\omega} \iff \boldsymbol{\omega} = \mathbf{B}_b^{-1} \boldsymbol{p} \tag{2.90}$$

Furthermore, by knowing that

$$\dot{\mathbf{p}} = \frac{d\mathbf{p}}{dt} = \frac{d}{dt}\left(\frac{\partial T}{\partial \boldsymbol{\omega}}\right) \tag{2.91}$$

the following is given by Equation 2.87

$$\begin{aligned}\dot{\mathbf{p}} &= -\boldsymbol{\beta}^T\boldsymbol{\gamma}\frac{\partial T}{\partial \boldsymbol{\omega}} + \boldsymbol{\beta}^T\frac{\partial T}{\partial \mathbf{q}} + \boldsymbol{\beta}^T\boldsymbol{\tau} \\ &= -\boldsymbol{\beta}^T\boldsymbol{\gamma}\mathbf{B}_b\boldsymbol{\omega} + \frac{1}{2}\boldsymbol{\beta}^T\boldsymbol{\omega}^T\frac{\partial \mathbf{B}_b}{\partial \boldsymbol{q}}\boldsymbol{\omega} + \boldsymbol{\beta}^T\boldsymbol{\tau} \\ &= f(\mathbf{q},\boldsymbol{\omega}) + \boldsymbol{\beta}^T\boldsymbol{\tau}\end{aligned} \tag{2.92}$$

The fact that the quasi-coordinates are not dependent on the generalized coordinates, but rather their derivatives, and that the mass-inertia matrix is a function of the generalized coordinates is applied to derive the following relation

$$\frac{\partial T}{\partial \mathbf{q}} = \frac{1}{2}\boldsymbol{\omega}^T\frac{\partial \mathbf{B}_b(\mathbf{q})}{\partial \mathbf{q}}\boldsymbol{\omega} \tag{2.93}$$

where

$$\boldsymbol{\omega}^T\frac{\partial \mathbf{B}_b(\mathbf{q})}{\partial \mathbf{q}}\boldsymbol{\omega} = \begin{bmatrix}\boldsymbol{\omega}^T\frac{\partial \mathbf{B}_b(\mathbf{q})}{\partial q_i} \\ \vdots \\ \boldsymbol{\omega}^T\frac{\partial \mathbf{B}_b(\mathbf{q})}{\partial q_n}\end{bmatrix}\boldsymbol{\omega} \tag{2.94}$$

The state-space model that describes the kinematics of the vessel is obtained as

$$\begin{aligned}\boldsymbol{\omega} &= \mathbf{B}_b^{-1}(\mathbf{q})\mathbf{p} \\ \dot{\mathbf{p}} &= f(\mathbf{q},\boldsymbol{\omega}) + \boldsymbol{\beta}^T\boldsymbol{\tau}\end{aligned} \tag{2.95}$$

2.3.3 Wave-induced loads

Faltinsen (1990) proposes that it is possible to express the response of a vessel in irregular waves through a superposition of the response due to various regular sinusoidal wave components. Commonly, the problem regarding the derivation of the response is divided into the diffraction and radiation problems where steady-state conditions are considered. In the diffraction problem, the vessel is held stationary, i.e. restrained from oscillatory movement, and is subjected to incident regular waves. The loads generated in this case are denoted wave excitation forces. When considering the radiation problem there are no incident regular waves, but the vessel is rather forced into harmonic motion with the wave excitation frequency. The generated radiation loads are related to added mass, damping and restoring terms.

Restoring loads

The restoring loads that act on a vessel are the forces and moments generated by the gravitational and buoyancy forces. The linear restoring force is related to the difference between the gravitational and buoyancy force. Here, the buoyancy force is related to the volume displaced by the vessel and is given as follows in an inertial reference frame

$$\mathbf{f}_b^0 = \nabla \rho_w \mathbf{g} \tag{2.96}$$

Here ∇ is the displaced volume and ρ_w is the water density. The gravitational force is directly related to the gravitational constant and the mass of the vehicle and given accordingly in an inertial reference frame

$$\mathbf{f}_g^0 = m_b \mathbf{g} \tag{2.97}$$

By knowing that the gravitational force acts through the center of gravity while the buoyancy force acts through the center of buoyancy, the restoring moments expressed in the body-fixed frame becomes (Fossen, 2011)

$$\boldsymbol{\tau}_R^b = \mathbf{r}_{cg_b/b}^b \times \mathbf{R}_0^b(\boldsymbol{\Theta})\mathbf{f}_g^0 + \mathbf{r}_{cb_b/b}^b \times \mathbf{R}_0^b(\boldsymbol{\Theta})\mathbf{f}_b^0 \tag{2.98}$$

Here $\mathbf{r}_{cg_b/b}^b$ and $\mathbf{r}_{cb_b/b}^b$ are the position vectors to the center of gravity and center of buoyancy, respectively, given in the body-fixed frame. Consequently, the restoring vector $\mathbf{g}_b(\boldsymbol{\omega})$ is given as the following in an inertial reference frame

$$\mathbf{g}_b(\boldsymbol{\omega}) = \begin{bmatrix} \mathbf{R}_0^b(\boldsymbol{\Theta})(\mathbf{f}_b^0 + \mathbf{f}_g^0) \\ \mathbf{r}_{cg_b/b}^b \times \mathbf{R}_0^b(\boldsymbol{\Theta})\mathbf{f}_g^0 + \mathbf{r}_{cb_b/b}^b \times \mathbf{R}_0^b(\boldsymbol{\Theta})\mathbf{f}_b^0 \end{bmatrix} = \begin{bmatrix} \mathbf{f}_R^b \\ \boldsymbol{\tau}_R^b \end{bmatrix} \tag{2.99}$$

Added mass and damping

The loads due to added mass and damping are dependent on the motion mode, hence the magnitudes of the added mass and damping are not necessarily equal in the different degrees of freedom. Furthermore, both added mass and damping may be highly frequency dependent (Faltinsen, 1990) and must be taken into account in seakeeping theory. In Fossen (2011), Cummin's equations, which represent the movement of a vessel in the time-domain, are transformed into the frequency domain and give the following expressions for the added mass and damping coefficients at an arbitrary wave frequency ω

$$\begin{aligned} \mathbf{A}(\omega) &= \bar{\mathbf{A}} - \frac{1}{\omega}\int_0^\infty \bar{\mathbf{K}}(\tau) sin(\omega\tau) d\tau \\ \mathbf{B}(\omega) &= \int_0^\infty \bar{\mathbf{K}}(\tau) cos(\omega\tau) d\tau \end{aligned} \tag{2.100}$$

Here $\bar{\mathbf{A}} = \mathbf{A}(\infty)$ is the added mass coefficient at the infinity frequency and $\bar{\mathbf{K}}$ is the retardation matrix related to fluid memory. By applying the inverse Fourier transform the following is true (Fossen, 2011)

$$\bar{\mathbf{K}}(t) = \frac{2}{\pi}\int_0^\infty \mathbf{B}(\omega) cos(\omega\tau) d\omega \tag{2.101}$$

Consequently, by calculating the damping for all frequencies, the added mass can be expressed through the retardation function. The added mass and damping coefficients can be found with potential theory programs such as WAMIT (Fossen, 2011).

Considering maneuvering theory, the frequency dependent added mass and potential damping terms can be approximated by constant values (Fossen, 2011). To approximate the added mass-inertia and potential damping matrices, a zero-frequency model is applied for surge, sway, and yaw. When it comes to the heave, roll and pitch modes, the natural frequencies are the dominating frequencies (Fossen, 2011). Hence, when considering decoupled motion, implying that off-diagonal terms are negligible compared to the diagonal elements, the added mass-inertia and potential damping matrices become (Fossen, 2011)

$$\mathbf{B}_A \approx \begin{bmatrix} A_{11}(0) & 0 & 0 & 0 & 0 & 0 \\ 0 & A_{22}(0) & 0 & 0 & 0 & 0 \\ 0 & 0 & A_{33}(\omega_{heave}) & 0 & 0 & 0 \\ 0 & 0 & 0 & A_{44}(\omega_{roll}) & 0 & 0 \\ 0 & 0 & 0 & 0 & A_{55}(\omega_{pitch}) & 0 \\ 0 & 0 & 0 & 0 & 0 & A_{66}(0) \end{bmatrix} \tag{2.102}$$

$$\mathbf{D}_p \approx \begin{bmatrix} B_{11}(0) & 0 & 0 & 0 & 0 & 0 \\ 0 & B_{22}(0) & 0 & 0 & 0 & 0 \\ 0 & 0 & B_{33}(\omega_{heave}) & 0 & 0 & 0 \\ 0 & 0 & 0 & B_{44}(\omega_{roll}) & 0 & 0 \\ 0 & 0 & 0 & 0 & B_{55}(\omega_{pitch}) & 0 \\ 0 & 0 & 0 & 0 & 0 & B_{66}(0) \end{bmatrix} \tag{2.103}$$

where $B_{11}(0) = B_{22}(0) = B_{66}(0) = 0$. As a side note, the added centripetal and Coriolis can be defined as follows through added mass-inertia matrix (Fossen, 2011)

$$\mathbf{C}_A = \begin{bmatrix} \mathbf{0}_{3x3} & -\mathbf{S}(\mathbf{A}_{11}\mathbf{v}^b_{b/0} + \mathbf{A}_{12}\boldsymbol{\omega}^b_{b/0}) \\ -\mathbf{S}(\mathbf{A}_{11}\mathbf{v}^b_{b/0} + \mathbf{A}_{12}\boldsymbol{\omega}^b_{b/0}) & -\mathbf{S}(\mathbf{A}_{21}\mathbf{v}^b_{b/0} + \mathbf{A}_{22}\boldsymbol{\omega}^b_{b/0}) \end{bmatrix} \tag{2.104}$$

where

$$\mathbf{B}_A = \begin{bmatrix} \mathbf{A}_{11} & \mathbf{A}_{12} \\ \mathbf{A}_{21} & \mathbf{A}_{22} \end{bmatrix} \tag{2.105}$$

In addition to the potential damping, other linear and nonlinear damping phenomena such as skin friction, vortex shedding, and wave drift affect the vessel. The wave drift damping is related to second-order wave theory and its contribution is proportional to the significant wave height H_s. When it comes to the skin friction, it is both a linear and nonlinear frequency dependent damping caused by laminar and turbulent boundary layers, respectively. The damping force due to vortex shedding is a nonlinear viscous phenomenon that can be modeled as follows (Fossen, 2011)

$$\mathbf{D}_{NL_v} = \frac{1}{2}\rho_w C_D (\mathbf{v}^b_{b/r})^T \mathbf{A} |\mathbf{v}^b_{b/r}| \tag{2.106}$$

where $A = diag(A_1, A_2, A_3)$ contains the projected cross-sectional areas under water in the surge, sway, and heave directions. Note that $\mathbf{v}^b_{b/r}$ is the vessel velocity relative to an incoming current with velocity $\mathbf{v}^0_c$, given by the following relation in the body-fixed reference frame

$$\mathbf{v}^b_{b/r} = \mathbf{v}^b_{b/0} - \mathbf{R}^b_0(\boldsymbol{\Theta})\mathbf{v}^0_c \tag{2.107}$$

Furthermore, Fossen (2011) presents a method for approximating the linear viscous damping contribution by evaluating the ratio between the total mass of the vessel and typical time constants in surge, sway, and yaw. To adjust the damping in heave, roll, and pitch, a tunable damping ratio is introduced similarly to the damping term described for a wire element in Section 2.4.1. Hence, the following damping coefficients can be used when approximating the linear damping contribution due to viscous effects

$$\begin{aligned}
B_{11_v} &= \frac{m_b + A_{11}(0)}{T_{surge}} \\
B_{22_v} &= \frac{m_b + A_{22}(0)}{T_{sway}} \\
B_{33_v} &= 2\zeta_{heave}\omega_{heave}(m_b + A_{33}(\omega_{heave})) \\
B_{44_v} &= 2\zeta_{roll}\omega_{roll}(I_y + A_{44}(\omega_{roll})) \\
B_{55_v} &= 2\zeta_{pitch}\omega_{pitch}(I_z + A_{55}(\omega_{pitch})) \\
B_{66_v} &= \frac{I_z + A_{66}(0)}{T_{yaw}}
\end{aligned} \tag{2.108}$$

where the time constants typically are between $100 - 250s$ in surge, sway, and yaw. Furthermore, the damping ratios are generally chosen as $\zeta_{heave} = \zeta_{pitch} = 0$ and $\zeta_{roll} = 0.1$.

Wave excitation forces

With incident regular waves and a vessel restrained from oscillations, there are generated loads due to the dynamic pressure field induced by the waves. The loads can be divided into Froude-Krylov and diffraction forces. The Froude-Krylov forces are related to the undisturbed pressure field induced by an undisturbed wave, while the diffraction forces are generated because the vessel affects the undisturbed pressure field (Faltinsen, 1990). According to linear wave theory, a velocity potential of a sine wave propagating along the x-axis is formulated as follows

$$\Phi = \frac{g\zeta_a}{\omega} e^{kz} sin(\omega t - kx + \epsilon) \tag{2.109}$$

where ζ_a is the wave amplitude, ω is the wave frequency, k is the wave number, ϵ is a random phase angle, z is the vertical distance relative to the surface and x is the propagation of the wave. The Froude-Krylov pressure for a regular wave can then be found from the velocity potential as follows

$$p_{FK} = \rho_w \frac{\partial \Phi}{\partial t} = g\zeta_a e^{kz} cos(\omega t - kx + \epsilon) \tag{2.110}$$

Considering that an irregular sea state can be found by linearly superposing the contribution from a series of regular waves, the Froude-Kyrlov pressure becomes the following

$$p_{FK} = \sum_{i=1}^{N} \rho_w g \zeta_{a,i} e^{k_i z} cos(\omega_i t - k_i x + \epsilon_i) \tag{2.111}$$

where N is the number of wave components. By assuming that the vessel has small characteristic lengths relative to the incoming wavelengths, the following approximation is given for the wave excitation forces (Faltinsen, 1990)

$$\mathbf{F} = F_1\mathbf{i} + F_2\mathbf{j} + F_3\mathbf{k} \tag{2.112}$$

where

$$F_i = -\int\int_S p_{FK} n_i ds + A_{i1}a_1 + A_{i2}a_2 + A_{i3}a_3 \tag{2.113}$$

Here S refers to the integration over the wetted surface of the vessel, n_i is a unit vector perpendicular to the wetted surface, A_{ij} are the added mass coefficients and a_i is the wave acceleration at the geometrical mass center of the vessel.

In addition to the first-order solution presented above, higher order theories are utilized to give a more exact solution to the nonlinear wave problem. Especially second-order effects such as mean drift loads, difference frequency loads and sum frequency loads are important. The wave-drift forces are related to the ability of a structure to generate waves, namely the radiated and diffracted waves (Faltinsen, 1990). Difference frequency loads are related to the nonlinear terms that contain the difference between the frequencies of different wave components. These loads are relevant for motion with large resonance periods. Sum frequency loads are related to the nonlinear terms that contain frequencies higher than the frequency of an individual wave component. These loads are relevant for motion with small resonance periods. For a thorough explanation of the derivation of mean drift loads, difference frequency loads and sum frequency loads acting on structures, refer to Faltinsen (1990).

2.4 Winch modeling

A winch system is a multidisciplinary system consisting of mechanical, electrical and/or hydraulic and cybernetic systems. With the MCMR Lab in consideration, the modeling process of a power unit is related to an electrical system. Furthermore, the development of the mechanical dynamics regarding wire and reel is presented.

2.4.1 Wire

In Pedersen and Pedersen (2005) a common method for modeling wires is described. The wire is divided into n segments of equal length in order to generate a deflection form that reflects the behavior of a wire. Each element has two nodes, one at each end, implying that there are $n+1$ nodes. The elements and nodes are therefore enumerated from $i = 1, 2, ..., n$ and $i = 0, 1, ..., n$, respectively, where the ith element is connected to the $(i-1)$th and ith node. The total mass and forces acting along the wire are distributed to the nodes and the sum over the ith element is defined as concentrated in the ith node. Additional concentrated forces acting on the wire are considered to act on a node.

As stated in Pedersen and Pedersen (2005), the finite element method (FEM) has been the most common method for modeling cable motion. However, since it is a comprehensive method where algebraic expressions are difficult to derive without a set of simplifications, another modeling approach is suggested. This alternative method divides the wire into a series of mass-spring-damper systems in order to approximate its behavior. In Pedersen and Pedersen (2005), FEM analysis was compared to the simplified approach and it showed satisfying results in regard to the average difference between in the position of the corresponding nodes in the two models. It should be noted that there are uncertainties regarding the correctness of the FEM model due to the simplifications that were made. However, the lumped mass-spring-damper approach yielded satisfactory results. Another point to take into consideration is that the mass matrix in the FEM model contains off-diagonal elements that impl slower solving of the equations when compared to the lumped mass-spring-damper model that has a diagonal mass matrix, i.e. a smaller bandwidth. A general drawing of a mass-spring-damper element is given in Figure 2.11

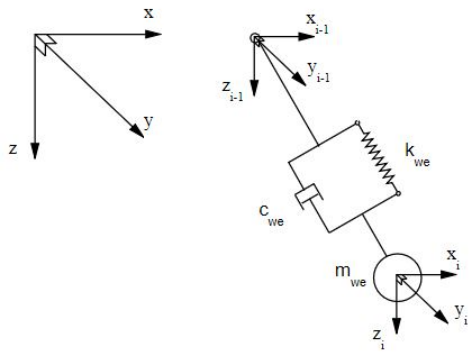

Figure 2.11: A general wire element

Wire dynamics

In Sørensen (2013), a set of assumptions regarding the modeling of cables are presented and are relevant when developing a wire model. The wire is assumed to have no bending stiffness or torsional stiffness, implying that only axial stiffness is relevant. Hence, the elements are considered to be bar elements rather than beam elements, which indicates a simplified analysis. Furthermore, the axial tension is assumed small enough to operate within the linear range of the stress and strain relationship, and the cross-sectional area of the wire is assumed to not change significantly due to axial deformations.

Considering the simplified wire model presented in Pedersen and Pedersen (2005), the force in a spring can be expressed as the relationship between its stiffness and elongation from its initial length. For a wire element, the spring force can be expressed as

$$F_{s_{we}} = k_{we} r_{we} \tag{2.114}$$

where the k_w is the wire stiffness and r_{we} is the elongation of the wire element. The stiffness of the wire can be related to the elasticity modulus E, the cross-sectional area A_w and the length of a wire element L_{we}.

$$k_{we} = \frac{EA_w}{L_{we}} \tag{2.115}$$

The damping is assumed to be linear and can be expressed as a relationship between the damping coefficient d_w and the elongation rate of a wire element $\dot{r}_{we}$

$$F_{d_{we}} = d_w \dot{r}_{we} \tag{2.116}$$

For a mass-spring-damper system, the critical damping is given as

$$c_{cr} = 2m_{we}\sqrt{\frac{k_w}{m_{we}}} = 2\sqrt{k_w m_{we}} \tag{2.117}$$

and through the definition of the damping ratio ζ, the expression of the damping in the system can be found as follows

$$\zeta = \frac{c}{c_{cr}} \Rightarrow c = 2\zeta\sqrt{k_w m_{we}} \tag{2.118}$$

In Skjong and Pedersen (2014), the damping ratio is chosen as $\zeta = 5$ to create an over-damped system in order to represent the dynamics of a wire.

The last factor in the expression of the damping force is found by evaluating the elongation of each wire element

$$r_{we} = \sqrt{(x_i - x_{i-1})^2 + (y_i - y_{i-1})^2 + (z_i - z_{i-1})^2} - L_{we} \tag{2.119}$$

The elongation rate is found by taking the derivative of the elongation

$$\begin{aligned} \dot{r}_{we} = & \frac{(x_i - x_{i-1})}{\sqrt{(x_i - x_{i-1})^2 + (y_i - y_{i-1})^2 + (z_i - z_{i-1})^2}}(\dot{x}_i - \dot{x}_{i-1}) \\ & + \frac{(y_i - y_{i-1})}{\sqrt{(x_i - x_{i-1})^2 + (y_i - y_{i-1})^2 + (z_i - z_{i-1})^2}}(\dot{y}_i - \dot{y}_{i-1}) \\ & + \frac{(z_i - z_{i-1})}{\sqrt{(x_i - x_{i-1})^2 + (y_i - y_{i-1})^2 + (z_i - z_{i-1})^2}}(\dot{z}_i - \dot{z}_{i-1}) \\ & - \dot{L}_{we} \end{aligned} \tag{2.120}$$

Notice that the length of the wire element varies with time since the length of the total paid out wire changes while the number of elements remains constant. Since the model operates with both body-fixed reference frames and the inertial reference frame, rotation matrices are used to transform the forces and velocities into the correct reference frames. The angles between the nodes are expressed as follows

$$\psi = tan^{-1}(\frac{y_i - y_{i-1}}{x_i - x_{i-1}}) \tag{2.121}$$

$$\theta = tan^{-1}(\frac{z_i - z_{i-1}}{x_i - x_{i-1}}) \tag{2.122}$$

$$\phi = tan^{-1}(\frac{z_i - z_{i-1}}{y_i - y_{i-1}}) \tag{2.123}$$

2.4.2 Reel dynamics

A generic reel with wire is illustrated in Figure 2.12, and it is necessary to develop a method for expressing the reel dynamics.

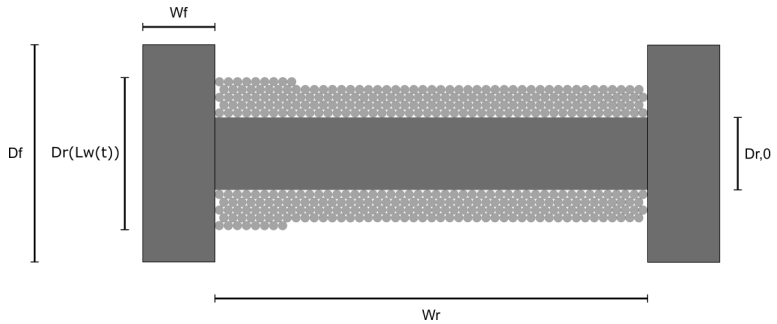

Figure 2.12: Generic tugger winch reel dimensions

Obviously, the wire influences the dynamics of the reel as it is connected to and stored onto the reel. Hence, the reel is affected by the amount of wire that is stored onto it at any given time instant. Consequently, the contribution from the wire must be included in the model to express the complete reel dynamics. In Skjong and Pedersen (2014), a reel model is developed by finding an expression for how the diameter of the reel changes with the amount of wire stored onto it. This is done by setting the storage volume of a full reel equal to the volume of the wire stored onto it in that scenario. Note that this method is a simplification of the problem, but that it aims to approximate the behavior of the system.

$$V_w = V_r \iff \frac{D_w^2}{4}\pi L_{w,r} = \frac{D_{r,full}^2 - D_{r,0}^2}{4}\pi w_r f_w \tag{2.124}$$

Here V_w and V_r are the volumes of the wire and the reel storage capacity, respectively, while f_w denotes the packing factor, which is related to the reduced storage capacity due to air gaps between the wire layers. Depending on how compactly the wire is packed onto the reel, the packing factor is somewhere in the range $0 < f_w < 1$. Given the most optimal configuration, as illustrated in Figure 2.13, the packing factor is given as

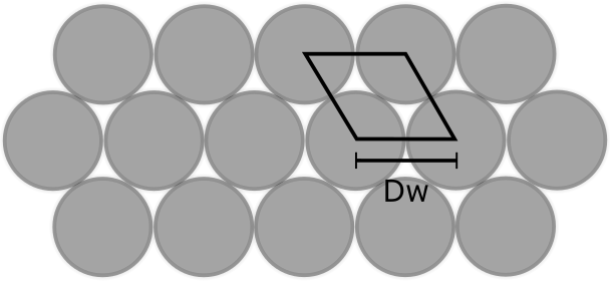

Figure 2.13: Optimal wire configuration

$$f_w = \frac{\frac{\pi D_w^2}{4}}{\frac{\sqrt{3}}{2}D_w^2} = \frac{\pi}{2\sqrt{3}} \approx 0.9069 \tag{2.125}$$

by comparing the volume of the parallelogram and a circle. Going back to Equation 2.124, the time-varying reel diameter is acquired as a function of the wire length stored onto the reel as follows

$$D_r(L_{w,r}(t)) = \sqrt{\frac{L_{w,r(t)}D_w^2}{w_r f_w} + D_{r,0}^2} \tag{2.126}$$

With the time-varying reel diameter, the moment of inertia of the reel can be calculated as follows

$$I_{reel}(t) = I_{rod} + 2I_{flange} + I_{wire}(t) \tag{2.127}$$

The moments of inertia for a cylinder and a hollow cylinder are the following

$$I_{cyl} = \frac{1}{2}mr^2 = \frac{1}{8}mD^2 \tag{2.128}$$

$$I_{cyl_{hollow}} = \frac{1}{2}m(r_2^2 + r_1^2) = \frac{1}{8}m(D_2^2 + D_1^2) \tag{2.129}$$

Assuming that the wire forms a hollow cylinder around the reel, the moment of inertia in Equation 2.127 is written as

$$I_{reel}(t) = \frac{1}{8}m_{rod}D_{r,0}^2 + 2\frac{1}{8}m_{flange}D_{r,full}^2 + \frac{1}{8}\rho_w L_{w,r}(t)(D^2(L_{w,r}(t)) + D_{r,0}^2) \tag{2.130}$$

The wire velocity can be expressed by the radius and angular velocity of the reel

$$\dot{L}_w = \frac{D_r(L_{w,r}(t))}{2}\omega_r \tag{2.131}$$

With the wire velocity, the length of each wire element can be calculated by integrating the wire velocity and dividing it by the number of elements in the wire model.

2.4.3 Electric power unit

As previously mentioned, the power unit will be modeled as an electric motor that converts electrical energy into the mechanical energy that drives the reel. In relation to the models derived in Gyberg (2017), the electric motor is modeled as an RL-circuit with a GY-element that transforms the voltage and current into torque and rotational velocity. The constitutive relations of the GY-element are given in Equation 2.132 and Equation 2.133. Here r_1 and r_2 are the torque and speed constants given in $\frac{Nm}{A}$ and $\frac{RPM}{V}$, respectively.

$$\tau_m = r_1 i \tag{2.132}$$

$$u = \frac{1}{r_2}\omega_m, \tag{2.133}$$

Considering reduction through the inclusion of a gear, TF-elements are introduced to apply the reduction coefficient. The reduction coefficient is related to the ratio between the radii or the number of teeth on two cogwheels (Pedersen and Engja, 2014). Additional features such as belt transmissions apply further reductions in a similar manner. Note that friction can be included in the TF-elements through the use of an efficiency factor η provided by component specification sheets. The moments of inertia of the different components of the power unit are implemented in I-elements.

2.5 Motion compensation

Marine vessels are subjected to a range of external forces such as wave and wind loads that induce motion in the six degrees of freedom. During a crane lift operation, the motions affect the movement of the lifted object and could lead to dangerous situations if not handled correctly. A variety of motion compensation and restriction methods are used to limit the movement of the lifted object.

2.5.1 Heave compensation

DNV (2011) states that the implementation of a heave compensation device is the most common method to compensate for the vertical motion of the vessel during a crane lift operation. The device can be used to control the tension in the wire and the motion of the lifted object. To perform this form of motion compensation, both passive and active methods are utilized. A passive heave compensation system involves the use of a spring-damper system while an active system can include active components such as controlled winches and pistons. As stated in Driscoll et al.

(1998), passive systems have been widely employed due to their simplicity. The systems are practically autonomous and are easy to maintain. On the other hand, in Woodacre et al. (2015), a combination of field experience and simulations implies that passive systems are limited to roughly 80% decoupling of the heave motion. To further increase the decoupling, active systems must be incorporated. Furthermore, a passive heave compensation system is unable to compensate for the relative motion between two independently moving reference frames and renders ship to ship cargo transfers ineffective. The inclusion of active heave compensation systems can improve the performance of the motion compensation but comes at the cost of requiring additional equipment such as computers, sensor, motors and hydraulic systems. Due to the added number of components, these systems can become complex, expensive and difficult to maintain.

2.5.2 Constant tension

Another approach called constant tension is performed by controlling the tension in a wire to remain at a predefined force set-point. Passive systems have commonly been utilized due to their simplicity, but as stated in Chen et al. (2017) they have drawbacks such as precision during rough sea states and power consumption due to the cooling of the hydraulic system. Therefore, as most crane winch systems are equipped with load cells that measure the tension in the wire continuously, active constant tension (ACT) systems with force feedback can be developed to improve the performance. Since PID controllers are common in the industry, they are often used to control the tension in the wire. Consequently, ACT can be implemented in tugger wire systems to limit the pendulum motion of lifted objects while preventing snap loads. Note that snap loads are characterized by a spike in tension over a short period of time when slack wire reengages tension.

2.5.3 Inverse dynamics controller

As derived in Siciliano et al. (2009), an inverse dynamics operational controller can be implemented when it is of interest to track an operational space reference. The operational space refers to the space in which the crane task is specified and is most often given in a Cartesian reference frame. It should be distinguished from the joint space that describes the configuration of the crane with the generalized coordinates. As the name indicates, the controller is based on the dynamics of the system and the previously developed equations of motion are used as a basis for the development of a control law. Recalling that the equations of motion for the crane can be written as

$$\mathbf{B}(\mathbf{q})\ddot{\mathbf{q}} + \mathbf{C}(\mathbf{q}, \dot{\mathbf{q}})\dot{\mathbf{q}} + \mathbf{g}(\mathbf{q}) = \boldsymbol{\tau}$$

it is shown in Siciliano et al. (2009) that an inverse dynamics linearizing control can be chosen as

$$\begin{aligned} \boldsymbol{\tau} &= \mathbf{B}(\mathbf{q})\mathbf{y} + \mathbf{n}(\mathbf{q}, \dot{\mathbf{q}}) \\ \mathbf{n}(\mathbf{q}, \dot{\mathbf{q}}) &= \mathbf{C}(\mathbf{q}, \dot{\mathbf{q}})\dot{\mathbf{q}} + \mathbf{g}(\mathbf{q}) \end{aligned} \tag{2.134}$$

to give a system of double integrators where

$$\ddot{\mathbf{q}} = \mathbf{y} \tag{2.135}$$

It should be noted that the system in Equation 2.134 is linear and decoupled with respect to the defined input $\mathbf{y}$ (Siciliano et al., 2009). This implies that the input element y_i only affects the generalized coordinate q_i independent of the movement of the other joints. Hence, the problem is reduced to finding a control law $\mathbf{y}$ such that it is able to track the trajectory given by the desired

position $\mathbf{r}_d(t)$, velocity $\dot{\mathbf{r}}_d(t)$, and acceleration $\ddot{\mathbf{r}}_d(t)$. Recalling the relationship between the velocity and generalized coordinates shown in Equation 2.42, the acceleration can be expressed as

$$\ddot{\mathbf{r}} = \mathbf{J}(\mathbf{q})\ddot{\mathbf{q}} + \dot{\mathbf{J}}(\mathbf{q})\dot{\mathbf{q}} \tag{2.136}$$

and then solved for the generalized acceleration as follows

$$\ddot{\mathbf{q}} = \mathbf{J}^{-1}(\mathbf{q})(\ddot{\mathbf{r}} - \dot{\mathbf{J}}(\mathbf{q})\dot{\mathbf{q}}) \tag{2.137}$$

Then, by choosing

$$\mathbf{y} = \mathbf{J}^{-1}(\mathbf{q})(\ddot{\mathbf{r}}_d + \mathbf{K}_d\dot{\tilde{\mathbf{r}}} + \mathbf{K}_p\tilde{\mathbf{r}} - \dot{\mathbf{J}}(\mathbf{q})\dot{\mathbf{q}}) \tag{2.138}$$

and inserting Equation 2.137 and Equation 2.138 into Equation 2.135, the error dynamics are are given by the following expression

$$\ddot{\tilde{\mathbf{r}}} + \mathbf{K}_d\dot{\tilde{\mathbf{r}}} + \mathbf{K}_p\tilde{\mathbf{r}} = 0 \tag{2.139}$$

where $\mathbf{K}_d$ and $\mathbf{K}_p$ are positive definite diagonal matrices that are tunable and therefore determine the operational space error convergence rate to zero. Note that the proposed controller is susceptible to parameter uncertainties. Thus, a robust configuration is proposed in Appendix C to account for unmodeled effects.

2.6 Software

This section provides a short introduction to the different software that is utilized during the development of the simulation models in this thesis.

2.6.1 20-Sim

20-Sim is a modeling and simulation program developed by Controllab that allows a high-level implementation of models through a graphical editor. It supports the use of bond graphs and block diagrams while having an efficient numerical analysis and simulation capability (Duindam et al., 2009). Furthermore, its library contains the standard bond graph and block diagram components. Elements and submodels of various physical domains are easily interfaced together and provide a platform that is ideal for a multi-disciplinary system such as an offshore crane.

2.6.2 Maple

Maple is a math software developed by Maplesoft that is capable of performing symbolic computations for complex mathematical expressions. Hence, the derivation of the algebraic expressions that are utilized in the simulation models can be calculated in Maple. Furthermore, it supports automatic code generation for a variety of programming languages, including C. Note that the code generation is optimized with respect to computational efficiency. Hence, it provides a platform for the development of a dynamic-link library (DLL) files that are necessary for the process of reducing the computational power that is required when performing simulations of crane operations.

2.6.3 MATLAB

MATLAB is a software developed by MathWorks that provides a platform for numerical computing. It is a powerful tool with respect to executing matrix operations and plotting functions. Hence, in this thesis, it is utilized in tasks regarding the processing of text files and the creation of graphical visualizations of simulation data.

2.6.4 Visual Studio

Visual Studio is a platform for the development of computer programs and is supplied by Microsoft. It provides an environment that is suitable for building DLL-files from the C-code that is generated in Maple. Hence, computationally intensive operations can be carried out in the DLL-files rather than by the solver in 20-Sim. Consequently, the overall simulation times can be reduced.

3 | Crane modeling

In this chapter, the procedure of developing a simulation model of the crane and its auxiliary equipment will be described through the use of the theory presented in Chapter 2. The crane simulation model is heavily based on the model developed in Gyberg (2017), but the process of deriving it is presented to serve as a basis for the understanding of the inner workings as it is the cornerstone of the thesis. The crane geometry established in Gyberg (2017) is depicted in Figure 3.1. It should be noted that the illustration of the crane is for a case where the lower crane boom is longer than the one that currently is mounted in the MCMR Lab. Regardless, the notation of parameters that indicate the positions of the centers of gravity[1] are the same for the two crane boom configurations. Furthermore, the process of implementing auxiliary equipment related to actuators and winch systems is presented in this chapter. The relevant parameters related to the model crane are given in Appendix A.1.

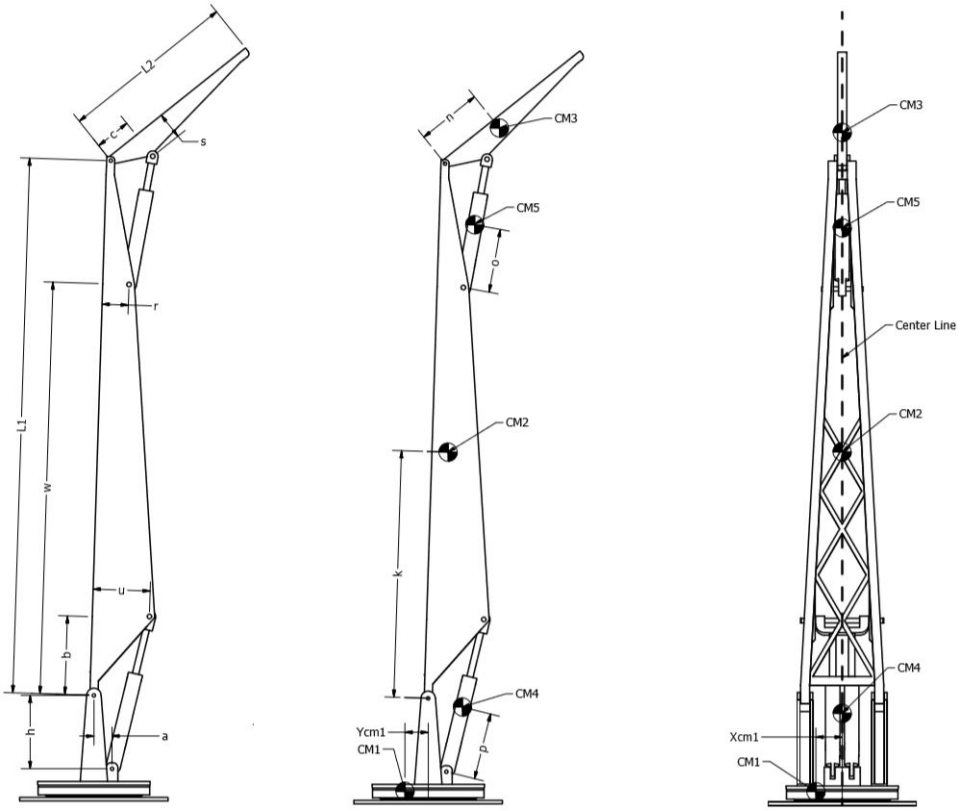

(a) Crane dimensions (b) CG in the yz-plane (c) CG in the xz-plane

Figure 3.1: Crane geometry. Taken from Gyberg (2017)

[1]Note that the centers of mass depicted in Figure 3.1 are equivalent to the centers of gravity in a uniform gravitational field (Millikan, 1903).

3.1 Generalized coordinates

The crane is designed with a rotating base and two crane booms that can be moved by pistons. Accordingly, the system has three degrees of freedom and the three angles θ_1, θ_2, and θ_3, depicted in Figure 3.2, are a set of generalized coordinates that are suitable in regard to uniquely describing the position and orientation of the system. The generalized coordinates are therefore defined as

$$\mathbf{q} = \begin{bmatrix} q_1 \\ q_2 \\ q_3 \end{bmatrix} = \begin{bmatrix} \theta_1 \\ \theta_2 \\ \theta_3 \end{bmatrix} \tag{3.1}$$

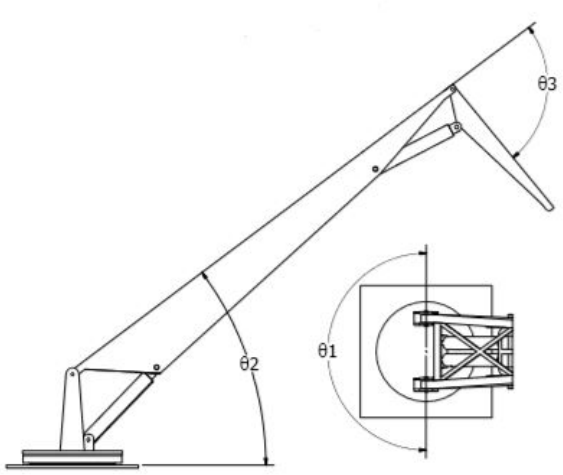

Figure 3.2: Crane with generalized coordinates. Taken from Gyberg (2017)

3.2 Crane boom actuators

As stated in Gyberg (2017), the crane boom actuators have large masses and should be included in the dynamic model of the crane. Hence, their orientation in terms of the generalized coordinates and the crane geometry must be expressed. The two angles δ_1 and δ_2 are defined as the orientation of the lower and upper actuator, respectively, with regard to the xy-plane. The geometries of the lower and upper actuators are presented in Figure 3.3 and are used to develop the expressions of the angles.

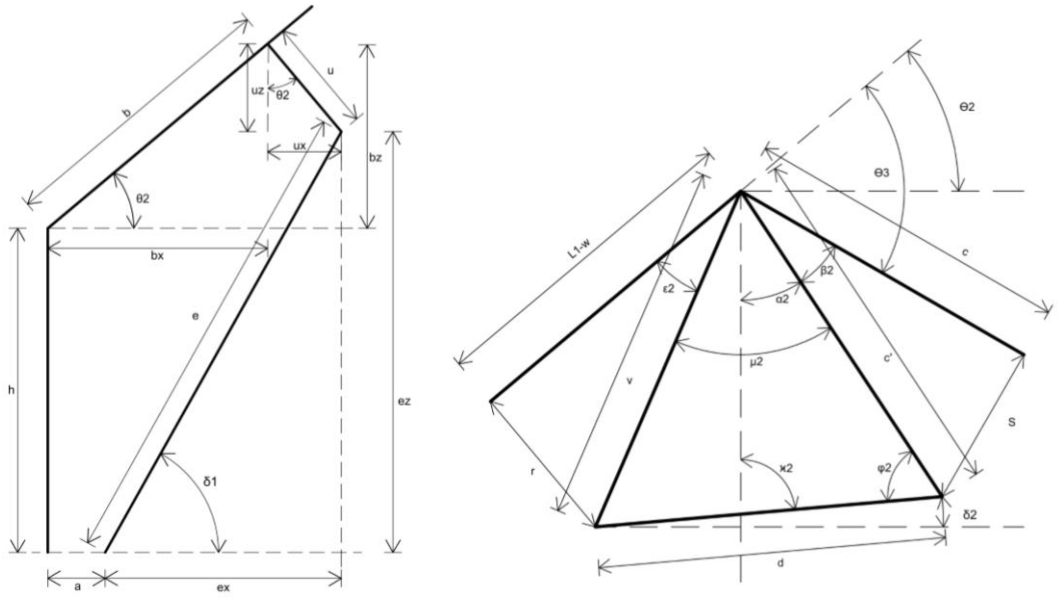

(a) Lower actuator (b) Upper actuator

Figure 3.3: Actuator geometries. Taken from Gyberg (2017)

For the lower actuator, the following can be derived

$$
\begin{aligned}
u_x &= sin(\theta_2) \cdot u \\
u_z &= cos(\theta_2) \cdot u \\
b_x &= cos(\theta_2) \cdot b \\
b_z &= cos(\theta_2) \cdot b \\
e_x &= b_x + u_x - a \\
e_z &= h + b_z - u_z \\
e &= \sqrt{e_x^2 + e_z^2}
\end{aligned}
$$

giving the angle

$$
\delta_1(\theta_2) = sin^{-1}\left(\frac{h + cos(\theta_2) \cdot b - cos(\theta_2) \cdot u}{\sqrt{(cos(\theta_2) \cdot b + sin(\theta_2) \cdot u - a)^2 + (h + cos(\theta_2) \cdot b - cos(\theta_2) \cdot u)^2}} \right) \tag{3.2}
$$

To derive the angle for the upper actuator, the following can be shown

$$
\begin{aligned}
c' &= \sqrt{s^2 + c^2} \\
v &= \sqrt{r^2 + (L1 - w)^2} \\
\beta_2 &= sin^{-1}\Big(\frac{s}{c'}\Big) \\
\epsilon_2 &= sin^{-1}\Big(\frac{r}{v}\Big) \\
\mu_2 &= \pi + \theta_3 - \beta_2 - \epsilon_2 \\
d &= \sqrt{v^2 + c'^2 - 2v \cdot c' \cdot cos(\mu_2)} \\
\phi_2 &= cos^{-1}\Big(\frac{c'^2 + d^2 - v^2}{2c'd}\Big) \\
\alpha_2 &= \frac{\pi}{2} - \beta_2 + \theta_2 + \theta_3 \\
\kappa_2 &= \pi - \alpha_2 - \phi_2
\end{aligned}
$$

yielding

$$\delta_2(\theta_2, \theta_3) = \frac{\pi}{2} - \kappa_2 = \theta_2 + \theta_3 - sin^{-1}\Big(\frac{s}{c'}\Big) + cos^{-1}\Big(\frac{c'^2 + d^2 - v^2}{2c'd}\Big) \tag{3.3}$$

3.3 Position vectors

As previously stated, the movement of all the rigid body parts of the crane must be referenced to an inertial reference frame due to the criteria of Newton's laws. Since it is most trivial to express the positions vectors to the centers of gravity in body-fixed frames, rotation matrices are used to transform them into the inertial frame. Therefore, a set of body-fixed reference frames are defined on the crane, as illustrated in Figure 3.4.

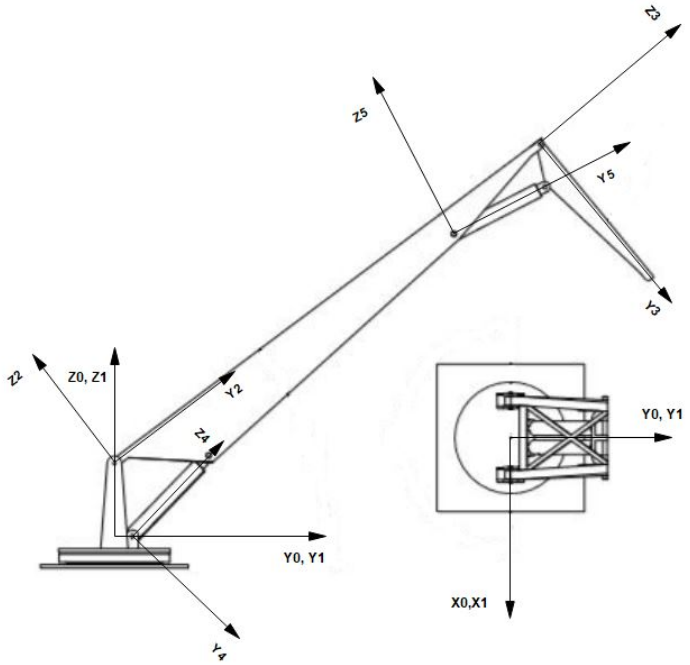

Figure 3.4: Crane with reference frames

To begin with, the reference frames must be related to each other through position vectors. In Section 2.1.1 the notation of the position vectors was defined, and the following relations between the reference frames can be derived from the geometry given in Figure 3.1

$$\mathbf{r}^0_{1/0} = \begin{bmatrix}0\\0\\0\end{bmatrix}, \quad \mathbf{r}^1_{2/1} = \begin{bmatrix}0\\0\\h\end{bmatrix}, \quad \mathbf{r}^2_{3/2} = \begin{bmatrix}0\\L_1\\0\end{bmatrix}, \quad \mathbf{r}^1_{4/1} = \begin{bmatrix}0\\a\\0\end{bmatrix}, \quad \mathbf{r}^2_{5/2} = \begin{bmatrix}0\\w\\-r\end{bmatrix} \tag{3.4}$$

Furthermore, the position vectors to the centers of gravity must be expressed, and in the body-fixed frames, they can be defined as

$$\mathbf{r}^1_{cg_1/1} = \begin{bmatrix}X_{cg_1}\\Y_{cg_1}\\0\end{bmatrix}, \quad \mathbf{r}^2_{cg_2/2} = \begin{bmatrix}0\\k\\0\end{bmatrix}, \quad \mathbf{r}^3_{cg_3/3} = \begin{bmatrix}0\\n\\0\end{bmatrix}, \quad \mathbf{r}^4_{cg_4/4} = \begin{bmatrix}0\\0\\p\end{bmatrix}, \quad \mathbf{r}^5_{cg_5/5} = \begin{bmatrix}0\\o\\0\end{bmatrix} \tag{3.5}$$

The next step is to relate the position vectors to the inertial reference frame. All the relevant rotation matrices can be defined with the generalized coordinates and the two actuator angles

$$\begin{aligned}
\mathbf{R}^0_1 &= \begin{bmatrix} cos(\theta_1) & sin(\theta_1) & 0\\ -sin(\theta_1) & cos(\theta_1) & 0\\ 0 & 0 & 1\end{bmatrix}, \quad \mathbf{R}^1_2 = \begin{bmatrix}1 & 0 & 0\\ 0 & cos(\theta_2) & -sin(\theta_2)\\ 0 & sin(\theta_2) & sin(\theta_2)\end{bmatrix},\\
\mathbf{R}^2_3 &= \begin{bmatrix}1 & 0 & 0\\ 0 & cos(\theta_3) & -sin(\theta_3)\\ 0 & sin(\theta_3) & sin(\theta_3)\end{bmatrix}, \quad \mathbf{R}^1_4 = \begin{bmatrix}1 & 0 & 0\\ 0 & cos(\delta_1) & -sin(\delta_1)\\ 0 & sin(\delta_1) & sin(\delta_1)\end{bmatrix},\\
\mathbf{R}^1_5 &= \begin{bmatrix}1 & 0 & 0\\ 0 & cos(\delta_2) & -sin(\delta_2)\\ 0 & sin(\delta_2) & sin(\delta_2)\end{bmatrix}
\end{aligned} \tag{3.6}$$

These rotation matrices are combined such that the body-fixed frames can be rotated into the orientation of the inertial frame. The combinations of rotation matrices that are required for the previously defined reference frames are stated below

$$\mathbf{R}^0_2 = \mathbf{R}^0_1\mathbf{R}^1_2, \quad \mathbf{R}^0_3 = \mathbf{R}^0_2\mathbf{R}^2_3, \quad \mathbf{R}^0_4 = \mathbf{R}^0_1\mathbf{R}^1_4, \quad \mathbf{R}^0_5 = \mathbf{R}^0_1\mathbf{R}^1_5 \tag{3.7}$$

With the definition of the rotation matrices, the previously defined position vectors can be transformed into the inertial reference frame with the general expression that was defined in Equation 2.2, yielding

$$\begin{aligned}
\mathbf{r}^0_{2/0} &= \mathbf{r}^0_{1/0} + \mathbf{R}^0_1\mathbf{r}^1_{2/1}, \quad & \mathbf{r}^0_{3/0} &= \mathbf{r}^0_{2/0} + \mathbf{R}^0_2\mathbf{r}^2_{3/2},\\
\mathbf{r}^0_{4/0} &= \mathbf{r}^0_{1/0} + \mathbf{R}^0_4\mathbf{r}^1_{4/1}, \quad & \mathbf{r}^0_{5/0} &= \mathbf{r}^0_{2/0} + \mathbf{R}^0_2\mathbf{r}^2_{5/2}
\end{aligned} \tag{3.8}$$

$$\begin{aligned}
\mathbf{r}^0_{cg_1/0} &= \mathbf{r}^0_{1/0} + \mathbf{R}^0_1\mathbf{r}^1_{cg_1/1}, \quad & \mathbf{r}^0_{cg_2/0} &= \mathbf{r}^0_{2/0} + \mathbf{R}^0_2\mathbf{r}^2_{cg_2/2},\\
\mathbf{r}^0_{cg_3/0} &= \mathbf{r}^0_{3/0} + \mathbf{R}^0_3\mathbf{r}^3_{cg_3/3}, \quad & \mathbf{r}^0_{cg_4/0} &= \mathbf{r}^0_{4/0} + \mathbf{R}^0_4\mathbf{r}^4_{cg_4/4},\\
\mathbf{r}^0_{cg_5/0} &= \mathbf{r}^0_{5/0} + \mathbf{R}^0_5\mathbf{r}^5_{cg_5/5}
\end{aligned} \tag{3.9}$$

3.4 Defining the Jacobian matrices

With the general expressions derived in Section 2.1.5, the Jacobian matrices that link the linear and angular velocities of the centers of gravity to the generalized coordinates can be expressed. To begin with, the unit vectors that define the direction that the crane joints are able to displace must be defined. The crane base rotates about the z-axis while the two crane booms rotate about their local x-axes. Hence, three unit vectors are required. Since it is straight forward to express the unit vectors in the local reference frames, they must be rotated into the inertial reference frame as follows

$$\mathbf{e}_1^0 = \mathbf{R}_1^0\mathbf{e}_1^1 = \mathbf{R}_1^0\mathbf{k}, \quad \mathbf{e}_2^0 = \mathbf{R}_2^0\mathbf{e}_2^2 = \mathbf{R}_2^0\mathbf{i}, \quad \mathbf{e}_3^0 = \mathbf{R}_3^0\mathbf{e}_3^3 = \mathbf{R}_3^0\mathbf{i} \tag{3.10}$$

where $\mathbf{i}$ and $\mathbf{k}$ are the unit vectors in the local x- and z-directions, respectively. The Jacobian matrices can then be expressed as follows

$$\begin{aligned}
\mathbf{J}_1 &= \begin{bmatrix} \mathbf{e}_1^0 \times (\mathbf{r}_{cg_1/0}^0 - \mathbf{r}_{1/0}^0) & \mathbf{0}_{3x2} \\ \mathbf{e}_1^0 & \mathbf{0}_{3x2} \end{bmatrix} \\
\mathbf{J}_2 &= \begin{bmatrix} \mathbf{e}_1^0 \times (\mathbf{r}_{cg_2/0}^0 - \mathbf{r}_{1/0}^0) & \mathbf{e}_2^0 \times (\mathbf{r}_{cg_2/0}^0 - \mathbf{r}_{2/0}^0) & \mathbf{0}_{3x1} \\ \mathbf{e}_1^0 & \mathbf{e}_2^0 & \mathbf{0}_{3x1} \end{bmatrix} \\
\mathbf{J}_3 &= \begin{bmatrix} \mathbf{e}_1^0 \times (\mathbf{r}_{cg_3/0}^0 - \mathbf{r}_{1/0}^0) & \mathbf{e}_2^0 \times (\mathbf{r}_{cg_3/0}^0 - \mathbf{r}_{2/0}^0) & \mathbf{e}_3^0 \times (\mathbf{r}_{cg_3/0}^0 - \mathbf{r}_{3/0}^0) \\ \mathbf{e}_1^0 & \mathbf{e}_2^0 & \mathbf{e}_3^0 \end{bmatrix} \\
\mathbf{J}_4 &= \begin{bmatrix} \mathbf{e}_1^0 \times (\mathbf{r}_{cg_4/0}^0 - \mathbf{r}_{1/0}^0) & \mathbf{e}_2^0 \times (\mathbf{r}_{cg_4/0}^0 - \mathbf{r}_{2/0}^0) & \mathbf{0}_{3x1} \\ \mathbf{e}_1^0 & \mathbf{e}_2^0 & \mathbf{0}_{3x1} \end{bmatrix} \\
\mathbf{J}_5 &= \begin{bmatrix} \mathbf{e}_1^0 \times (\mathbf{r}_{cg_5/0}^0 - \mathbf{r}_{1/0}^0) & \mathbf{e}_2^0 \times (\mathbf{r}_{cg_5/0}^0 - \mathbf{r}_{2/0}^0) & \mathbf{e}_3^0 \times (\mathbf{r}_{cg_5/0}^0 - \mathbf{r}_{3/0}^0) \\ \mathbf{e}_1^0 & \mathbf{e}_2^0 & \mathbf{e}_3^0 \end{bmatrix}
\end{aligned} \tag{3.11}$$

3.5 Mass and inertia matrix

The last step before the equations of motion can be developed is to define the mass and inertia matrices $\mathbf{M}_j$. As stated in Section 2.1.3, the inertia tensor is dependent on the configuration of the rigid body with respect to the inertial frame. Therefore, the inertia tensors of each rigid body in their body-fixed frames must be transformed as defined in Equation 2.14, yielding

$$\mathbf{I}_1^0 = \mathbf{R}_1^0\mathbf{I}_1^1\mathbf{R}_0^1, \quad \mathbf{I}_2^0 = \mathbf{R}_2^0\mathbf{I}_2^2\mathbf{R}_0^2, \quad \mathbf{I}_3^0 = \mathbf{R}_3^0\mathbf{I}_3^3\mathbf{R}_0^3, \quad \mathbf{I}_4^0 = \mathbf{R}_4^0\mathbf{I}_4^4\mathbf{R}_0^4, \quad \mathbf{I}_5^0 = \mathbf{R}_5^0\mathbf{I}_5^5\mathbf{R}_0^5 \tag{3.12}$$

Since the mass is independent of the orientation of a body, the mass and inertia matrix of body j can be formulated as shown below

$$\mathbf{M}_j = \begin{bmatrix} m_j\mathbf{I}_{3x3} & \mathbf{0}_{3x3} \\ \mathbf{0}_{3x3} & \mathbf{I}_j^0 \end{bmatrix} \tag{3.13}$$

3.6 Kinematics

As stated earlier, the kinematics disregard the forces that induce the motion of a body and will be defined inside an IC-field. This implies that the generalized forces $\boldsymbol{\tau}$ and the restoring force and moment vector $\mathbf{g}(\mathbf{q})$ in the equations of motion can be excluded at this stage. Therefore, only the inertia matrix $\mathbf{B}(\mathbf{q})$ and centripetal and Coriolis matrix $\mathbf{C}(\mathbf{q}, \dot{\mathbf{q}})$ are of interest in the IC-field. They are found as explained in Section 2.1.6 and the algebraic expressions are derived with the use of a Maple-script developed in Gyberg (2017). The Maple-script has been slightly modified and is referred to in Appendix B.

Due to the complexity of the expressions in the inertia and centripetal and Coriolis matrices, they will not be solved directly in 20-Sim but rather processed through a DLL-file. It is done to reduce the time required by the solver in 20-Sim to perform the calculations of every time step during a simulation. The required C-code is generated by exporting the algebraic expressions derived in Maple, and the process of developing the DLL-file is described in Rokseth (2014). In addition to the steps described in Rokseth (2014), a MATLAB-script has been made to process the text file containing the C-code such that issues regarding the use of a DLL-file in 20-Sim are circumvented. Hence, rather than compiling the C-code using Cygwin, the C-code can be inserted directly into a DLL-project in Microsoft Visual Studio and be built there.

The DLL-file is designed such that the input is a vector containing all the relevant parameters of the crane model. The output is a vector containing the elements of the mass-inertia and centripetal and Coriolis matrices. Due to symmetry properties, the output vector can be reduced significantly and only the relevant elements are returned. The matrices are reassembled inside the IC-field and the constitutive relations are calculated as described in Section 2.2.7. It should be noted that a slight modification is applied to the effort expression in Equation 2.75 as the terms containing forces and moments are removed, i.e. $\boldsymbol{\tau}$ and $\mathbf{g}(\mathbf{q})$. This is done in accordance with the definition of the kinematics. Furthermore, since it is convenient to have separate 1-junctions representing the generalized coordinates and their velocities, the IC-field is connected to a number of 1-junction corresponding to the number of generalized coordinates in the system. The IC-field representing the crane is illustrated in Figure 3.5 and the code executed inside the IC-field is referred to in Appendix B.

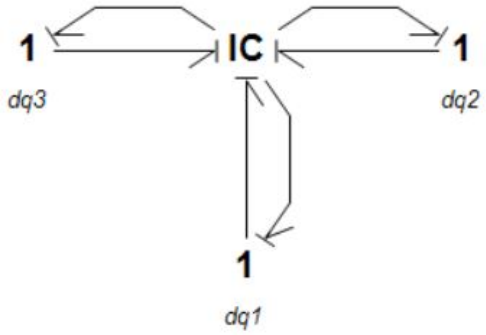

Figure 3.5: IC-field interfaced with the generalized coordinates

To reduce the complexity of the model, the calculation of the generalized coordinates is done in a subsystem called *Calculation of angles*, which is illustrated in Figure 3.6a. The generalized coordinates are calculated by integrating the flow signal given by the three 1-junctions connected to the IC-field and then distributed as signals to the Jacobian matrices and other subsystems that are dependent on them.

3.7 Kinetics

In addition to the kinematics, the forces that act on the crane must be included. These forces are related to gravity, payloads, winches, wires, and actuators and will be interfaced with the IC-field as generalized forces. The relationship between the kinematics and kinetics is described with MTF-elements that connect the generalized coordinates to the generalized forces that act on arbitrary points p on the crane. By recalling the properties of the Jacobian matrices, the constitutive relations in the MTF-elements are defined as follows

$$\begin{aligned} \mathbf{f}_p &= \mathbf{J}_p \mathbf{f}_q \\ \mathbf{e}_q &= \mathbf{J}_p^T \mathbf{e}_p \end{aligned} \tag{3.14}$$

Here $\mathbf{e}_p$ and $\mathbf{f}_p$ are the flow and effort at the arbitrary point p, while $\mathbf{e}_q$ and $\mathbf{f}_q$ represent the flow and effort of the generalized coordinates. The modulus that relates the flows and efforts is given by the Jacobian matrix $\mathbf{J}_p$. Note that when only forces are acting on the arbitrary point p, the last three rows in the Jacobian matrix can be omitted. On the other hand, when moments are the sole contributor to the arbitrary point p, the first three rows can be neglected.

3.7.1 Gravitational loads

As previously stated, the crane consists of five body parts that have masses of significance in relation to their gravitational loads. The Jacobian matrices that relate the velocities at the centers of gravity of these bodies were developed in Section 3.4 and are implemented into MTF-elements as stated by the constitutive relation given in Equation 3.14. An overview of the connection between the IC-field and the gravitational forces is given in Figure 3.6. The Se-elements apply the gravitational force at the center of gravity of the jth body of the crane as $\mathbf{F}_{cg_j} = [0,\ 0,\ -m_j g]$ in the inertial reference frame.

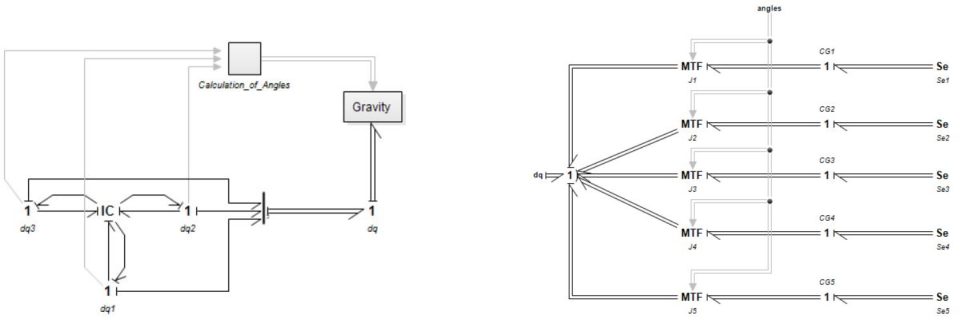

(a) IC-field and gravity interfacing

(b) Transformation of gravitational loads

Figure 3.6: Interfacing gravitational loads to the IC-field

3.7.2 Actuators

The crane is actuated by three actuators, allowing it to adjust the position of the two crane booms and rotate the crane base. The design of the actuators themselves is thoroughly described in Gyberg (2017) and only the interfacing of the actuator forces will be studied further due to its relevance when developing control algorithms later on.

The actuators that adjust the inclination of the crane booms generate an equal force in both their connection points to the crane. Hence, it is necessary to develop a relationship between the inertial

frame and the position of the upper connection points of the two crane boom actuators. Note that the positions of the lower connection points already have been defined in Section 3.3. By defining the reference frames 6 and 7 at the upper connection points of the lower and upper actuators, respectively, their position vectors are given as

$$\mathbf{r}^2_{6/2} = \begin{bmatrix} 0 \\ b \\ -u \end{bmatrix}, \quad \mathbf{r}^3_{7/3} = \begin{bmatrix} 0 \\ c \\ -s \end{bmatrix} \tag{3.15}$$

In the inertial reference frame, the position vectors are given by the following expressions

$$\mathbf{r}^0_{6/0} = \mathbf{r}^0_{2/0} + \mathbf{R}^0_2 \mathbf{r}^2_{6/2}, \quad \mathbf{r}^0_{7/0} = \mathbf{r}^0_{3/0} + \mathbf{R}^0_3 \mathbf{r}^3_{7/3} \tag{3.16}$$

The Jacobian matrices are derived as previously described and can be expressed as follows for the four connection points

$$\begin{aligned}
\mathbf{J}_6 &= \begin{bmatrix} \mathbf{e}^0_1 \times (\mathbf{r}^0_{4/0} - \mathbf{r}^0_{1/0}) & \mathbf{0}_{3x2} \\ \mathbf{e}^0_1 & \mathbf{0}_{3x2} \end{bmatrix} \\
\mathbf{J}_7 &= \begin{bmatrix} \mathbf{e}^0_1 \times (\mathbf{r}^0_{6/0} - \mathbf{r}^0_{1/0}) & \mathbf{e}^0_2 \times (\mathbf{r}^0_{6/0} - \mathbf{r}^0_{2/0}) & \mathbf{0}_{3x1} \\ \mathbf{e}^0_1 & \mathbf{e}^0_2 & \mathbf{0}_{3x1} \end{bmatrix} \\
\mathbf{J}_8 &= \begin{bmatrix} \mathbf{e}^0_1 \times (\mathbf{r}^0_{5/0} - \mathbf{r}^0_{1/0}) & \mathbf{e}^0_2 \times (\mathbf{r}^0_{5/0} - \mathbf{r}^0_{2/0}) & \mathbf{0}_{3x1} \\ \mathbf{e}^0_1 & \mathbf{e}^0_2 & \mathbf{0}_{3x1} \end{bmatrix} \\
\mathbf{J}_9 &= \begin{bmatrix} \mathbf{e}^0_1 \times (\mathbf{r}^0_{7/0} - \mathbf{r}^0_{1/0}) & \mathbf{e}^0_2 \times (\mathbf{r}^0_{7/0} - \mathbf{r}^0_{2/0}) & \mathbf{e}^0_3 \times (\mathbf{r}^0_{7/0} - \mathbf{r}^0_{3/0}) \\ \mathbf{e}^0_1 & \mathbf{e}^0_2 & \mathbf{e}^0_3 \end{bmatrix}
\end{aligned} \tag{3.17}$$

The interfacing with the IC-field is carried out through MTF-elements that use the Jacobian matrices as the moduli in the constitutive relations. Regarding the forces generated at the end-points of an actuator, they are of equal magnitude, but of opposite sign due to being reaction forces. They can thus be joined in a 0-junction with their power bonds going in the opposite direction of one another. The effort in the 0-junction is set by the force generated by the actuator model after being transformed into the inertial reference frame. The transformation of the local actuator forces is executed by first decomposing the forces in the lower and upper actuators with respect to $\delta_1(\theta_2)$ and $\delta_2(\theta_1, \theta_2)$, respectively. Then, the decomposed forces are rotated into the inertial frame by applying a rotation matrix with the angle θ_1 about the z-axis. With this, the crane boom actuator forces can be written as

$$\mathbf{F}^0_2 = F_{a2}\mathbf{R}^0_1 \begin{bmatrix} 0 \\ cos(\delta_1) \\ sin(\delta_1) \end{bmatrix}, \quad \mathbf{F}^0_3 = F_{a3}\mathbf{R}^0_1 \begin{bmatrix} 0 \\ cos(\delta_2) \\ sin(\delta_2) \end{bmatrix} \tag{3.18}$$

where F_{ai} is the amplitude of the local actuator force. The interfacing with the IC-field and actuator models is shown in Figure 3.7. Note that actuator 1 and actuator 2 refer to the lower and upper crane boom actuators, respectively.

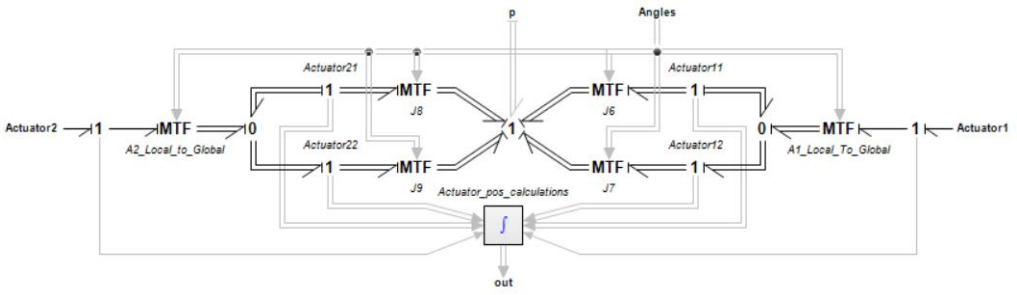

Figure 3.7: Crane boom actuator interfacing

When it comes to the actuator that is responsible for the rotation of the crane base, the interfacing to the IC-field is trivial since the rotation of the base is given by the generalized coordinate $q_1 = \theta_1$. This implies that the actuator model developed in Gyberg (2017) can be connected directly to the generalized velocity $\dot{q}_1$, which is provided by the IC-field. No further modifications are required for the interfacing between the rotation of the crane base and the IC-field. With the inclusion of the subsystems that represent the forces applied by the actuators, the crane simulation model becomes as shown in Figure 3.8

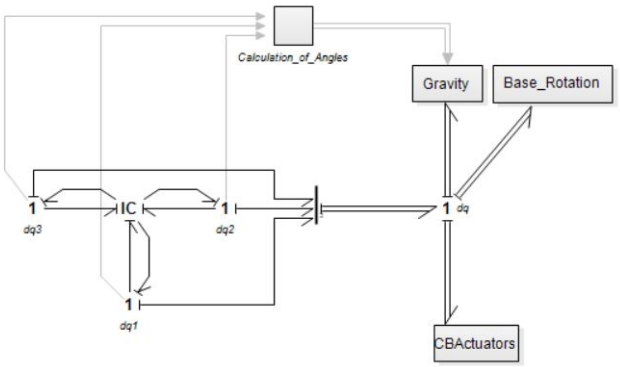

Figure 3.8: Actuator interfacing with IC-field

3.7.3 Main wire implementation and modeling

As explained in Gyberg (2017), the force applied by the main wire onto the crane can be defined as a generalized force acting on the crane boom tip. By placing reference frame 8 at the crane boom tip the position vector can be related to the inertial frame as follows

$$\mathbf{r}^0_{8/0} = \mathbf{r}^0_{3/0} + \mathbf{R}^0_3 \mathbf{r}^3_{8/3} \tag{3.19}$$

where

$$\mathbf{r}^3_{8/3} = \begin{bmatrix} 0 \\ L_2 \\ 0 \end{bmatrix} \tag{3.20}$$

The Jacobian matrix can then be defined as

$$\mathbf{J}_{10} = \begin{bmatrix} \mathbf{e}_1^0 \times (\mathbf{r}_{8/0}^0 - \mathbf{r}_{1/0}^0) & \mathbf{e}_2^0 \times (\mathbf{r}_{8/0}^0 - \mathbf{r}_{2/0}^0) & \mathbf{e}_3^0 \times (\mathbf{r}_{8/0}^0 - \mathbf{r}_{3/0}^0) \\ \mathbf{e}_1^0 & \mathbf{e}_2^0 & \mathbf{e}_3^0 \end{bmatrix} \tag{3.21}$$

With this, a wire model based on the theory developed in Skjong and Pedersen (2014), which was presented in Section 2.4, can be attached to the crane tip by using an MTF-element with the Jacobian matrix as the modulus.

The wire model is as stated in Section 2.4.1, based on connecting a series of mass-spring-dampers to mimic the dynamics of a wire. By utilizing the theory presented in Skjong and Pedersen (2014), the wire model developed in Gyberg (2017) can be implemented after applying a set of modifications to the wire elements. A general wire element is modeled as shown in Figure 3.9. Here, the CR-element is a combination of an R-element and a C-element and contains the properties of the spring and damper in the wire model. The spring stiffness is reflected in the properties of the wire, namely the E-modulus, cross-sectional area and length of the wire element as shown in Equation 2.115. When it comes to the damping, the expression is given in Equation 2.118, where $\zeta = 5$ as suggested in Skjong and Pedersen (2014) to create an over-damped system. Note that the ζ-value can be tuned to remove high-frequent vibrations in the wire that would not be present in a real-world application. Furthermore, since a wire cannot absorb compression forces, a set of conditional statements are included to ensure that the tension in the wire never goes below zero. The I-element and Se-element account for the inertia and load that are present due to the mass located at the end of the wire element. The Sf-element sets the flow of the wire element by applying the wire velocity, which is given by the winch model that was developed in Gyberg (2017). Lastly, the MTF-elements denoted *XYZ0* and *XYZ1* apply the constitutive relation defined for the elongation of a wire element, which was given in Equation 2.120. The coordinates of the two end-points of the wire element are required in the constitutive relation, and they are calculated in the *Pos*-subsystem by the use of a vector parameterization between the two end-points of the wire. With the use of a vector parameterization, the number of wire elements can be increased by simply copying and pasting additional wire elements into the model and connecting them to the required input signals. Note that this method places the wire elements in a straight line and does not take into account the correct initial configuration of a wire subjected to gravity. To account for that, catenary equations could be implemented, but for simplicity, a small initialization phase is allowed at the start of the simulations to allow the wire to find its equilibrium position.

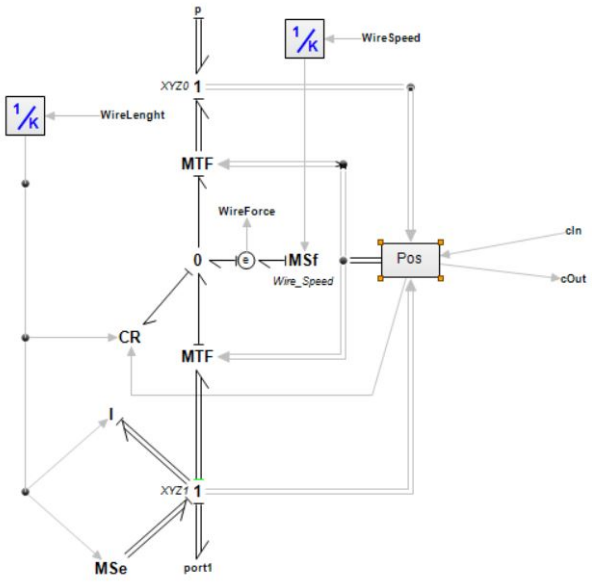

Figure 3.9: Wire element

The winch that controls the pay-in and out speed of the wire is implemented as described in Section 2.4.3, and the coupling between the winch and the wire elements is shown in Figure 3.10. A more thorough description of the process regarding the development of the winch model is found in Gyberg (2017).

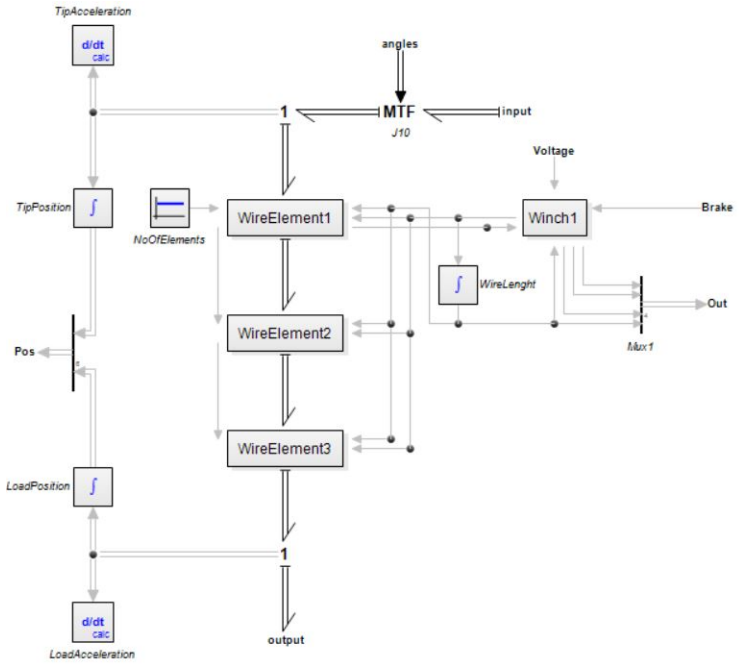

Figure 3.10: Wire elements and winch coupling

By implementing the wire and winch model into the crane system, as shown in Figure 3.11, the crane simulation model designed in Gyberg (2017) is complete with the exception of the control system. The implementation of a new control system is presented in the next chapter. Note that the controller is designed to support the functionality that is required in the upcoming case study.

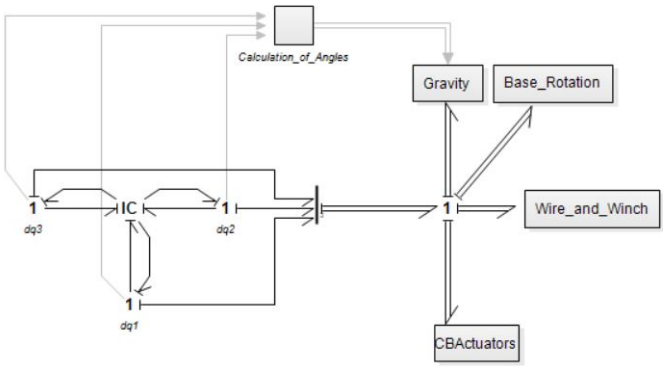

Figure 3.11: Wire and winch interfacing

4 | Case 1: Tugger winch systems

The purpose of this case study is to implement tugger winch systems that are capable of limiting pendulum motions and preventing the occurrence of snap loads. In order to create a realistic scenario, data from a simulation of an offshore operation was provided by Subsea 7. The setup is illustrated in Figure 4.1, where a $200t$ payload is suspended from four slings that are connected to the main wire through the crane block. Furthermore, fixed length tugger wires are connected to the payload to restrict the movement and to showcase the snap loads that occur during an offshore operation if no control of the tugger wires is performed.

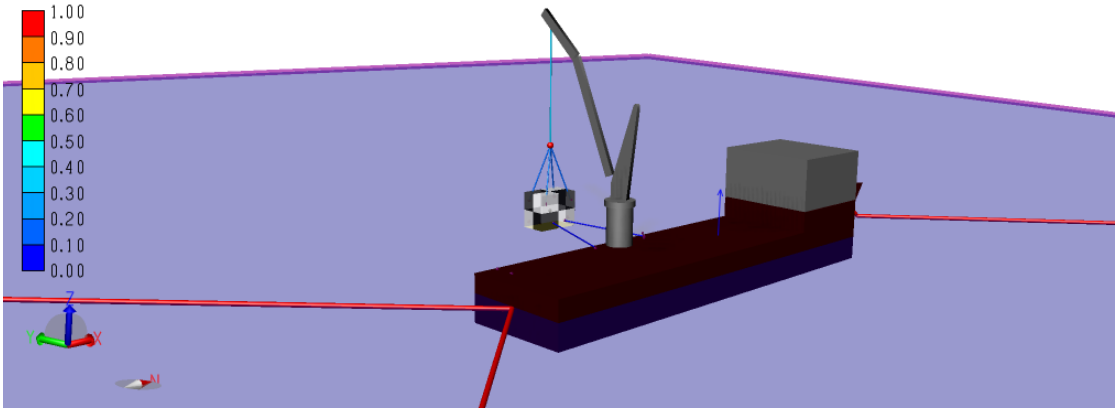

Figure 4.1: Case setup for the payload

4.1 Model setup and scaling

The simulation model provided by Subsea 7 is of a full-scale offshore operation. Hence, the parameters retrieved from the SIMA model must be scaled down to correspond with the scale of the model crane in the MCMR Lab. It is important to note that the SIMA model itself is not modified, but that the generated simulation data are scaled into their correct magnitudes in relation to the model scale. Furthermore, the results that are presented in the case study are always given in accordance with the model scale of the crane designed by Gyberg (2017). Consequently, scaling laws are applied to modify the relevant parameters and simulation data.

With the scaling laws for classical mechanical systems, it is given that $length \propto \lambda$ and $time \propto \lambda^{\frac{1}{2}}$ (Ghosh, 2011), where the characteristic dimension $\lambda = 25$ corresponds to the model scale of 1:25. Note that the proposed scaling of time is related to weight and inertia forces, and must be scaled differently with respect to forces given in other domains (Ghosh, 2011). Furthermore, angular displacements are dimensionless and are not scaled (Ghosh, 2011). From the previously stated

scaling laws, the following can be derived if the density, ρ, is assumed constant.

$$mass \propto \rho \cdot length^3 \propto \lambda^3 \tag{4.1}$$

With the proposed geometric scaling laws, the moment of inertia is scaled as follows

$$moment\ of\ inertia \propto mass \cdot length^2 \propto \lambda^5 \tag{4.2}$$

Additionally, the sea states are scaled, which implies that the significant wave height, H_s, and peak period, T_p, are scaled with respect to the scaling laws for length and time, respectively. Evidently, by applying the proposed scaling laws, the magnitudes are reduced while the frequency is increased. Furthermore, the scaling laws in dynamics can be determined by applying the laws of motion Ghosh (2011). Considering that the acceleration is the double derivative of the displacement with respect to time, the following can be shown for the inertia forces

$$inertia\ force \propto \frac{mass \cdot length}{time^2} \propto \lambda^3 \tag{4.3}$$

Hence, the important dimensions of the crane and payload setup are given as follows in Table 4.1. Note that the dynamic characteristics of elastic bodies are affected by scaling. This is of importance when designing the proper dimensions of the tugger wires that are applied in the simulation model. Therefore, the derivation of the spring stiffness in the model scale and its implications on the dynamics will be discussed in Section 4.3.7.

Table 4.1: Full scale and model scale parameters

Parameter	**Full scale**	**Model scale**	**Unit**
Sling 1-4, length	18.04	0.7216	m
Main wire, length	36.78	1.4712	m
Tugger wires, length	27.35	1.094	m
Payload, mass	200000.0	12.8	kg
Payload dimensions, LxWxH	10.0x7.56x6.53	0.4x0.3024x0.2612	m
Payload inertia, x-axis	7429000.0	0.7607	kgm^2
Payload inertia, y-axis	7962000.0	0.8153	kgm^2
Payload inertia, z-axis	2685000.0	0.2749	kgm^2
Tugger wire 1, initial force	14207.0	0.909	N
Tugger wire 2, initial force	15145.0	0.969	N
Significant wave height	H_s	$H_s \cdot \lambda^{-1}$	m
Peak period	T_p	$T_p \cdot \lambda^{-\frac{1}{2}}$	s

Furthermore, the setup of the crane and payload in 20-Sim must imitate the configuration given in the SIMA model. Firstly, the vessel in the SIMA model is trimmed to have an initial roll angle of approximately $-1.1°$. Consequently, tension is induced in the fixed-length tugger wires. Hence, the configuration must be replicated within the limitations of the model crane at the MCMR Lab. Therefore, the initial crane boom angles are selected such that they produce an angle of $-1.1°$ between the upper crane boom and the xy-plane. The tugger wires are then tightened to keep the main wire perpendicular to the upper crane boom. Furthermore, the initial position of the model crane is different to the SIMA model regarding their respective inertial reference frames. Hence, the motion of the crane in SIMA is shifted such that it corresponds to the initial position of the tip of the crane boom in 20-Sim. Another modification is related to the fact that the tugger winches are stationary in the MCMR Lab because the crane platform is fixed to the ground. Consequently, the position of the tugger winches is fixed globally in the SIMA model. This leads to reduced snap loads in the tugger wires compared to the more realistic case where the tugger winches are attached to the moving vessel. Regardless, the adjustment makes the experiments performed with the model

crane comparable to the simulation executed in SIMA. Hence, data regarding the performance of the tugger winch systems are obtainable.

4.2 Payload model

To recreate the simulation of the offshore operation that was provided by Subsea 7, a similar payload setup must be developed in the bond graph language. The modeling of wires was described in Section 2.4.1, and the four slings are included by connecting four wire elements to the end-point of the main wire. In the opposite end, the four slings are connected to the payload, which will be modeled as a 3D rigid body. A generic modeling approach for 3D rigid bodies was developed in Pedersen and Engja (2014) and is applicable for this model. First, Pedersen and Engja established a general expression for the kinetic energy of a rigid body

$$T = \frac{1}{2}\int\int\int \rho(\mathbf{v} + \boldsymbol{\omega} \times \mathbf{r})^T(\mathbf{v} + \boldsymbol{\omega} \times \mathbf{r})dV \tag{4.4}$$

from which they derived the equations of motion using the quasi-Lagrange equations

$$\begin{aligned} \frac{d}{dt}(\frac{\partial T}{\partial \mathbf{v}}) + \boldsymbol{\omega} \times \frac{\partial T}{\partial \mathbf{v}} &= \boldsymbol{\tau}_v \\ \frac{d}{dt}(\frac{\partial T}{\partial \boldsymbol{\omega}}) + \boldsymbol{\omega} \times \frac{\partial T}{\partial \boldsymbol{\omega}} + \mathbf{v} \times \frac{\partial T}{\partial \mathbf{v}} &= \boldsymbol{\tau}_\omega \end{aligned} \tag{4.5}$$

where ρ is the density, $\mathbf{v}$ is the linear velocity, $\boldsymbol{\omega}$ is the angular velocity, and $\boldsymbol{\tau}_v$ and $\boldsymbol{\tau}_\omega$ are the forces and moments, respectively. Note that the proposed approach neglects the contribution of the potential energy since it is added to the bond graph model at a later stage together with other external forces. By sorting the expressions generated by the quasi-Lagrange equations, the mass and Coriolis and centripetal matrices can be formed as shown below

$$\begin{aligned} \mathbf{M} &= \begin{bmatrix} m\mathbf{I}_{3x3} & -m\mathbf{S}(\mathbf{r}_G) \\ m\mathbf{S}(\mathbf{r}_G) & \mathbf{I}_g - m\mathbf{S}^2(\mathbf{r}_G) \end{bmatrix} \\ \mathbf{C} &= \begin{bmatrix} \mathbf{0}_{3x3} & -m\mathbf{S}(\mathbf{v}) - m\mathbf{S}(\boldsymbol{\omega} \cdot \mathbf{r}_G) \\ -m\mathbf{S}(\mathbf{v}) - m\mathbf{S}(\boldsymbol{\omega} \cdot \mathbf{r}_G) & m\mathbf{S}(\mathbf{S}(\mathbf{v}) \cdot \mathbf{r}_G) - \mathbf{S}((\mathbf{I}_g - m\mathbf{S}^2(\mathbf{r}_G)) \cdot \boldsymbol{\omega}) \end{bmatrix} \end{aligned} \tag{4.6}$$

where m is the mass, $\mathbf{r}_G$ is the position vector from the body-fixed frame to the center of gravity, $\mathbf{I}_g$ is the inertia tensor and $\mathbf{S}(\cdot)$ is the skew-symmetric matrix.

Recalling the constitutive relation defined for an IC-field in Equation 2.75, the mass and Coriolis and centripetal matrices can be incorporated into an IC-field to describe the kinetic energy of the rigid body. Furthermore, forces and moments are added to the system in both the body-fixed and inertial reference frame, as shown in Figure 4.2.

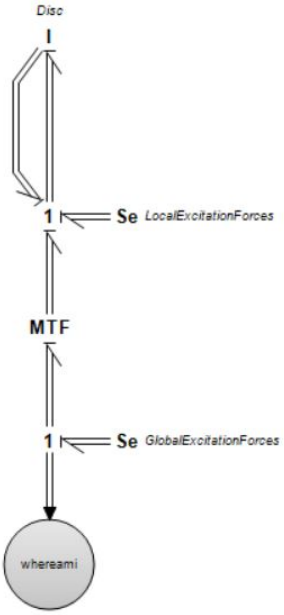

Figure 4.2: Generic rigid body

The MTF-element performs the transformation between the body-fixed and the inertial reference frame by applying the rotation matrix. Note that an angular velocity transformation of the body-fixed angular rates is carried out as the rotation matrix is dependent on the Euler angles. The angular velocity transformation matrix was derived in Section 2.3 and given in Equation 2.80.

The next step is to attach the slings to the payload. To develop the required constitutive relation, the position vectors that indicate the position of sling $i = 1, 2, 3, 4$ on the payload, given in the body-fixed frame, are expressed

$$\mathbf{r}^b_{s_i/0} = \mathbf{r}^b_{b/0} + \mathbf{r}^b_{s_i/b} \tag{4.7}$$

By the properties of a rigid body, the velocity becomes

$$\mathbf{v}^b_{s_i/0} = \mathbf{v}^b_{b/0} + \boldsymbol{\omega}^b_{b/0} \times \mathbf{v}^b_{s_i/b} \tag{4.8}$$

Then, by defining

$$\boldsymbol{\nu} = \begin{bmatrix} \mathbf{v}^b_{b/0} \\ \boldsymbol{\omega}^b_{b/0} \end{bmatrix} \tag{4.9}$$

the velocity expression can be rewritten to

$$\mathbf{v}^b_{s_i/0} = \begin{bmatrix} \mathbf{I}_{3x3} & \mathbf{i} \times \mathbf{r}^b_{s_i/b} & \mathbf{j} \times \mathbf{r}^b_{s_i/b} & \mathbf{k} \times \mathbf{r}^b_{s_i/b} \end{bmatrix} \cdot \boldsymbol{\nu} \tag{4.10}$$

where i, j, and k are unit vectors in the x-, y- and z-directions, respectively. By applying the rotation matrix between the body-fixed and inertial reference frame, the constitutive relation for

the four slings becomes

$$\begin{aligned}\mathbf{v}^0_{s_i/0} &= \mathbf{R}^0_b \begin{bmatrix}\mathbf{I}_{3x3} & \mathbf{i}\times\mathbf{r}^b_{s_i/b} & \mathbf{j}\times\mathbf{r}^b_{s_i/b} & \mathbf{k}\times\mathbf{r}^b_{s_i/b}\end{bmatrix}\cdot\boldsymbol{\nu} \\ &= \mathbf{R}^0_b \begin{bmatrix}1 & 0 & 0 & 0 & z_{s_i} & -y_{s_i} \\ 0 & 1 & 0 & -z_{s_i} & 0 & x_{s_i} \\ 0 & 0 & 1 & y_{s_i} & -x_{s_i} & 0\end{bmatrix}\cdot\boldsymbol{\nu}\end{aligned} \tag{4.11}$$

Note that solely the linear velocities are required as input to the wire models. The constitutive relation is included in the bond graph model by adding MTF-elements to the 1-junction that represents the body-fixed linear and angular velocities of the rigid body, which is shown in Figure 4.3.

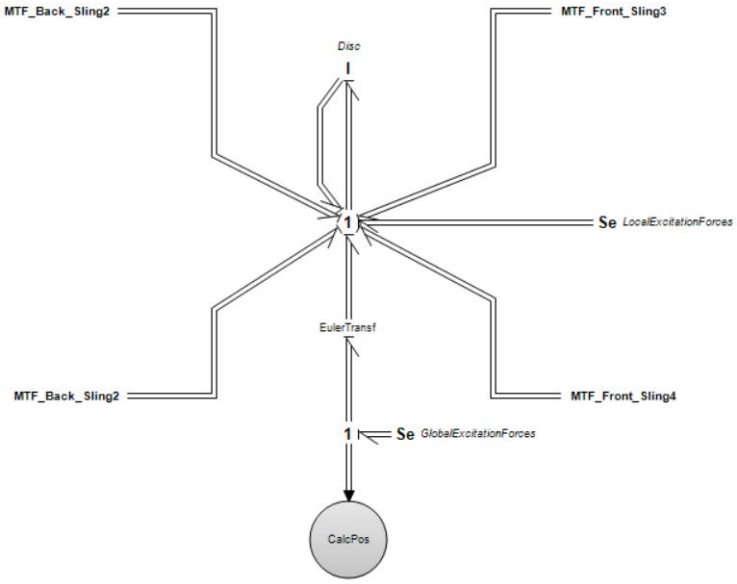

Figure 4.3: Rigid body with slings attached

The response of the payload model is evaluated by applying forces as impulses in the x- and y-directions. Note that the payload is connected to four slings, while the main wire is fixed at the opposite end. Figure 4.4b shows how the payload begins to oscillate symmetrically about its initial x-position when an impulse is applied in the x-direction. Furthermore, displacement is observed in the z-direction while the motion along the y-axis is zero. Considering a motion along the x- and z-axes, the induced pitch motion shown in Figure 4.4c is logical. The same is true when an impulse is applied in the y-direction, but in this case, the translational motion is about the y-axis and the rotation is about the x-axis, as shown in Figure 4.4e and Figure 4.4f, respectively. When applying the two impulses simultaneously, the payload is observed to oscillate as a combination of the two previous cases, but additionally rotates about the z-axis. This is shown in Figure 4.4h and Figure 4.4i. The response is expected considering that the moments of inertia are different about the x- and y-axes. Consequently, the payload is assumed to behave in accordance with a real system.

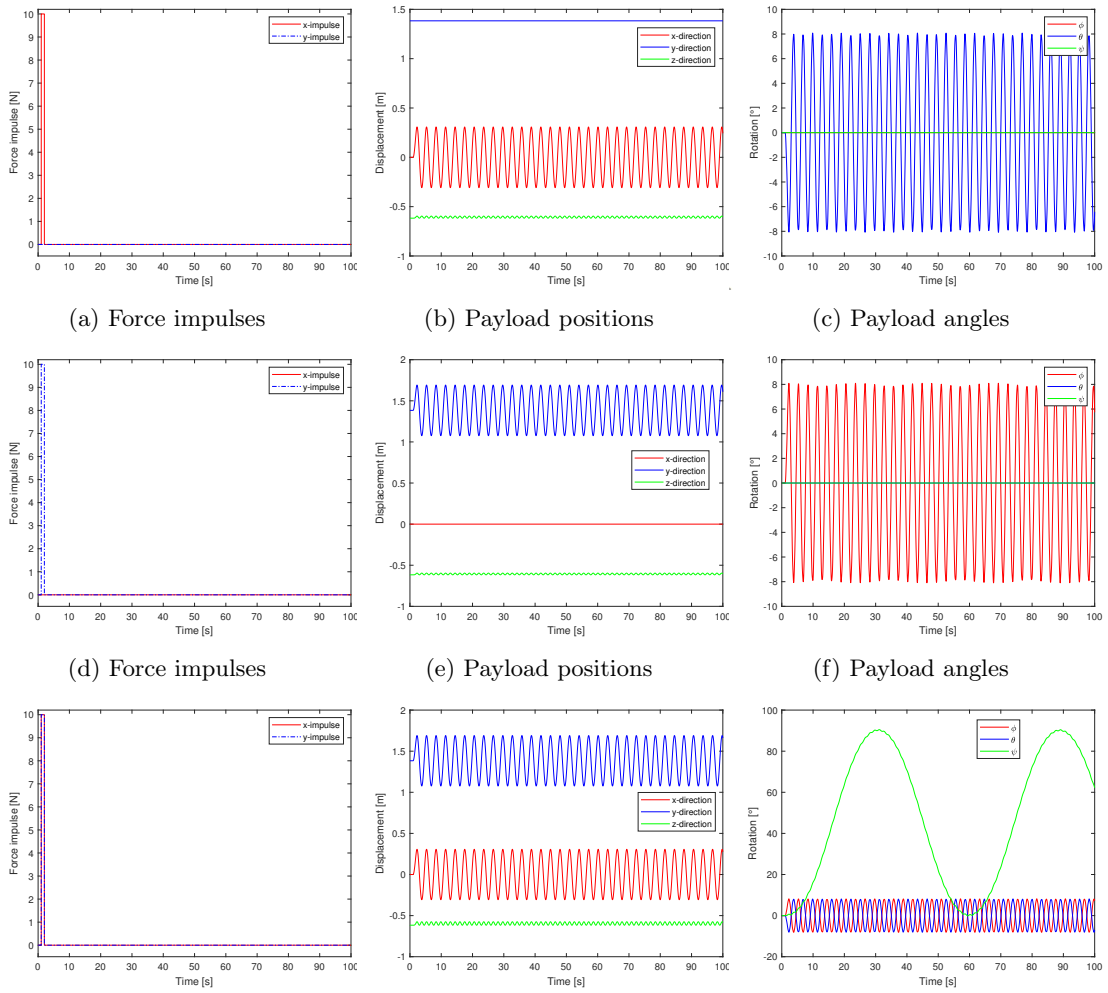

(a) Force impulses (b) Payload positions (c) Payload angles

(d) Force impulses (e) Payload positions (f) Payload angles

(g) Force impulses (h) Payload positions (i) Payload angles

Figure 4.4: Payload response induced by force impulses

4.3 Controller

In the SIMA model, the movement of the crane tip is induced by the vessel motion that is generated by the incident waves. As the model crane in the MCMR Lab is placed on a stationary platform, the actuators are controlled such that the crane tip is able to follow the desired reference trajectory. In this case, the reference trajectory corresponds to the position data that is obtained from the simulations executed in SIMA. Hence, an inverse dynamics controller can be designed such that the operational space error dynamics converges to zero with a time-varying reference, as derived in Section 2.5.3. To implement the controller, the position, velocity and acceleration references are required as inputs. Unfortunately, only the position of the crane tip is available from the simulation executed in SIMA. Hence, the velocity and acceleration must be approximated by a reference model.

4.3.1 Reference model

The reference model is designed as a mass-spring-damper system due to its similarities to the physical dynamics of a marine vessel (Fossen, 2011). To generate the desired trajectories the following transfer function is applied

$$h(s) = \frac{\omega_{n_i}^2}{s^2 + 2\zeta_i \omega_{n_i} s + \omega_{n_i}^2}, \; i = 1, 2, 3 \tag{4.12}$$

where ζ_i and ω_{n_i} are the relative damping ratios and natural frequencies, respectively. The block diagram is shown in Figure 4.5.

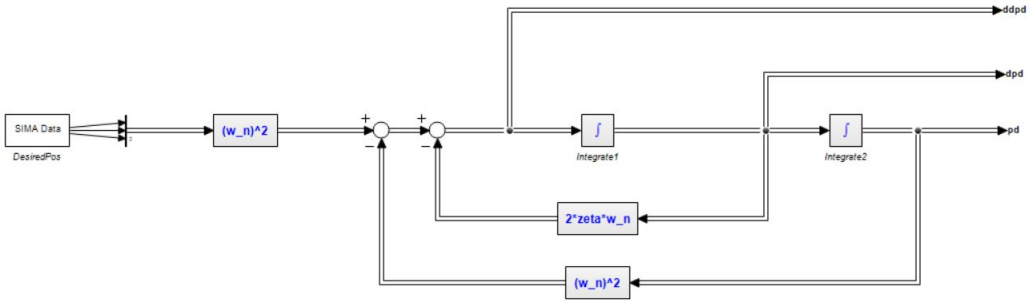

Figure 4.5: Reference model block diagram

For this case, the relative damping ratios and natural frequencies are tuned to have a position output that approximates the input. The reference is tested for a crane tip motion induced by a sea state with $Hs = 2.5m$ and $T_p = 10s$. Hence, the crane tip data retrieved from the SIMA model are scaled down with respect to the previously stated scaling laws. Consequently, the motion of the crane tip in the model scale corresponds to the motion induced by a sea state with $H_s = 0.1m$ and $T_p = 2.0s$. The results are shown in Figure 4.6 for the parameters $\boldsymbol{\zeta} = diag[\zeta_1,\ \zeta_2,\ \zeta_3] = diag[0.7,\ 0.7,\ 0.7]$ and $\boldsymbol{\omega}_n = diag[\omega_{n_1},\ \omega_{n_2},\ \omega_{n_3}] = diag[8,\ 8,\ 8]$.

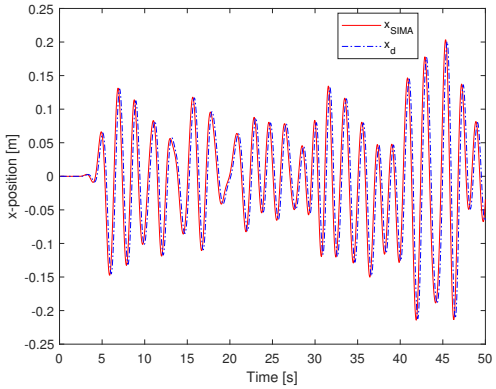

(a) X-position: SIMA and reference model

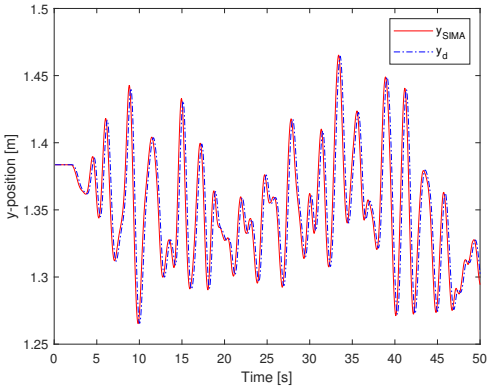

(b) Y-position: SIMA and reference model

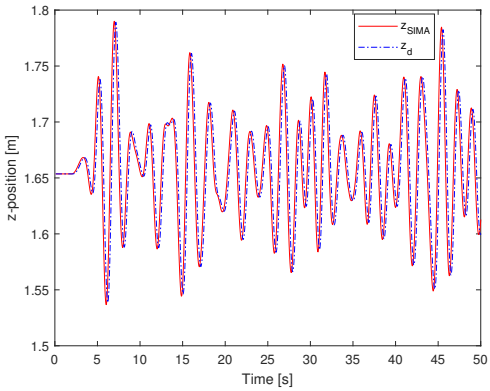

(c) Z-position: SIMA and reference model

Figure 4.6: Comparison of reference model and SIMA data

With the chosen parameters, the reference model produces a position output that barely deviates from the SIMA simulation data. The most prominent difference between them is the delayed response of the reference model. This is due to the filter properties of the reference model where a filter is known to produce a phase lag. Regardless, the critical factor is that the position data and the desired position have the same frequencies and amplitudes of the equal magnitude. This is to ensure that the data sent to the controller reflects the movement of a crane on a floating vessel. Hence, the damping ratios are set to values that indicate an under-damped system such that the amplitudes of the reference model output are increased to the magnitude of the input. By modifying the damping ratio to increase the amplitudes rather than increasing the frequency in an attempt to reduce the phase lag, the simulation time is decreased. The desired velocity and acceleration should give reasonable approximations of the values that are present in the SIMA model when considering that the desired position is found by double integration of the desired acceleration with respect to time.

4.3.2 Inverse dynamics controller

As mentioned, it is of interest to move the crane tip of the 20-Sim model similar to the position data retrieved from the simulation model made by Subsea 7. This can be achieved by developing an inverse dynamics controller that takes the desired position, velocity, and acceleration from the reference model as input and provides the necessary actuator forces as output. Note that slight modifications are applied to the theory derived in Section 2.5.3 to adapt the inverse dynamics controller to the crane simulation model.

External force transformation

As the controller output is the generalized force vector $\boldsymbol{\tau}$, it must be transformed to provide the forces that the actuators must generate. The procedure of deriving the generalized forces is shown in Section 2.1.3, and it is applied to develop the transformation matrix. To begin with, the local force of the crane base is equal to the inertial force, and no transformation is necessary. On the other hand, both rotation and decomposition of the forces are required for the two remaining actuators. By recalling the transformation described in Section 3.7.2, the actuator forces in the inertial frame are written as follows

$$\mathbf{F}_1^0 = F_{a1}\begin{bmatrix}1\\0\\0\end{bmatrix}, \quad \mathbf{F}_2^0 = F_{a2}\mathbf{R}_1^0\begin{bmatrix}0\\cos(\delta_1)\\sin(\delta_1)\end{bmatrix}, \quad \mathbf{F}_3^0 = F_{a3}\mathbf{R}_1^0\begin{bmatrix}0\\cos(\delta_2)\\sin(\delta_2)\end{bmatrix} \tag{4.13}$$

where F_{ai} are the amplitudes of the actuator forces in the local reference frames. By definition, the generalized forces are expressed as follows

$$\begin{aligned}
Q_1 &= F_{a1} + (\mathbf{F}_2^0)^T(\frac{\partial r_{a21}}{\partial\theta_1} - \frac{\partial r_{a22}}{\partial\theta_1}) + (\mathbf{F}_3^0)^T(\frac{\partial r_{a31}}{\partial\theta_1} - \frac{\partial r_{a32}}{\partial\theta_1})\\
Q_2 &= 0 + (\mathbf{F}_2^0)^T(\frac{\partial r_{a21}}{\partial\theta_2} - \frac{\partial r_{a22}}{\partial\theta_2}) + (\mathbf{F}_3^0)^T(\frac{\partial r_{a31}}{\partial\theta_2} - \frac{\partial r_{a32}}{\partial\theta_2})\\
Q_3 &= 0 + (\mathbf{F}_2^0)^T(\frac{\partial r_{a21}}{\partial\theta_3} - \frac{\partial r_{a22}}{\partial\theta_3}) + (\mathbf{F}_3^0)^T(\frac{\partial r_{a31}}{\partial\theta_3} - \frac{\partial r_{a32}}{\partial\theta_3})
\end{aligned} \tag{4.14}$$

The expression is rewritten and solved for the desired local actuator forces as given below. Note that $\boldsymbol{\tau} = [Q_1,\ Q_2,\ Q_3]^T$ is the output of the inverse dynamics controller.

$$\begin{aligned}
\boldsymbol{\tau} = \begin{bmatrix}Q_1\\Q_2\\Q_3\end{bmatrix} &= \underbrace{\begin{bmatrix}
1 & \frac{\partial(\mathbf{F}_2^0)^T}{\partial F_{a2}}(\frac{\partial r_{a21}}{\partial\theta_1} - \frac{\partial r_{a22}}{\partial\theta_1}) & \frac{\partial(\mathbf{F}_3^0)^T}{\partial F_{a3}}(\frac{\partial r_{a31}}{\partial\theta_1} - \frac{\partial r_{a32}}{\partial\theta_1})\\
0 & \frac{\partial(\mathbf{F}_2^0)^T}{\partial F_{a2}}(\frac{\partial r_{a21}}{\partial\theta_2} - \frac{\partial r_{a22}}{\partial\theta_2}) & \frac{\partial(\mathbf{F}_3^0)^T}{\partial F_{a3}}(\frac{\partial r_{a31}}{\partial\theta_2} - \frac{\partial r_{a32}}{\partial\theta_2})\\
0 & \frac{\partial(\mathbf{F}_2^0)^T}{\partial F_{a2}}(\frac{\partial r_{a21}}{\partial\theta_3} - \frac{\partial r_{a22}}{\partial\theta_3}) & \frac{\partial(\mathbf{F}_3^0)^T}{\partial F_{a3}}(\frac{\partial r_{a31}}{\partial\theta_3} - \frac{\partial r_{a32}}{\partial\theta_3})
\end{bmatrix}}_{\mathbf{Q}}\underbrace{\begin{bmatrix}F_{a1}\\F_{a2}\\F_{a3}\end{bmatrix}}_{\mathbf{u}}\\
\Rightarrow \mathbf{u} &= \begin{bmatrix}F_{a1}\\F_{a2}\\F_{a3}\end{bmatrix} = \mathbf{Q}^{-1}\boldsymbol{\tau}
\end{aligned} \tag{4.15}$$

4.3.3 Controller implementation

To implement the controller, the Q-matrix, h(q)-function and the derivative of the Jacobian matrix must be determined in addition to the expressions developed in Chapter 3. With the previously derived tools for expressing the Q-matrix, a DLL-file is generated. It is created through a process identical to the development of the kinematic crane model. By utilizing the Maple-script developed in Gyberg (2017), an algebraic expression of the Q-matrix is obtained and exported as C-code. A MATLAB-script is developed to process the C-code such that it can be built into a DLL-file in Visual Studio. The Q-matrix can then be evaluated at every time step in 20-Sim by calling the DLL-file and inserting the output into its proper matrix form.

The Jacobian matrix of the crane tip must be implemented into the control scheme when the objective of the controller is to regulate the motion of the crane tip. As for the Q-matrix, the expression of the Jacobian matrix is retrieved from the Maple-script. It is inverted by applying the definition of a pseudo-inverse matrix, which was derived in Section 2.1.5. The derivative of the Jacobian matrix is obtained by applying the chain rule, as explained in Section 2.1.5. The expression of the pseudo-inverse Jacobian matrix, the Jacobian matrix, and its derivative are inserted into their respective blocks of the control system that is illustrated in Figure 4.7. Regarding the h(q)-function, it represents the transformation between the generalized coordinates and the crane tip position given in the inertial frame. Subsequently, the position vector $r^0_{8/0}$, given in Equation 3.19, is applied and performs the proper transformation.

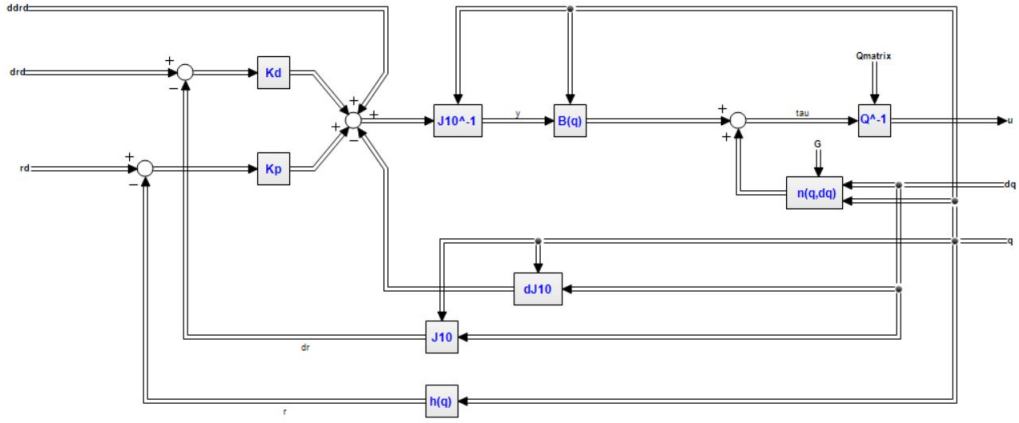

Figure 4.7: Inverse dynamics controller block diagram

4.3.4 Controller verification

The output of the controller is connected directly to the crane model to verify that the controller is properly implemented together with the external force transformation. In that regard, the motors and gears that drive the actuators are removed to avoid problems related to synchronization with the low-level controllers. The first step in testing the controller is to run a simulation where the main wire and payload are removed from the crane. This initial test is related to the state-space model that was developed for the crane simulation model in Chapter 3. Here, the equations of motion are derived for the crane while the payload is added as an external force. Consequently, the inverse dynamics employed in the controller do not account for main wire and payload dynamics. Therefore, the controller is first verified for a case without a payload. Then, the controller is modified to help account for the dynamics of the payload.

Crane without payload

By applying the simulation data that were used when verifying the reference model, the crane should move according to the generated reference trajectory. The ability of the crane to track the reference trajectory without significant errors in the position is shown in Figure 4.8. Here, the average position errors of $1 \cdot 10^{-4}$ indicate that the controller behaves properly. The gain matrices are set to $\mathbf{K}_p = diag[65,\ 15,\ 15]$ and $\mathbf{K}_d = diag[5,\ 1,\ 1]$.

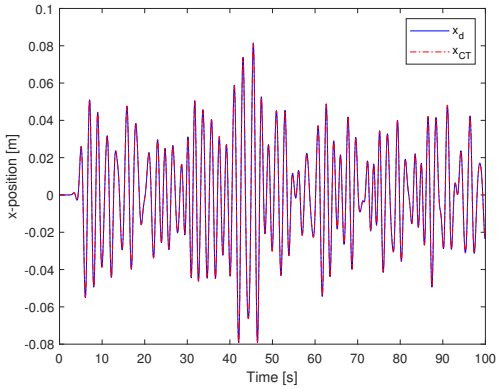

(a) X-position: Crane tip and reference model

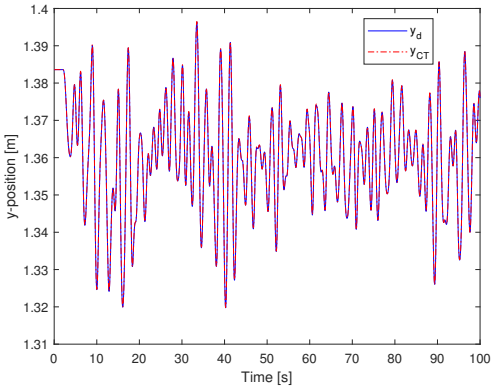

(b) Y-position: Crane tip and reference model

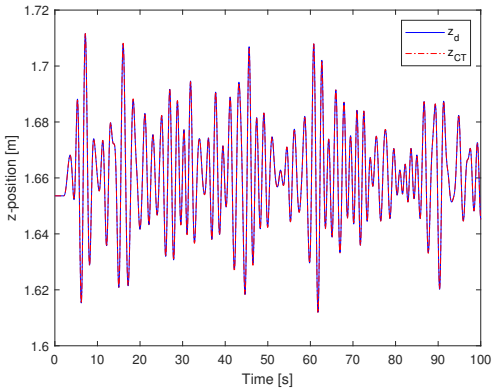

(c) Z-position: Crane tip and reference model

Figure 4.8: Reference and crane tip movement

The controller is then tested for a rougher sea state with $H_s = 0.26m$ and $T_p = 2.0$ to verify whether the controller is capable of moving the crane tip in accordance with extreme weather conditions. Again, the difference between the crane tip position and the reference signal is minuscule with a maximum average error of $7 \cdot 10^{-4}$ in the translational directions. Evidently, the controller functions properly and the control parameters can be tuned to increase the error convergence rate towards zero.

Crane with payload

As previously stated, the payload is not accounted for in the equations of motion that the controller currently is based on. Therefore, the controller is expected to perform poorly when the payload and wire dynamics are included in the simulation model. Note that a gravity term related to the mass of the payload must be included in the term $\mathbf{n}(\mathbf{q}, \dot{\mathbf{q}})$. From the definition of potential energy in Equation 2.13 and the matrix $\mathbf{g}(\mathbf{q})$ in Equation 2.58, the following expression is derived

$$\mathbf{g}_6(\mathbf{q}) = \frac{\partial V_6}{\partial \mathbf{q}} = \frac{\partial (m_6 \mathbf{g}^T \mathbf{r}^0_{8/0})}{\partial \mathbf{q}} \tag{4.16}$$

where m_6 is the mass of the payload and $\mathbf{r}^0_{8/0}$ is the position vector of the crane tip given in the inertial reference frame.

With the inclusion of the gravity term, the simulation data of the sea state with $H_s = 0.1m$ and $T_p = 2.0s$ are applied to the model. Substantial deviations from the desired positions are observed in Figure 4.9, and the issue regarding the state-space model is illustrated. Evidently, the forces calculated by the controller are not adequate for regulating the position of the crane tip when the payload is added to the crane.

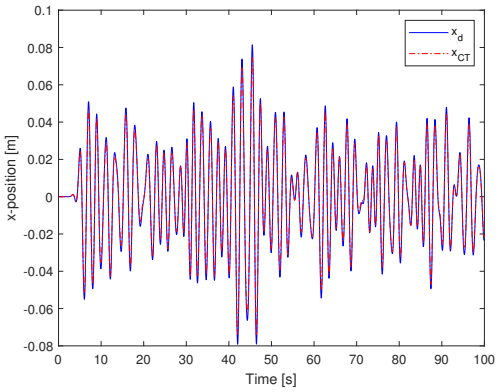

(a) X-position: Crane tip and reference model

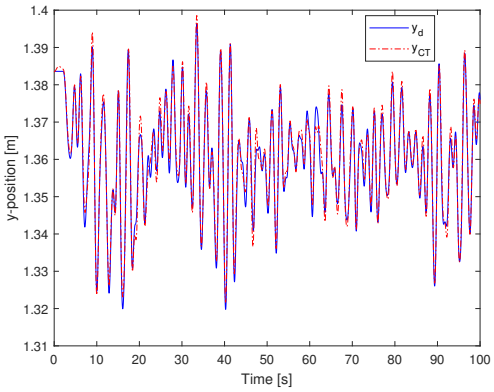

(b) Y-position: Crane tip and reference model

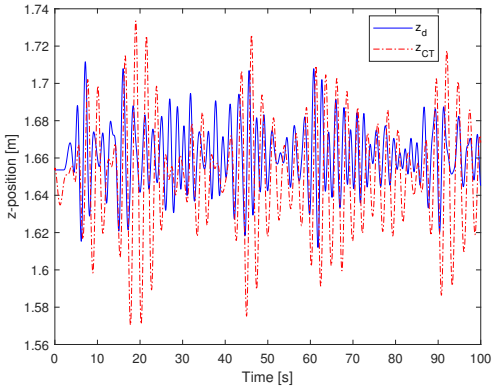

(c) Z-position: Crane tip and reference model

Figure 4.9: Reference and crane tip movement with payload attached

To improve the controller, a modification is applied to the state-space model utilized by the controller. To include a complete description of the dynamics of the main wire and payload, additional generalized coordinates must be defined, thus complicating the development of the crane model. Therefore, a simplified method is employed where the payload is assumed to be attached directly to the crane tip. Hence, the modification is performed by assuming that an additional rigid body is placed with its center of gravity at the crane tip. Consequently, an additional kinetic energy term must be included in the derivation of the $\mathbf{B}(\mathbf{q})$ and $\mathbf{C}(\mathbf{q}, \dot{\mathbf{q}})$ matrices that were presented in Chapter 3. In that regard, as the payload is assumed to act on the crane tip, the Jacobian matrix related to that point has already been developed. The remaining term is thus the inertia tensor, which can be expressed as follows

$$\mathbf{I}_6^0 = \mathbf{R}_8^0 \mathbf{I}_6^8 \mathbf{R}_0^8 \tag{4.17}$$

where $\mathbf{R}_8^0 = \mathbf{R}_3^0$ because the two reference frames are attached to the same rigid body. $\mathbf{I}_6^8$ refers to the inertia of the rigid body given in the reference frame defined at the crane tip. With this, the Maple-script utilized when developing the kinematic crane model in Section 3.6 is modified to include the contributions of the payload. A DLL-file is created to calculate the $\mathbf{B}(\mathbf{q})$ and $\mathbf{C}(\mathbf{q}, \dot{\mathbf{q}})$ matrices for the modified system that is utilized by the inverse dynamics controller.

By applying the described modifications to the system model, the controller performance is improved significantly. By setting the gain matrices to $\mathbf{K}_p = diag[800,\ 450,\ 550]$ and $\mathbf{K}_d = diag[10,\ 10,\ 10]$, the maximum average error is below $3 \cdot 10^{-4}$. Hence, the performance improves significantly with the combination of a modified state-space model and tuned gain matrices. Figure 4.10 shows the enhanced ability regarding moving the crane tip according to the reference signal.

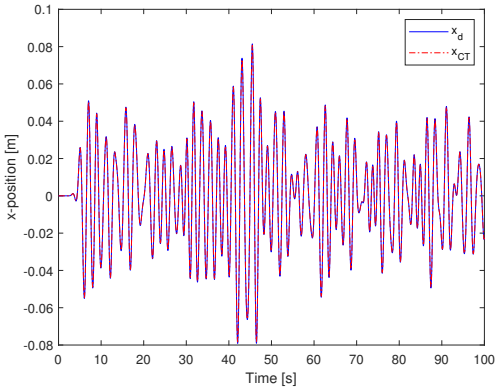

(a) X-position: Crane tip and reference model

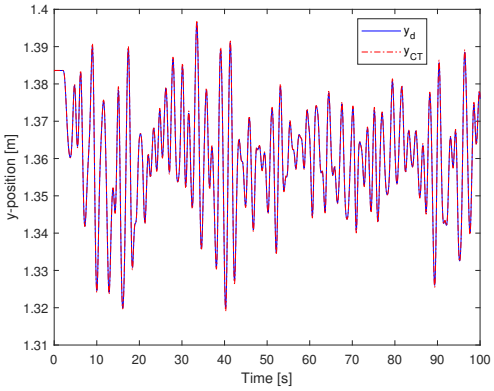

(b) Y-position: Crane tip and reference model

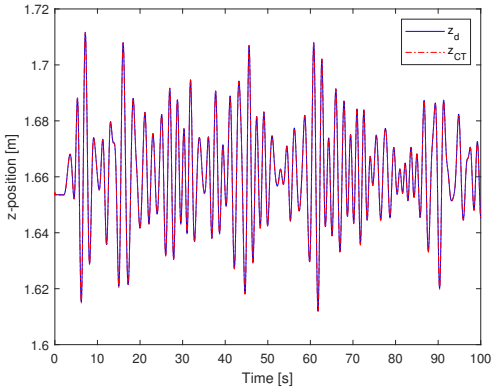

(c) Z-position: Crane tip and reference model

Figure 4.10: Reference and crane tip movement with modified state-space model

4.3.5 Actuator controllers

The dynamics of the actuator motors and gears were omitted to avoid interference during the implementation and verification of the inverse dynamics controller. At this point, they are reintroduced because they are an essential part of the functionality of the crane simulation model. Hence, they must be controlled such that the forces generated by the actuators correspond to the control output of the inverse dynamics controller. To achieve this, basic PID-controllers with force feedback from the actuators are designed. They calculate the voltage outputs that are applied to the electric motors that drive the actuators. The PID-controllers are taken from the 20-Sim controller library where the control output in the s-domain is given as follows

$$u = K \cdot e \cdot \left(1 + \frac{1}{1 + s \cdot T_i} + \frac{s \cdot T_d}{1 + s \cdot \frac{T_d}{N}}\right) \tag{4.18}$$

Here K, T_i, T_d, and N are the proportional gain, the integral time constant, the derivative time constant, and the derivative gain limit, respectively. The error e is given as the difference between the force set-point and the measured actuator force. In addition, anti-windup is implemented by

limiting the integral term between the upper and lower limits of the nominal voltages of the motors. The three PID-controllers are tuned to give a satisfactory response with respect to generating the required actuator forces. In Table 4.2, the controller gains are listed, and it should be noted that the two crane boom actuators utilize the same parameters because they are designed with identical gears and motors. Note that the simulation time increases with the inclusion of the controllers and that further tuning could lead to faster simulations.

Table 4.2: Actuator PID-parameters

PID-parameters	**Base rotation**	**Crane boom**
K	60	40
T_i	0.01	0.01
T_d	1.0	1.0
N	1.0	1.0

4.3.6 Tugger winch design

The next step is to implement the tugger winch systems to reduce the pendulum motion of the payload. As stated previously, tugger wires are susceptible to snap loads in the case where a wire engages a slack configuration. Therefore, it is of interest to design a winch system that is able to pay in and out wire such that the tension in the wire is kept above zero but below the safe working load (SWL). Consequently, the winch motors must be capable of supplying a sufficiently large rotational speed and moment onto the winch reel while the wire is under tension. As a starting point, the maximum pay-in speeds, hold-back forces, and pull-in forces for crane mounted tugger winches are retrieved from data provided by Subsea 7 and presented in Table 4.3.

Table 4.3: Crane mounted tugger winch properties

Pay-in speed [m/s]	**Hold-back force [kN]**	**Pull-in force [kN]**
0.75	98.1	37.3
0.85	86.3	33.4
1.0	73.6	28.4
1.2	61.8	24.5

Beginning with the tugger winch reel, it is designed based on the main wire reel, which was modeled in Gyberg (2017), and the standard components that are available in the MCMR Lab. As a result, Figure 4.11 presents a set of suggested parameters for the reel. Note that a structural analysis should be performed to verify the structural integrity of the reel.

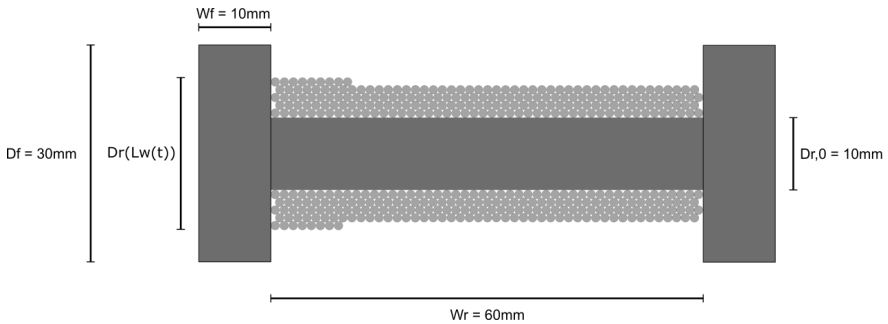

Figure 4.11: Tugger winch reel dimensions

With the suggested reel dimensions, the required pay-in speed of the tugger winch system is evaluated. By taking the maximum pay-in speed in Table 4.3 as a reference, the tugger winches should as a minimum be capable of obtaining those speeds. Furthermore, since it is of interest to evaluate the requirements of a tugger winch system subjected to different sea states, the maximum pay-in speed is set to $3m/s$ in the design phase. In relation to the model crane, the pay-in speed of the tugger winches becomes $v_{wire} = 0.60m/s$ in the model scale.

To begin with, the maximum rotational velocity that is required to obtain a pay-in speed of $0.60m/s$ is when the reel diameter is at its minimum. This corresponds to the case where all the wire has been paid out. Considering the reel dimensions in Figure 4.11, the maximum required rotational velocity becomes the following by applying Equation 2.131

$$\omega_{reel} = \frac{2 \cdot v_{wire}}{D_{rod}} = \frac{2 \cdot 0.60}{10 \cdot 10^{-3}} = 120 \ rad/s = 1145.9 \ RPM \tag{4.19}$$

In addition to fulfilling the criterion regarding pay-in speed, the tugger winch systems must be capable of generating enough force to operate in the tension set-point range. To that extent, the maximum required force in the design of the tugger winches is related to the pull-in forces given in Table 4.3, which indicate a maximum required force of $2.4N$ in the model scale. In contrast to the case with the pay-in speed, the maximum torque is required when the reel diameter is at its largest value. This implies that all the wire is rolled onto the reel. By considering a wire length $L_w = 5m$, the largest reel diameter becomes $D_{r_{max}} = 24mm$ by utilizing Equation 2.126. Consequently, the maximum torque is obtained by considering that the torque equals force times distance where the distance corresponds to the maximum reel radius. Hence, the expression becomes the following

$$\tau_{reel} = \frac{D_{reel_{max}}}{2} \cdot F_p = \frac{24 \cdot 10^{-3}}{2} \cdot 2.4 = 0.0288 \ Nm \tag{4.20}$$

where τ_{reel} and F_p are the maximum required torque and force on the reel, respectively.

An iteration process is employed to encounter a motor and gear combination that fulfills the proposed criteria. Note that a wide range of gear and motor combinations could satisfy the chosen criteria, but that the most reasonable option is chosen. The specifications regarding the chosen components are given in Table 4.4 and Table 4.5.

Table 4.4: Tugger winch motor properties

Parameter	**Value**	**Unit**
Motor model name	EC 20	-
Motor model number	351008	-
Nominal voltage	24 V	V
Nominal speed	5220 RPM	RPM
Nominal torque	7.74 mNm	mNm
Nominal current	0.329 A	A
Stall torque	19.9 mNm	mNm
Terminal resistance	28.6	Ω
Terminal inductance	3.09	mH
Torque constant	23.8	mNm/A
Speed constant	402	RPM/V
Rotor inertia	5.1	gcm^2

Table 4.5: Tugger winch gear properties

Parameter	**Value**	**Unit**
Gearbox model name	Planetary Gearhead GP 22 C	-
Gearbox model number	143972	-
Reduction	4.4:1	-
Nominal torque	500	mNm
Max intermittent torque	800	mNm
Max efficiency	73	%
Weight	60	g
Mass inertia	0.4	gcm^2

From the motor and gear properties, the nominal output speed is $1186RPM$ with a gear reduction of 4.4:1. Hence, it complies with the pay-in requirement. Similarly, the nominal torque provided by the gear fulfills the criterion regarding pull-in forces with its value of $0.034Nm$. It should be noted that the reel will be connected directly to the gear shaft, thus no further reduction is applied from the gear to the reel. This is a small modification with respect to the main wire winch system designed in Gyberg (2017). However, a mechanical efficiency factor $\eta = 0.9$ is added to account for possible losses in the reel and gear connection.

4.3.7 Tugger winch implementation

Similar to the slings, the tugger wires are attached to the payload with the use of MTF-elements containing the constitutive relation defined in Equation 4.11. The winch reel in the other end of the wire will be globally fixed in accordance with the stationary crane base in the MCMR Lab. Furthermore, the electric power unit and reel dynamics are implemented as described in Section 2.4 with the use of the motor and gear properties that were given in Table 4.4 and Table 4.5, respectively. A TF-element is included to apply the mechanical efficiency factor of the reel and gear connection.

As previously mentioned, the tugger wires are subjected to snap loads when they are not controlled. To obtain a response in 20-Sim that corresponds to the data retrieved from the SIMA model, the wires must be scaled correctly. Regarding the wire dynamics, the displacement, stiffness, and damping must be taken into consideration. Given the general expression of the force generated by a spring, the following is defined

$$F_s = kx \tag{4.21}$$

where k is the spring stiffness and x is the displacement from the equilibrium position. Considering the unit of the spring stiffness being force per length unit, it is scaled as follows (Groesen and Molenaar, 2007)

$$k \propto \frac{mass \cdot \frac{length}{time^2}}{length} \propto \lambda^2 \tag{4.22}$$

The displacement is a length and obviously proportional to λ. In total, the spring force becomes proportional to λ^3, which corresponds with the definition in Equation 4.3. By further inspection of the spring stiffness, the following definition is given

$$k = \frac{Ea}{L} \tag{4.23}$$

where E is Young's modulus, a is the cross-sectional area of the wire, and L is the length of the wire. Hence, when both the area and length of the wire are scaled with respect to the proposed

scaling laws, it becomes evident that Young's modulus must be scaled to satisfy the scaling laws of the spring stiffness defined in Equation 4.22. Consequently, the material utilized in the model scale must be less stiff than the material in the full-scale scenario. On that note, Young's modulus utilized in the model scale is found by retrieving the cross-sectional stiffness defined for the tugger wires in SIMA. With a cross-sectional stiffness of $Ea = 13803kN$ and a standard tugger winch diameter of $D = 20mm$, Young's modulus becomes the following in full-scale

$$E = \frac{Ea}{\pi(\frac{D}{2})^2} = 43.9GPa \tag{4.24}$$

Hence, Young's modulus in the model scale becomes

$$E_m = \frac{E}{\lambda} = 1.76GPa \tag{4.25}$$

In SIMA, the damping coefficient is set to five percent of the cross-sectional stiffness. Applying the same condition in the model scale gives the following damping coefficient.

$$c_m = 1.76 \cdot 10^9 \cdot \pi \frac{8 \cdot 10^{-4}}{2} \cdot 0.05 = 44.2 \tag{4.26}$$

The damping in the simulation model is adjusted through the damping ratio, and it is found to be approximately $\zeta = 12.4$ with Equation 2.118. Thus, it is given a value considerably larger than the one proposed in Skjong and Pedersen (2014). However, the recommendation in Skjong and Pedersen (2014) is not given by exact science but is rather provided as an estimate of a value that yields a response similar to real wire dynamics. Therefore, to imitate the wire dynamics implemented in SIMA, the derived value of the damping ratio is considered suitable. Lastly, the wire density is set to the density of steel because it is a common wire material.

A PID-controller with force feedback is implemented to control the tugger winches. It is designed to prevent the tension in the tugger wire from going to zero, but simultaneously allow the tension to increase towards an upper limit. The upper limit is defined as the maximum hold-back force of the tugger winch system. It is related to the maximum hold-back force given in Table 4.3, which becomes $6.28N$ in the model scale. In relation to the tugger wire tension set-point range, the error utilized by the PID-controllers is divided into two separate scenarios. The first case is when the tension in the wire decreases below the initial tension. Here, the error is simply the difference between the measured and initial wire tension. The second case is when the tension is above the initial tension, but below the maximum allowed tension. Since it is of interest to limit the pendulum motion of the payload, the winch system should not pay out wire until approaching the tension limit. Therefore, a sigmoid function is multiplied with the error that was utilized in the first case to restrict the winch from paying out excessive wire when the tension in the wire increases. The sigmoid function that is applied is the logistic function, which is given as follows

$$f(x) = \frac{1}{1 + e^{-k(x-\Delta)}} \tag{4.27}$$

where k affects the steepness of the function while Δ shifts it along the x-axis. Note that the parameters of the sigmoid function and the PID-gains are found through an iteration process to obtain the best response from the tugger winch system. The chosen parameters are given in Table 4.6 and Table 4.7, and a plot of the sigmoid function is given in Figure 4.12

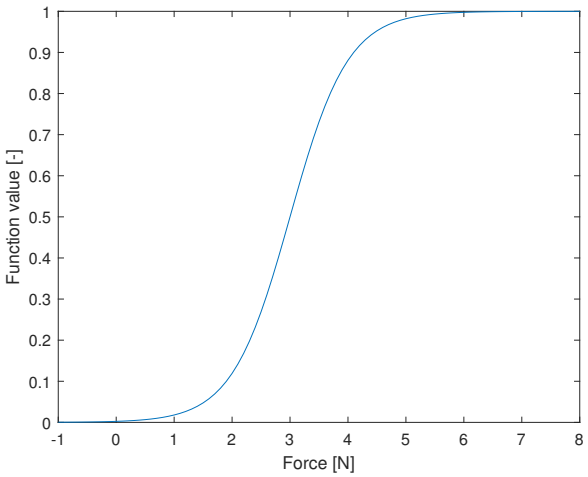

Figure 4.12: Sigmoid function with the chosen parameters

Table 4.6: Sigmoid parameters

Parameters	**Value**
k	5.5
Δ	5.0

Table 4.7: Tugger winch PID parameters

PID-parameters	**Value**
K	20.0
T_i	3.5
T_d	0.001
N	10.0

4.3.8 Tugger winch results

In all the simulations, a two seconds initialization phase is included to allow the tugger winches to pull in wire to generate the initial tension that is caused by the trimming of the vessel in the SIMA model. The initialization phase is implemented by modifying the crane tip position data to remain as constant x-, y- and z-values the first two seconds of the simulation. Furthermore, as previously stated, the results are presented with respect to the magnitudes that are present in a model scale environment. That implies that the data retrieved from the SIMA model are scaled according to the proposed scaling laws.

To verify the wire model, simulations are executed in both SIMA and 20-Sim with a moderately rough sea state with $H_s = 0.1m$ and $T_p = 2.0s$. Figure 4.13 shows that the snap loads are not identical and that the maximum magnitude is approximately 35% larger in 20-Sim compared to SIMA. The differences can be explained by a range of dissimilarities between the setups in the two simulation environments. First, the damping term in the 20-Sim model is turned off when the wire is slack to prevent the ability of engaging compression forces. Hence, it is possible that less damping is applied in this phase compared to how it is defined in SIMA. Consequently, snap loads of greater magnitudes could be expected. Moreover, the dissimilarity could in part be caused by the disparity between the two models regarding the fact that the 20-Sim model is designed to approximate a six degrees of freedom crane tip movement even though the crane itself is stationary.

Additionally, the initial tension and position of the payload do not fully correspond to the SIMA model as the 20-Sim crane model is not tilted $-1.1°$. Instead, the upper crane boom is adjusted to a $-1.1°$ angle with respect to the xy-plane and the tugger wires are tightened to produce the initial tension observed in the SIMA model. Consequently, the motion of the payload becomes different, which undoubtedly causes different loads in the tugger wires. Regardless, the tugger wires have a similar response and the results are deemed satisfactory with respect to the ability of the wire model to replicate the effect of snap loads. Considering that the snap loads have higher peaks in 20-Sim, the effectiveness of implementing an active tension controller in this model environment should prove valid with respect to the realistic scenario given in SIMA as well.

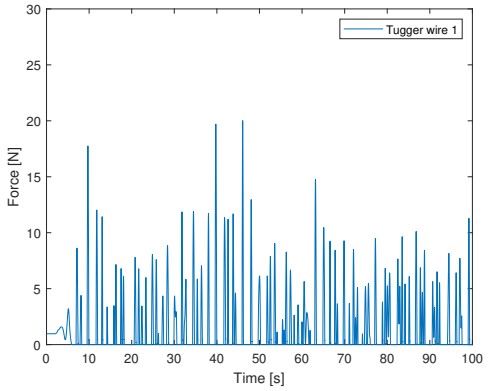

(a) SIMA: tugger wire 1

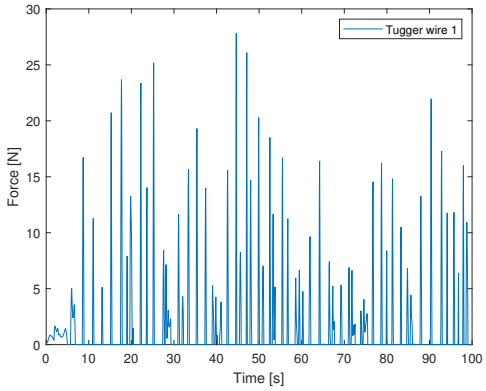

(b) 20-Sim: Tugger wire 1

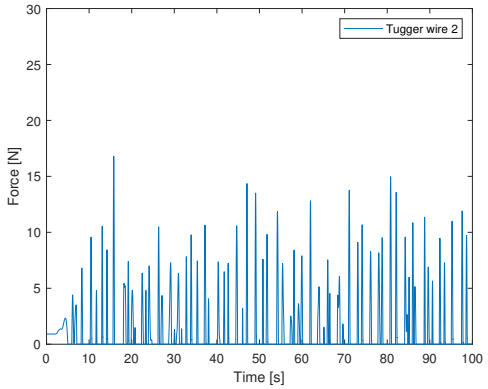

(c) SIMA: Tugger wire 2

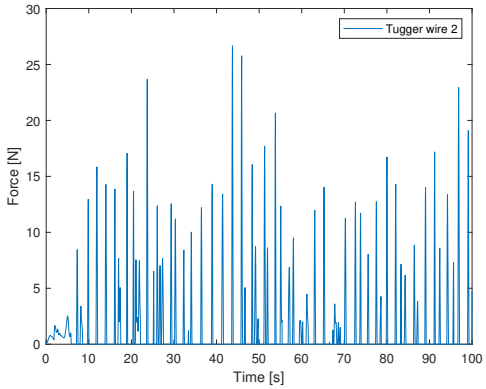

(d) 20-Sim: Tugger wire 2

Figure 4.13: Tugger wire snap loads, $\zeta = 12.4$, $H_s = 0.1m$ and $T_p = 2.0s$

To prevent snap loads from appearing, the active tension mode is activated in the tugger winch systems. The set-point range is given between the initial tension presented in Table 4.1 and the maximum hold-back force of the winch. To analyze the effect of the controller, the sea state that was applied for the previous case with fixed-length tugger wires is utilized. In Figure 4.14a, the ability to prevent snap loads is illustrated. The controller hinders the wires from entering a slack configuration by paying in the wire when the tension starts to decrease, as shown in Figure 4.14c and Figure 4.14b. Furthermore, the tension is kept within the allowed tension range by paying out wire when the tension starts to increase excessively. Note that the motor speed and gear moment are well within their limitations in the current sea state, as shown in Figure 4.14d and Figure 4.14e, respectively. Hence, the tugger winch system appears to function in regard to preventing snap loads from occurring.

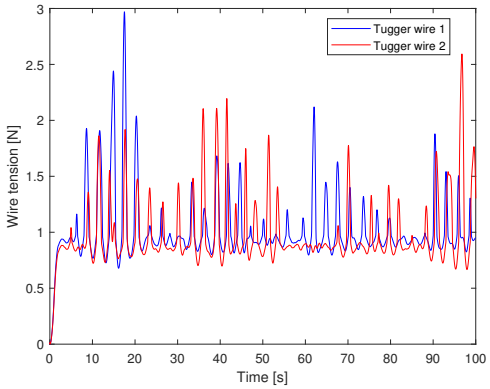

(a) Tugger wire tension

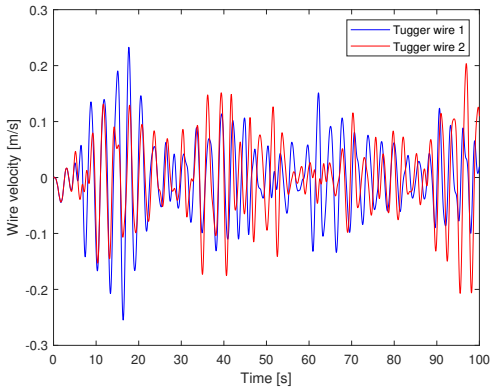

(b) Tugger wire velocities

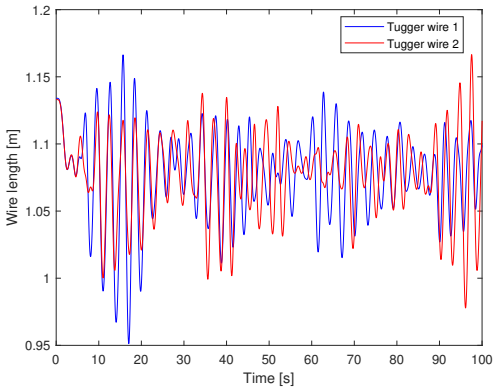

(c) Tugger wire lengths

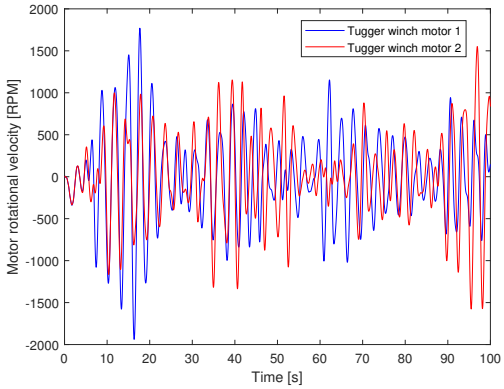

(d) Motor speed

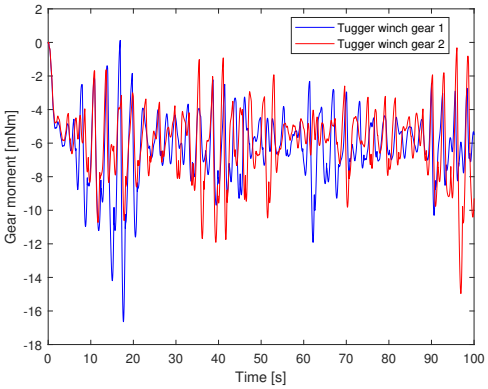

(e) Gear moment

Figure 4.14: Tugger winch system characteristics, $H_s = 0.1m$ and $T_p = 2.0s$

On the other hand, when observing the motion of the payload in Figure 4.15, the control algorithm is shown to be suboptimal with respect to limiting pendulum motion. Note that to simplify the comparison of the crane tip and payload motion, the payload data is shifted $0.03847m$ in the positive y-direction to accommodate for the initial displacement that is induced when the tugger wires are tightened the first two seconds of the simulation. The distance the payload data is shifted corresponds to the steady-state difference in the y-direction between the payload and crane tip when the crane is fixed in its initial configuration while the tugger wires are tightened to obtain their initial tension.With a standard PID-controller, substantial amplitudes in the pendulum motion are

observed in Figure 4.15b. Thus, the impact of implementing a sigmoid function becomes apparent in Figure 4.15a. Here, the amplitudes are significantly reduced since the winch is restrained from paying out an excessive amount of wire when the wire tension is within the tension range. Still, the controller performance is not deemed satisfactory with respect to the payload motion. By inspection of Figure 4.15a, the difference in the maximum peak values in the y-position are not the issue, but rather the fact that the payload moves with a phase lag relative to the crane tip. Hence, the maximum deviation between the crane tip and the payload is found to be $0.1096m$ in the model scale, implying that the maximum distance between the crane tip and payload in the y-direction would be $2.74m$ in a full-scale scenario. Depending on the criteria regarding allowed pendulum motion during a crane lift operation, the observed magnitudes could be deemed infeasible. However, the results are indubitably improved when compared to the case with no tugger wires, as shown in Figure 4.15c.

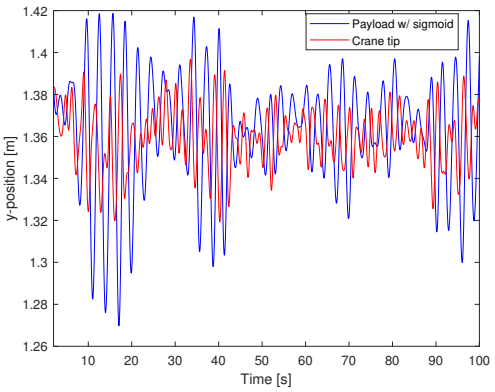

(a) Controller with sigmoid function

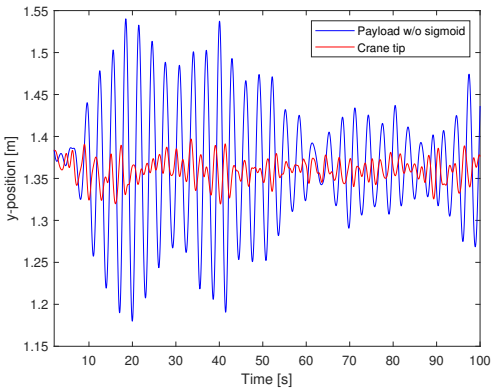

(b) Controller without sigmoid function

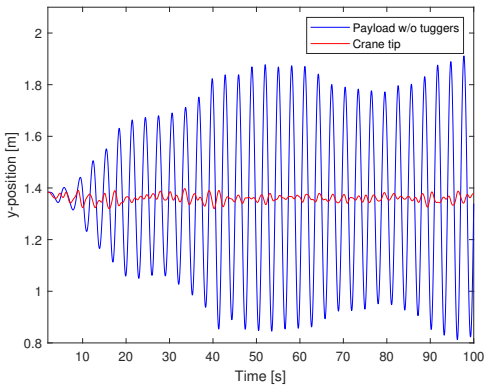

(c) Controller without tugger wires

Figure 4.15: Payload and crane tip motion comparison

Furthermore, Figure 4.16 shows how the payload is displaced more when the controller is active compared to the case with fixed-length tugger wires. This is expected to some extent since the fixed length tugger wires should hinder motion beyond their maximum lengths while the control system will pay out wire to hinder excessive tension. However, due to the lacking capabilities of the applied controller, the difference in motion amplitudes is larger than desired. Consequently, there is a trade-off between motion amplitudes and preventing snap loads when applying the proposed controller. Hence, other control techniques are required to both prevent snap loads and limit the pendulum motion to a greater extent than currently achieved.

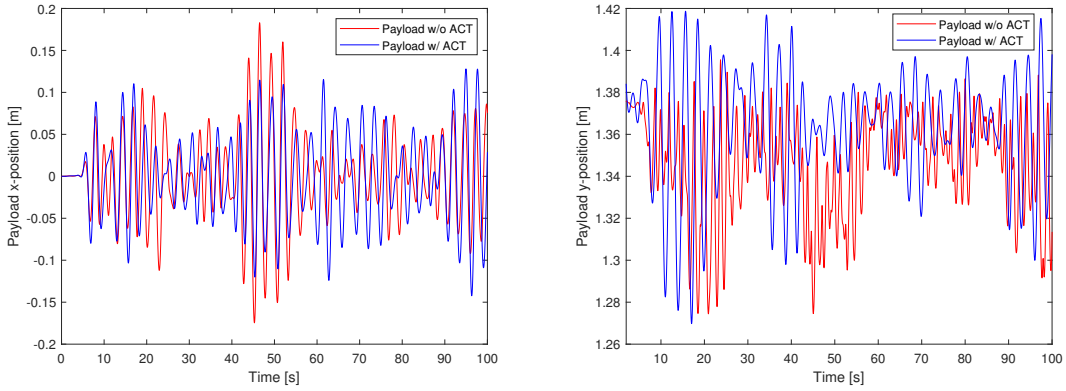

(a) Payload x-position

(b) Payload y-position

Figure 4.16: Payload motion with and without tension control

Another issue is related to the rotation of the payload about the z-axis. From Figure 4.17 it becomes apparent that the rotation of the payload is excited to significant magnitudes compared to the crane motion. This enlightens another issue of basic PID-algorithms controlling two individual tugger wires. They are not developed to perform a coordinated control of the payload with respect to its position, but rather individually ensure that the tension in the wire is kept within the tensions set-point range. Hence, the two tugger winch systems can promote unwanted motion during scenarios where they are fighting with one another to obtain the desired wire tension. However, compared to the case with fixed-length wires, the maximum amplitudes of the rotational motion of the payload about the z-axis is significantly reduced, as shown in Figure 4.17.

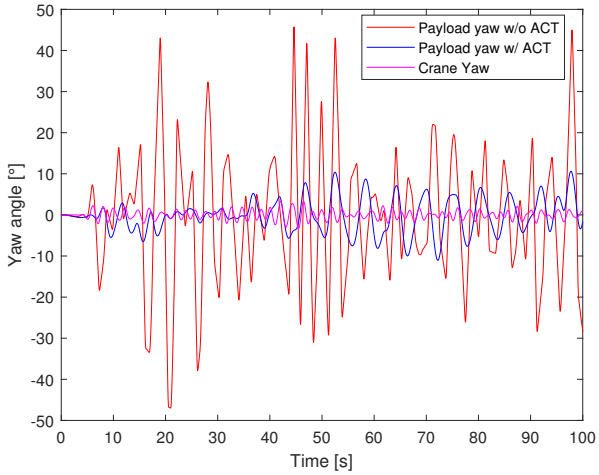

Figure 4.17: Payload and crane yaw motion

Furthermore, there are issues revolving the implementation of a sigmoid function with respect to the integral term. Since the error is kept close to zero until the wire tension approaches its SWL, the integral term is not reduced significantly if the wire tensions are at moderate levels. On the other hand, when the tension goes below the lower limit of the tension range, it immediately starts to increase. Hence, the integral term has a tendency to increase over time, which is shown in Figure 4.18. Consequently, the payload has a tendency to gradually be pulled towards the crane base. To limit this effect, the integral is capped to an upper limit corresponding to a value slightly higher than the one obtained after the initialization phase. Other methods such as integral reset were tested, but applying integral limits yielded the best results. To apply further improvements,

the current controller could be split into two separate controllers that are switched between with respect to the current state of the system. Hence, one controller is designed for the scenario when the wire starts to become slack, while the other controller regulates the wire tension when it is within the tension set-point range. Note that shattering is an issue that must be taken into account when performing switching between controllers.

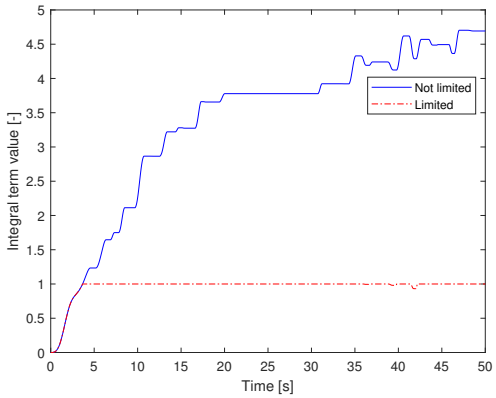

Figure 4.18: Integral terms with and without strict limits

Disregarding the problems related to the payload motion, the system is subjected to a rough sea state with $H_s = 0.22m$ and $T_p = 2.0s$. This is to test the limits of the tugger winch system with respect to its ability to prevent snap loads. Note that the simulations are given over a simulation period of $200s$ as the worst scenario of the motor output occurs at a later stage when applying the proposed sea state. From Figure 4.19a, it becomes apparent that the tugger wires do not go slack during the simulation, thus snap loads are prevented. Furthermore, the tension is kept within the maximum allowed value with respect to the proposed hold-back force. Hence, the tugger winch system is capable of preventing snap loads in rough sea states. By further inspection, Figure 4.19c, Figure 4.19e, and Figure 4.19f indicate that the system is about to reach its limits. The pay-in and out speeds approach their design limits of $0.6m/s$ when the motors have a rotational velocity of $5000RPM$, which is close to their maximum nominal velocities. At the same time, the moment provided by the gear when paying in wire approaches its limit of $34mNm$. Evidently, the applied sea state pushes the tugger winch system to its maximum capabilities when applying the proposed controller. Note that more intricate control algorithms could require less motor power, and thus enable operations in even rougher sea states. In Figure 4.19b, the crane tip and payload motion are observed to be out of phase, hence producing large relative distances. Consequently, the maximum distance between the crane tip and payload at any given time is found to be $0.2165m$ in model scale, which gives $5.41m$ in a full-scale scenario. In that regard, the limiting factor is the pendulum motion of the payload rather than snap loads, as was expected from the previous results. Note that rougher sea states were simulated but that large rotations about the z-axis rendered the results infeasible as the payload rotated 180° about its own axis.

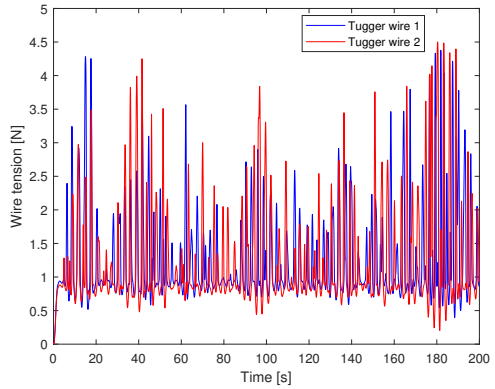

(a) Tugger wire tension

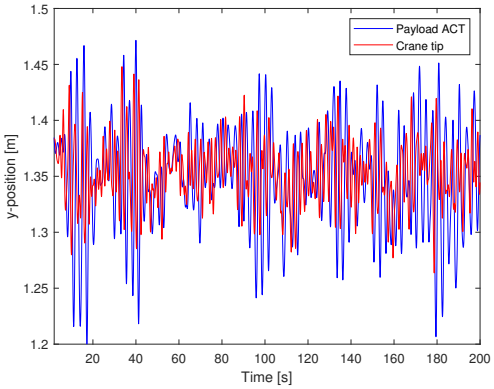

(b) Payload y-position

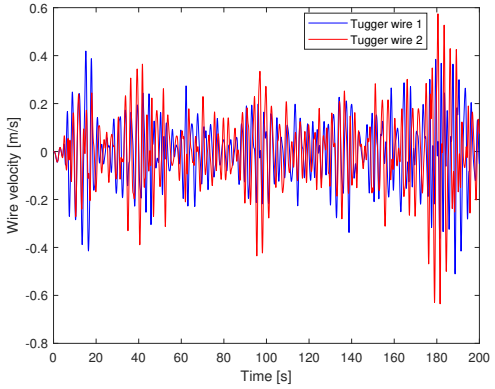

(c) Tugger wire velocities

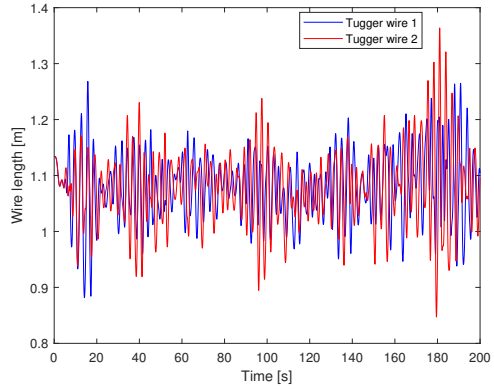

(d) Tugger wire lengths

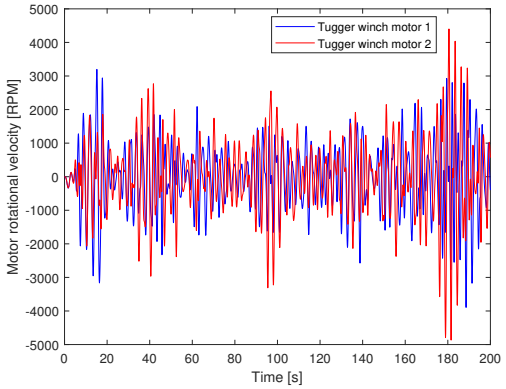

(e) Motor speed

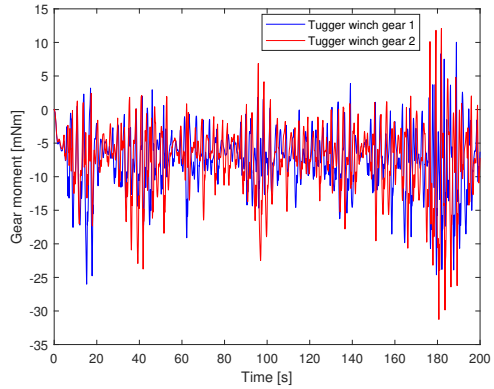

(f) Gear moment

Figure 4.19: Tugger winch system characteristics, $H_s = 0.22m$ and $T_p = 2.0s$

The implementation of control algorithms that consider both wire tension and payload position is recommended when the pendulum motion is the limiting factor of the system. On that note, a source of inspiration could be the model-based control system designed in Ren et al. (2018). Here, the applied wire tension is calculated by estimating the forces that are required to hold a payload at the desired position. It is designed for the three planer motions surge, sway and yaw and could be adapted to accommodate for the dynamic models that are applied in the crane simulation model. In this master's thesis, no further development of a control algorithm has been performed due to the discovery of a scaling error at a late stage of the conducted research. Hence, the whole chapter

had to be reworked and modified, which limited the time available for the implementation of more sophisticated controllers. However, the crane simulation model has been extended to include more accurate payload models and tugger winch systems. Consequently, the performance of other control systems can be evaluated by simply implementing the control algorithms directly into the existing simulation model.

5 | Case 2: Crane and vessel model

The model crane was designed to mimic the functionality of offshore cranes. Hence, the next step in the progression of the simulation model is related to the dynamics of a floating vessel. Consequently, a model with six degrees of freedom that is based on vessel dynamics will be added to the existing crane simulation model. Fortunately, by utilizing the derived framework of Lagrangian mechanics, a vessel model can be combined with the crane simulation model without applying considerable modifications. The process regarding the development of the interconnected vessel and crane dynamics will be presented in detail and is based on the theory described in Rokseth et al. (2017). To verify the model, the system response in a given sea state will be compared to the SIMA model provided by Subsea 7. Note that even though the model is based on the ship data in SIMA, a range of parameters are unavailable and must be approximated. Hence, the reader should be aware that the developed model is not expected to behave identically to the SIMA model. However, the comparison is carried out to verify that the vessel and crane response has the same tendencies as observed in other reliable simulation tools. As stated in Chapter 4, the results presented in this case study are given with respect to the scale of the model crane in the MCMR Lab. Furthermore, all relevant parameters related to the combined crane and vessel model are given in Appendix A.

5.1 Interconnected crane and vessel dynamics

The interconnected vessel and crane dynamics result in a system with six degrees of freedom related to the vessel and n degrees of freedom related to the crane. This gives a total of $k = 6 + n$ degrees of freedom. By recalling that the crane is modeled as an open chain of linked rigid bodies, the generalized coordinates are chosen as the joint displacements. Additionally, the generalized coordinates related to the vessel were defined in Equation 2.77. Hence, the vector of generalized coordinates that uniquely describes the position and orientation of the combined system becomes the following

$$\mathbf{q} = \begin{bmatrix} \mathbf{r}^0_{b/0} \\ \boldsymbol{\Theta} \\ \mathbf{q}_c \end{bmatrix} \tag{5.1}$$

where the vector $q_c = [q_{c_1}, ..., q_{c_n}]$ defines the generalized coordinates related to the crane joints. Since the quasi-coordinates are related to the generalized velocities through a transformation matrix, the quasi-coordinates vector becomes the following when augmenting Equation 2.82

$$\boldsymbol{\omega} = \begin{bmatrix} \mathbf{v}^0_{b/0} \\ \boldsymbol{\omega}^b_{b/0} \\ \dot{\mathbf{q}}_c \end{bmatrix} \tag{5.2}$$

By the definition of the relation between the quasi-coordinates and the generalized coordinates in Equation 2.82, the transformation matrix $\boldsymbol{\alpha}^T$ must be augmented with respect to the additional generalized coordinates related to the crane. Consequently, it becomes the following $n \times n$ matrix

$$\boldsymbol{\alpha}^T = \begin{bmatrix} \mathbf{R}_0^b & \mathbf{0}_{3x3} & \mathbf{0}_{3xn} \\ \mathbf{0}_{3x3} & \mathbf{T}_\Theta^{-1}(\boldsymbol{\Theta}) & \mathbf{0}_{3xn} \\ \mathbf{0}_{nx3} & \mathbf{0}_{nx3} & \mathbf{I}_{nxn} \end{bmatrix} \tag{5.3}$$

that yields the following inverse

$$\boldsymbol{\beta} = (\boldsymbol{\alpha}^T)^{-1} = \begin{bmatrix} \mathbf{R}_b^0 & \mathbf{0}_{3x3} & \mathbf{0}_{3xn} \\ \mathbf{0}_{3x3} & \mathbf{T}_\Theta(\boldsymbol{\Theta}) & \mathbf{0}_{3xn} \\ \mathbf{0}_{nx3} & \mathbf{0}_{nx3} & \mathbf{I}_{nxn} \end{bmatrix} \tag{5.4}$$

5.1.1 Position vectors and rotation matrices

The position vectors that were defined in the development of the crane simulation model in Chapter 3 must be modified to comply with the new system. In this case, the position vectors are related to the body-fixed reference frame on the vessel rather than the reference frame at the base of the crane. Therefore, the previously defined inertial frame is renamed as it no longer is inertial, and the new configuration is depicted in Figure 5.1 and Figure 5.2.

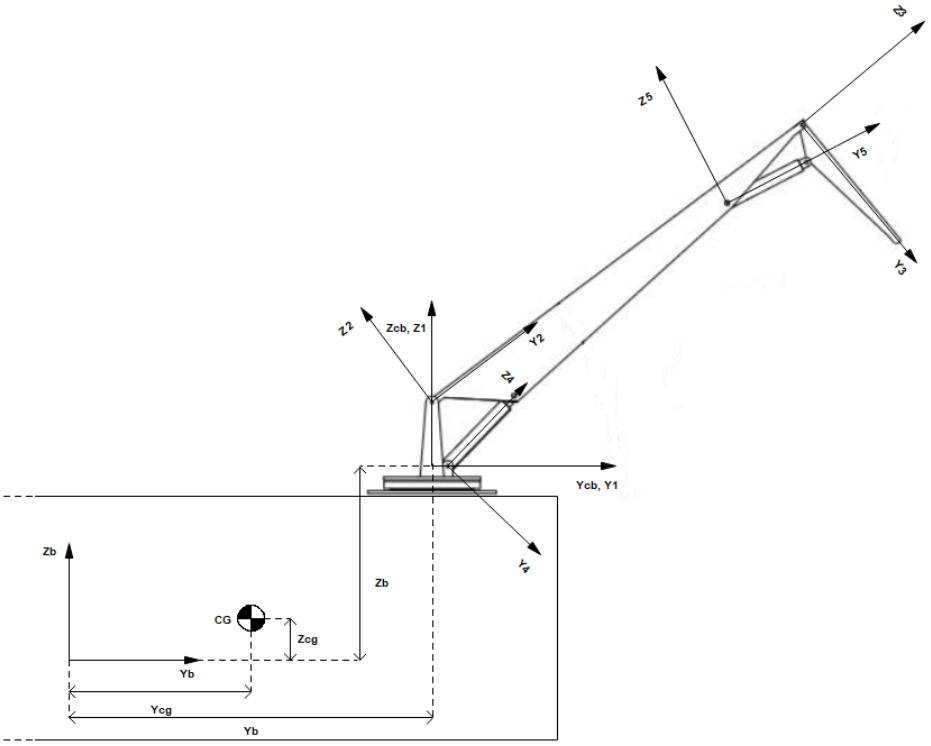

Figure 5.1: Crane and vessel in the YZ-plane

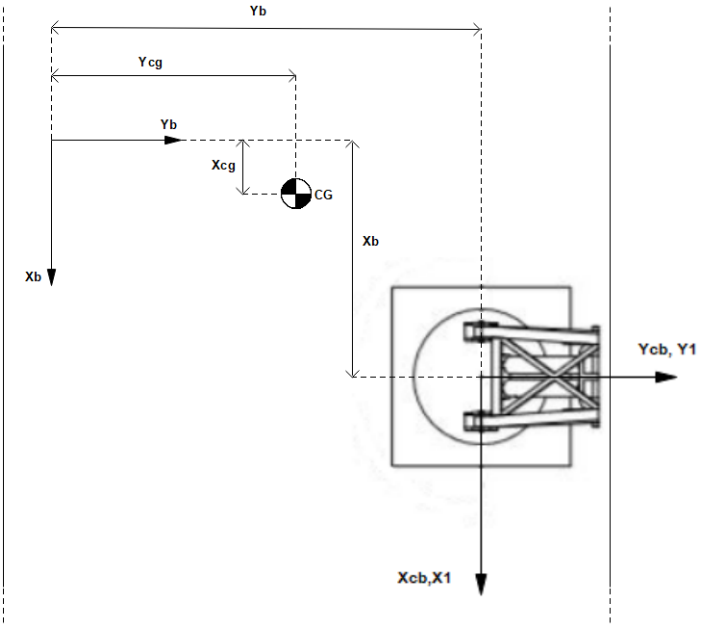

Figure 5.2: Crane and vessel in the XY-plane

To apply the modifications, both the position vector from the body-fixed vessel frame to the crane base and to the center of gravity of the vessel must be defined, and they are expressed as follows

$$\mathbf{r}^b_{cg_b/b} = \begin{bmatrix} x_{cg} \\ y_{cg} \\ z_{cg} \end{bmatrix}, \quad \mathbf{r}^b_{cb/b} = \begin{bmatrix} x_{cb} \\ y_{cb} \\ z_{cb} \end{bmatrix} \tag{5.5}$$

The position vectors that were defined with respect to the inertial reference frame that previously was located at the crane base, can be expressed in the body-fixed vessel frame as follows

$$\begin{aligned} \mathbf{r}^b_{2/b} &= \mathbf{r}^b_{cb/b} + \mathbf{r}^{cb}_{1/cb} + \mathbf{R}^b_1 \mathbf{r}^1_{2/1}, \quad & \mathbf{r}^b_{3/b} &= \mathbf{r}^b_{2/b} + \mathbf{R}^b_2 \mathbf{r}^2_{3/2}, \\ \mathbf{r}^b_{4/b} &= \mathbf{r}^b_{cb/b} + \mathbf{r}^{cb}_{1/cb} + \mathbf{R}^b_4 \mathbf{r}^1_{4/1}, \quad & \mathbf{r}^b_{5/b} &= \mathbf{r}^b_{2/b} + \mathbf{R}^b_2 \mathbf{r}^2_{5/2} \end{aligned} \tag{5.6}$$

$$\begin{aligned} \mathbf{r}^b_{cg_1/b} &= \mathbf{r}^{cb}_{1/cb} + \mathbf{R}^b_1 \mathbf{r}^1_{cg_1/1}, \quad & \mathbf{r}^b_{cg_2/b} &= \mathbf{r}^b_{2/b} + \mathbf{R}^b_2 \mathbf{r}^2_{cg_2/2}, \\ \mathbf{r}^b_{cg_3/b} &= \mathbf{r}^b_{3/b} + \mathbf{R}^b_3 \mathbf{r}^3_{cg_3/3}, \quad & \mathbf{r}^b_{cg_4/b} &= \mathbf{r}^b_{4/b} + \mathbf{R}^b_4 \mathbf{r}^4_{cg_4/4}, \\ \mathbf{r}^b_{cg_5/b} &= \mathbf{r}^b_{5/b} + \mathbf{R}^b_5 \mathbf{r}^5_{cg_5/5} \end{aligned} \tag{5.7}$$

Here the position vector $\mathbf{r}^{cb}_{1/cb}$ is zero as the origins of the two reference frames are defined at the same point. Note that the rotation matrices are identical to the ones derived in Chapter 3. This is because the reference frame at the crane base and the body-fixed vessel frame are attached to the same rigid body and do not rotate with respect to each other. Thus, the rotation matrices defined in Equation 3.6 give the following relation

$$\mathbf{R}^b_2 = \mathbf{R}^b_1 \mathbf{R}^1_2, \quad \mathbf{R}^b_3 = \mathbf{R}^b_2 \mathbf{R}^2_3, \quad \mathbf{R}^b_4 = \mathbf{R}^b_1 \mathbf{R}^1_4, \quad \mathbf{R}^b_5 = \mathbf{R}^b_1 \mathbf{R}^1_5 \tag{5.8}$$

Similarly, the unit vectors e^b_i are found to be the following

$$\mathbf{e}^b_1 = \mathbf{R}^b_1 \mathbf{e}^1_1 = \mathbf{R}^b_1 \mathbf{k}, \quad \mathbf{e}^b_2 = \mathbf{R}^b_2 \mathbf{e}^2_2 = \mathbf{R}^b_2 \mathbf{i}, \quad \mathbf{e}^b_3 = \mathbf{R}^b_3 \mathbf{e}^3_3 = \mathbf{R}^b_3 \mathbf{i} \tag{5.9}$$

5.1.2 Jacobian matrices

Then, the Jacobian matrices that relate the linear and angular velocities to the centers of gravity can be defined. To begin with, the contribution from the vessel onto the centers of gravity of the crane components must be considered. By definition, the linear velocity contribution from the vessel onto the center of gravity of the jth rigid body is expressed as follows

$$\begin{aligned}\mathbf{v}_{cg_j/0}^{(v_{b/0}^b)} + \mathbf{v}_{cg_j/0}^{(\omega_{b/0}^b)} &= \mathbf{v}_{b/0}^b + \boldsymbol{\omega} \times \mathbf{r}_{cg_j/b}^b \\ &= \mathbf{I}_{3x3}\mathbf{v}_{b/0}^b + \begin{bmatrix}\mathbf{i}_b \times \mathbf{r}_{cg_j/b}^b, & \mathbf{j}_b \times \mathbf{r}_{cg_j/b}^b, & \mathbf{k}_b \times \mathbf{r}_{cg_j/b}^b\end{bmatrix} \boldsymbol{\omega}_{b/0}^b \\ &= \mathbf{J}_{v_b}^{(v_{b/0}^b)}\mathbf{v}_{b/0}^b + \mathbf{J}_{\omega_b}^{(v_{b/0}^b)}\boldsymbol{\omega}_{b/0}^b\end{aligned} \tag{5.10}$$

Similarly, the contribution from the rotational velocity of the vessel can be expressed as follows

$$\begin{aligned}\boldsymbol{\omega}_{cg_j/0}^{(v_{b/0}^b)} + \boldsymbol{\omega}_{cg_j/0}^{(\omega_{b/0}^b)} &= \mathbf{0}_{3x3}\mathbf{v}_{b/0}^b + \mathbf{I}_{3x3}\boldsymbol{\omega}_{b/0}^b \\ &= \mathbf{J}_{v_b}^{(\omega_{b/0}^b)}\mathbf{v}_{b/0}^b + \mathbf{J}_{\omega_b}^{(\omega_{b/0}^b)}\boldsymbol{\omega}_{b/0}^b\end{aligned} \tag{5.11}$$

When it comes to the contributions from the generalized velocities $\dot{q}_{c_i}$ onto the center of gravity of the jth rigid body, the method developed in Section 2.1.5 is utilized. The following Jacobian matrices are obtained for the five crane components of relevant masses

$$\begin{aligned}
\mathbf{J}_1^b &= \begin{bmatrix}\mathbf{J}_{v_{cg_1}}^{(\dot{\mathbf{q}})} \\ \mathbf{J}_{\omega_1}^{(\dot{\mathbf{q}})}\end{bmatrix} = \begin{bmatrix}\mathbf{e}_1^b \times (\mathbf{r}_{cg_1/b}^b - \mathbf{r}_{1/b}^b) & \mathbf{0}_{3x2} \\ \mathbf{e}_1^b & \mathbf{0}_{3x2}\end{bmatrix} \\
\mathbf{J}_2^b &= \begin{bmatrix}\mathbf{J}_{v_{cg_2}}^{(\dot{\mathbf{q}})} \\ \mathbf{J}_{\omega_2}^{(\dot{\mathbf{q}})}\end{bmatrix} = \begin{bmatrix}\mathbf{e}_1^b \times (\mathbf{r}_{cg_2/b}^b - \mathbf{r}_{1/b}^b) & \mathbf{e}_2^b \times (\mathbf{r}_{cg_2/b}^b - \mathbf{r}_{2/b}^b) & \mathbf{0}_{3x1} \\ \mathbf{e}_1^b & \mathbf{e}_2^b & \mathbf{0}_{3x1}\end{bmatrix} \\
\mathbf{J}_3^b &= \begin{bmatrix}\mathbf{J}_{v_{cg_3}}^{(\dot{\mathbf{q}})} \\ \mathbf{J}_{\omega_3}^{(\dot{\mathbf{q}})}\end{bmatrix} = \begin{bmatrix}\mathbf{e}_1^b \times (\mathbf{r}_{cg_3/b}^b - \mathbf{r}_{1/b}^b) & \mathbf{e}_2^b \times (\mathbf{r}_{cg_3/b}^b - \mathbf{r}_{2/b}^b) & \mathbf{e}_3^b \times (\mathbf{r}_{cg_3/b}^b - \mathbf{r}_{3/b}^b) \\ \mathbf{e}_1^b & \mathbf{e}_2^b & \mathbf{e}_3^b\end{bmatrix} \\
\mathbf{J}_4^b &= \begin{bmatrix}\mathbf{J}_{v_{cg_4}}^{(\dot{\mathbf{q}})} \\ \mathbf{J}_{\omega_4}^{(\dot{\mathbf{q}})}\end{bmatrix} = \begin{bmatrix}\mathbf{e}_1^b \times (\mathbf{r}_{cg_4/b}^b - \mathbf{r}_{1/b}^b) & \mathbf{e}_2^b \times (\mathbf{r}_{cg_4/b}^b - \mathbf{r}_{2/b}^b) & \mathbf{0}_{3x1} \\ \mathbf{e}_1^b & \mathbf{e}_2^b & \mathbf{0}_{3x1}\end{bmatrix} \\
\mathbf{J}_5^b &= \begin{bmatrix}\mathbf{J}_{v_{cg_5}}^{(\dot{\mathbf{q}})} \\ \mathbf{J}_{\omega_5}^{(\dot{\mathbf{q}})}\end{bmatrix} = \begin{bmatrix}\mathbf{e}_1^b \times (\mathbf{r}_{cg_5/b}^b - \mathbf{r}_{1/b}^b) & \mathbf{e}_2^b \times (\mathbf{r}_{cg_5/b}^b - \mathbf{r}_{2/b}^b) & \mathbf{e}_3^b \times (\mathbf{r}_{cg_5/b}^b - \mathbf{r}_{3/b}^b) \\ \mathbf{e}_1^b & \mathbf{e}_2^b & \mathbf{e}_3^b\end{bmatrix}
\end{aligned} \tag{5.12}$$

The total linear and angular velocity of the center of gravity of the jth rigid body is the sum of the contributions from the vessel and the generalized velocities $\dot{q}_{c_i}$. Hence, the linear and angular velocities are obtained as a function of the generalized coordinates and the quasi-coordinates as follows

$$\begin{aligned}\mathbf{v}_{cg_j/0}^b &= \begin{bmatrix}\mathbf{J}_{v_b}^{(v_{b/0}^b)} & \mathbf{J}_{\omega_b}^{(v_{b/0}^b)} & \mathbf{J}_{v_{cg_j}}^{(\dot{\mathbf{q}})}\end{bmatrix} \boldsymbol{\omega} \\ &= \mathbf{J}_{v_{cg_j}}^b(\mathbf{q})\boldsymbol{\omega}\end{aligned} \tag{5.13}$$

$$\begin{aligned}\boldsymbol{\omega}^b_{j/0} &= \begin{bmatrix}\mathbf{J}_{v_b}^{(\omega^b_{b/0})} & \mathbf{J}_{\omega_b}^{(\omega^b_{b/0})} & \mathbf{J}_{\omega_j}^{(\dot{\mathbf{q}})}\end{bmatrix} \\ &= \mathbf{J}^b_{\omega_j}(\mathbf{q})\boldsymbol{\omega}\end{aligned} \tag{5.14}$$

The linear and angular velocities of the centers of gravity of the jth rigid body, given in the body-fixed vessel frame, are then obtained in a compact form as shown below

$$\boldsymbol{\nu}^b_{cg_j} = \begin{bmatrix}\mathbf{v}^b_{cg_j/0} \\ \boldsymbol{\omega}^b_{j/0}\end{bmatrix} = \begin{bmatrix}\mathbf{J}^b_{v_{cg_j}}(\mathbf{q}) \\ \mathbf{J}^b_{\omega_j}(\mathbf{q})\end{bmatrix}\boldsymbol{\omega} = \mathbf{J}^b_c(\mathbf{q})\boldsymbol{\omega} \tag{5.15}$$

5.1.3 Combined kinetic energy

To develop the equations of motion of the combined system, the kinetic energy of the crane must be derived. Consequently, the kinetic energy of each individual component of the crane must be expressed. This is done with the general expression of the kinetic energy of a rigid body, which was given in Equation 2.12. Therefore, the inertia tensors that are expressed in their local reference frames must be transformed into the body-fixed vessel frame by utilizing Equation 2.14. The inertia tensors are obtained as follows

$$\mathbf{I}^b_1 = \mathbf{R}^b_1\mathbf{I}^1_1\mathbf{R}^1_b, \quad \mathbf{I}^b_2 = \mathbf{R}^b_2\mathbf{I}^2_2\mathbf{R}^2_b, \quad \mathbf{I}^b_3 = \mathbf{R}^b_3\mathbf{I}^3_3\mathbf{R}^3_b, \quad \mathbf{I}^b_4 = \mathbf{R}^b_4\mathbf{I}^4_4\mathbf{R}^4_b, \quad \mathbf{I}^b_5 = \mathbf{R}^b_5\mathbf{I}^5_5\mathbf{R}^5_b \tag{5.16}$$

Then, the sum of the kinetic energy contributions from the crane components is given as follows by applying Equation 2.54

$$\sum_{j=1}^{n}(T_j(\mathbf{q},\boldsymbol{\omega})) = \frac{1}{2}\boldsymbol{\omega}^T\sum_{j=1}^{n}(\mathbf{B}_j(\mathbf{q}))\boldsymbol{\omega} \tag{5.17}$$

On a side note, if the expression of the kinetic energy of the vessel given in Equation 2.86 is to remain valid, the Jacobian matrix defined in Equation 2.85 must be augmented to comply with the new dimensions of the quasi-coordinates. This is achieved by the following modification of the Jacobian matrix

$$\mathbf{J}_b = \begin{bmatrix}\mathbf{J}_{v_b} & \mathbf{0}_{3xn} \\ \mathbf{J}_{\omega_b} & \mathbf{0}_{3xn}\end{bmatrix} \tag{5.18}$$

With this, the total kinetic energy of the system can be expressed as

$$\begin{aligned}T(\mathbf{q},\boldsymbol{\omega}) &= T_b(\mathbf{q},\boldsymbol{\omega}) + \sum_{j=1}^{n}(T_j(\mathbf{q},\boldsymbol{\omega})) \\ &= \frac{1}{2}\boldsymbol{\omega}^T\mathbf{B}(\mathbf{q})\boldsymbol{\omega}\end{aligned} \tag{5.19}$$

With the expression of the total kinetic energy of the system, the state-space model is obtained by the steps derived in Section 2.3.2, and a kinematic model of the combined vessel and crane system can be implemented in an IC-field.

5.1.4 Crane and vessel kinematics

The process of implementing the interconnected vessel and crane kinematics into an IC-field requires the development of a DLL-file. Note that this is to limit the computational complexity of the calculations that are performed directly in 20-Sim. Therefore, a Maple-script is created to include the combined system kinematics. First, the expression of the mass-inertia matrix $\mathbf{B}_b(\mathbf{q})$ of the vessel is implemented by following the steps derived in Section 2.3. Then, the position vectors, Jacobian matrices, and inertia matrices that were derived previously are inserted, and the total mass-inertia $\mathbf{B}(\mathbf{q})$ is derived in accordance with the preceding section. Unlike the development of the kinematics of the stationary crane, the interconnected vessel and crane kinematics are derived with the use of the quasi-equations of motion. Consequently, the algebraic expressions of the matrices $\boldsymbol{\gamma}$ and $\boldsymbol{\omega}\frac{\partial \mathbf{B}(\mathbf{q})}{\partial \mathbf{q}}$ must be derived in addition to the mass-inertia matrix. The two matrices are derived with the expressions defined in Equation 2.89 and Equation 2.94, respectively. Then, the algebraic expressions of the three matrices are exported as C-code in preparation of developing a DLL-file. Note that the MATLAB-script, which was designed for the crane simulation model, is modified to be capable of transforming the new C-code to a format that complies with the requirements of 20-Sim regarding DLL-files. The DLL-file is then built in Microsoft Visual Studio by inserting the modified C-code into a DLL-project. Note that the DLL-file is designed to receive an input vector containing the crane and vessel parameters and give an output vector containing the required elements of the three matrices $\boldsymbol{\gamma}$, $\boldsymbol{\omega}\frac{\partial \mathbf{B}(\mathbf{q})}{\partial \mathbf{q}}$ and $\mathbf{B}(q)$. The Maple- and MATLAB-scripts are referred to in Appendix B.

In addition to the kinematics of the rigid bodies, both added mass and added centripetal and Coriolis effects must be included for the floating vessel. Considering that the crane is above sea level, the added mass-inertia and centripetal and Coriolis matrices given in Equation 2.102 and Equation 2.104, respectively, are augmented to the following

$$\mathbf{B}_A = \begin{bmatrix} A_{11}(0) & 0 & 0 & 0 & 0 & 0 & \mathbf{0}_{1x3} \\ 0 & A_{22}(0) & 0 & 0 & 0 & 0 & \mathbf{0}_{1x3} \\ 0 & 0 & A_{33}(\omega_{heave}) & 0 & 0 & 0 & \mathbf{0}_{1x3} \\ 0 & 0 & 0 & A_{44}(\omega_{roll}) & 0 & 0 & \mathbf{0}_{1x3} \\ 0 & 0 & 0 & 0 & A_{55}(\omega_{pitch}) & 0 & \mathbf{0}_{1x3} \\ 0 & 0 & 0 & 0 & 0 & A_{66}(0) & \mathbf{0}_{1x3} \\ \mathbf{0}_{3x1} & \mathbf{0}_{3x1} & \mathbf{0}_{3x1} & \mathbf{0}_{3x1} & \mathbf{0}_{3x1} & \mathbf{0}_{3x1} & \mathbf{0}_{3x3} \end{bmatrix} \tag{5.20}$$

$$\mathbf{C}_A = \begin{bmatrix} \mathbf{0}_{3x3} & -\mathbf{S}(\mathbf{A}_{11}\mathbf{v}^b_{b/0} + \mathbf{A}_{12}\boldsymbol{\omega}^b_{b/0}) & \mathbf{0}_{3x3} \\ -\mathbf{S}(\mathbf{A}_{11}\mathbf{v}^b_{b/0} + \mathbf{A}_{12}\boldsymbol{\omega}^b_{b/0}) & -\mathbf{S}(\mathbf{A}_{21}\mathbf{v}^b_{b/0} + \mathbf{A}_{22}\boldsymbol{\omega}^b_{b/0}) & \mathbf{0}_{3x3} \\ \mathbf{0}_{3x3} & \mathbf{0}_{3x3} & \mathbf{0}_{3x3} \end{bmatrix}$$

The proposed decoupled added mass matrix is related to maneuvering theory, but considering that the vessel will be kept stationary with mooring lines, the seakeeping theory could be deemed more accurate. However, to simplify the process, the added mass coefficients are chosen as constant values that are related to the average added mass value over a frequency range. Thus, the added mass values are based on the experiments performed on 2D rectangular cylinders that were carried out by Vugts (1968). The experimental data regarding added mass in sway motion is on average 40% of the mass of the 2D section. In heave motion, the average value of a 2D section with a beam four times the size of the draft is roughly 125% of the mass. As stated in Pettersen (2007), the added mass in roll is small and often below 25% of the inertia about the x-axis. This statement is confirmed with Vugts (1968), and the added mass in roll is set to 20% of the inertia about the x-axis. When it comes to the added mass in surge, pitch, and yaw, they are set to 40% of their mass and inertia, respectively, because accurate estimates are not available without utilizing potential theory programs.

With the definition of the added mass, the kinematics can be implemented into an IC-field. The code contained inside the IC-field is referred to in Appendix B. Furthermore, it is convenient to divide the quasi-coordinates into the individual generalized velocities when creating interfaces to the IC-field. Thereby, 1-junctions representing the linear velocities of the vessel, $\mathbf{v}^{\mathbf{b}}_{\mathbf{b/0}}$, the rotational velocities of the vessel, $\boldsymbol{\omega}^b_{b/0}$, and the crane joint velocities, $\dot{\mathbf{q}}_c$, can be connected to the IC-field. Note that each crane joint rate is represented by a separate 1-junction, as shown in Figure 5.3.

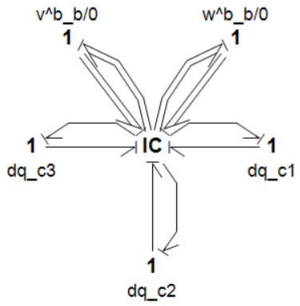

Figure 5.3: IC-field interfaced with the quasi-coordinates

5.1.5 Crane and vessel kinetics

In this case, the forces that act on the system are related to gravity, payloads, winches, wires, actuators, and hydrodynamic loads. Recall that the constitutive relation regarding the interfacing of generalized forces and generalized coordinates was formulated as follows in Equation 3.14 when developing the crane simulation model

$$\begin{aligned}\mathbf{f}^0_p &= \mathbf{J}_p \mathbf{f}^0_q \\ \mathbf{e}^0_q &= \mathbf{J}^T_p \mathbf{e}^0_p\end{aligned}$$

Consequently, an additional transformation must be applied to rotate the generalized forces into the body-fixed vessel frame in which the quasi-coordinates are given. Hence, the total constitutive relation in the case of a combined vessel and crane system becomes

$$\begin{aligned}\mathbf{f}^0_p &= \mathbf{J}_p \mathbf{R}^0_b(\boldsymbol{\Theta}) \mathbf{f}^b_q \\ \mathbf{e}^b_q &= \mathbf{J}^T_p \mathbf{R}^b_0(\boldsymbol{\Theta}) \mathbf{e}^0_p\end{aligned} \tag{5.21}$$

Note that either the three last rows or the three first rows of the Jacobian matrix can be omitted if only forces or moments are acting on the arbitrary point p, respectively.

5.1.6 Crane and vessel gravitational loads

Considering the constitutive relation given in Equation 5.21, the gravitational loads can be implemented in a similar manner to the method that was presented in Section 3.7.1. The only modification is the inclusion of another MTF-element that performs the rotational transformation from the inertial reference frame to the body-fixed vessel frame. An overview of the transformation of the gravitational forces is given in Figure 5.4. The Se-elements apply the gravitational force at the center of gravity of the jth body according to $\mathbf{F}_{cg_j} = [0,\ 0,\ -m_j g]$. Note that the gravitational load due to the mass of the vessel will be included when considering the restoring forces that act on the system.

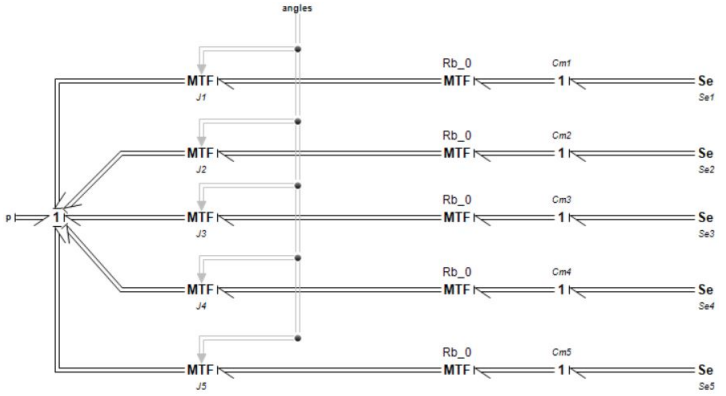

Figure 5.4: Interfacing gravitational loads to the IC-field of the combined kinematics

5.1.7 Actuators

The functionality of the actuators remains unchanged when the crane is attached to a floating vessel. On the other hand, the position vectors and Jacobian matrices developed for the crane simulation model in Section 3.7.2 must be modified to comply with the new configuration. Note that the position vectors given in Equation 3.15 stay unaltered because they are related to the local body-fixed frames defined on the crane. The position vectors to the upper connection points of the lower and upper crane boom actuators are given as follows

$$\mathbf{r}^b_{6/b} = \mathbf{r}^b_{2/b} + \mathbf{R}^b_2 \mathbf{r}^2_{6/2}, \qquad \mathbf{r}^b_{7/b} = \mathbf{r}^b_{3/b} + \mathbf{R}^b_3 \mathbf{r}^3_{7/3} \tag{5.22}$$

The Jacobian matrices are derived as previously described, and can be expressed as follows for the four connection points of the crane boom actuators

$$\begin{aligned}
\mathbf{J}^b_6 &= \begin{bmatrix} \mathbf{J}^{(v^b_{b/0})}_{v_b} & \mathbf{J}^{(v^b_{b/0})}_{\omega_b} & \mathbf{e}^b_1 \times (\mathbf{r}^b_{4/b} - \mathbf{r}^b_{1/b}) & \mathbf{0}_{3x2} \\ \mathbf{J}^{(\omega^b_{b/0})}_{v_b} & \mathbf{J}^{(\omega^b_{b/0})}_{\omega_b} & \mathbf{e}^b_1 & \mathbf{0}_{3x2} \end{bmatrix} \\
\mathbf{J}^b_7 &= \begin{bmatrix} \mathbf{J}^{(v^b_{b/0})}_{v_b} & \mathbf{J}^{(v^b_{b/0})}_{\omega_b} & \mathbf{e}^b_1 \times (\mathbf{r}^b_{6/b} - \mathbf{r}^b_{1/b}) & \mathbf{e}^b_2 \times (\mathbf{r}^b_{6/b} - \mathbf{r}^b_{2/b}) & \mathbf{0}_{3x1} \\ \mathbf{J}^{(\omega^b_{b/0})}_{v_b} & \mathbf{J}^{(\omega^b_{b/0})}_{\omega_b} & \mathbf{e}^b_1 & \mathbf{e}^b_2 & \mathbf{0}_{3x1} \end{bmatrix} \\
\mathbf{J}^b_8 &= \begin{bmatrix} \mathbf{J}^{(v^b_{b/0})}_{v_b} & \mathbf{J}^{(v^b_{b/0})}_{\omega_b} & \mathbf{e}^b_1 \times (\mathbf{r}^b_{5/b} - \mathbf{r}^b_{1/b}) & \mathbf{e}^b_2 \times (\mathbf{r}^b_{5/b} - \mathbf{r}^b_{2/b}) & \mathbf{0}_{3x1} \\ \mathbf{J}^{(\omega^b_{b/0})}_{v_b} & \mathbf{J}^{(\omega^b_{b/0})}_{\omega_b} & \mathbf{e}^b_1 & \mathbf{e}^b_2 & \mathbf{0}_{3x1} \end{bmatrix} \\
\mathbf{J}^b_9 &= \begin{bmatrix} \mathbf{J}^{(v^b_{b/0})}_{v_b} & \mathbf{J}^{(v^b_{b/0})}_{\omega_b} & \mathbf{e}^b_1 \times (\mathbf{r}^b_{7/b} - \mathbf{r}^b_{1/b}) & \mathbf{e}^b_2 \times (\mathbf{r}^b_{7/b} - \mathbf{r}^b_{2/b}) & \mathbf{e}^b_3 \times (\mathbf{r}^b_{7/b} - \mathbf{r}^b_{3/b}) \\ \mathbf{J}^{(\omega^b_{b/0})}_{v_b} & \mathbf{J}^{(\omega^b_{b/0})}_{\omega_b} & \mathbf{e}^b_1 & \mathbf{e}^b_2 & \mathbf{e}^b_3 \end{bmatrix}
\end{aligned} \tag{5.23}$$

The interfacing of the crane boom actuators to the IC-field is performed as described in Section 3.7.2, implying that the moduli of the MTF-elements are their respective Jacobian matrices. Note that the transformation of the local actuator forces that were given in Equation 3.18 is valid if the rotation matrix $\mathbf{R}^0_1$ is replaced with $\mathbf{R}^b_1$ as follows

$$\mathbf{F}^b_2 = F_{a2} \mathbf{R}^b_1 \begin{bmatrix} 0 \\ cos(\delta_1) \\ sin(\delta_1) \end{bmatrix}, \qquad \mathbf{F}^b_3 = F_{a3} \mathbf{R}^b_1 \begin{bmatrix} 0 \\ cos(\delta_2) \\ sin(\delta_2) \end{bmatrix} \tag{5.24}$$

When considering the actuator that rotates the base, it is connected directly to the generalized velocity $\dot{\mathbf{q}}_{c_1}$ and no further modifications must be performed.

5.1.8 Main wire and payload

The force applied by the main wire onto the crane is considered as a generalized force acting on the tip of the crane. Thus, when following the steps derived in Section 3.7.3, the position vector to the crane tip becomes

$$\mathbf{r}^b_{8/b} = \mathbf{r}^b_{3/b} + \mathbf{R}^b_3 \mathbf{r}^3_{8/3} \tag{5.25}$$

yielding the following Jacobian matrix

$$\mathbf{J}^b_{10} = \begin{bmatrix} \mathbf{J}^{(v^b_{b/0})}_{v_b} & \mathbf{J}^{(v^b_{b/0})}_{\omega_b} & \mathbf{e}^b_1 \times (\mathbf{r}^b_{8/b} - \mathbf{r}^b_{1/b}) & \mathbf{e}^b_2 \times (\mathbf{r}^b_{8/b} - \mathbf{r}^b_{2/b}) & \mathbf{e}^b_3 \times (\mathbf{r}^b_{8/b} - \mathbf{r}^b_{3/b}) \\ \mathbf{J}^{(\omega^b_{b/0})}_{v_b} & \mathbf{J}^{(\omega^b_{b/0})}_{\omega_b} & \mathbf{e}^b_1 & \mathbf{e}^b_2 & \mathbf{e}^b_3 \end{bmatrix} \tag{5.26}$$

The wire model is implemented as described in Section 3.7.3. Considering that the forces in the wire model are given in the inertial reference frame, the constitutive relation defined in Equation 5.21 must be applied. Hence, the interfacing with the IC-field is performed identically to the gravitational loads.

5.1.9 Vessel restoring terms

As defined in Section 2.3.3, the restoring forces are related to the gravitational and buoyancy forces. With the vessel modeled as a rectangular barge, the displaced volume can be approximated to the following with a small angle assumption

$$\nabla \approx A_w H_d \approx LBH_d \tag{5.27}$$

Here A_w, L, B, and H_d are the waterplane area, length, width, and draft of the barge, respectively. The buoyancy force becomes the following by applying Equation 2.96

$$\mathbf{f}^0_b = \rho_w LBH_d \mathbf{g} \tag{5.28}$$

Considering that the buoyancy force is a function of the vertical position of the vessel relative to the water surface, it acts similarly to a spring. This implies that it should be implemented as a C-element. The gravitational force related to the vessel is given below

$$\mathbf{f}^0_b = m_b \mathbf{g} \tag{5.29}$$

and is implemented as a Se-element. By recalling that the linear restoring force is the sum of the buoyancy force and the weight of the vessel, the two forces can be connected to a 1-junction. A third power bond, representing the linear restoring force, can then be connected to the 1-junction representing the linear velocity of the vessel. Note that the restoring forces are given in the inertial frame, hence a rotational transformation is executed in an MTF-element prior to being connected to the linear velocity of the vessel.

The general expression of the restoring torques was given in Equation 2.98 and is approximated by cross multiplying the buoyancy force with a righting arm, GZ, that is found through the metacentric height. The metacentric height is expressed as

$$GM = KB + BM - KG \tag{5.30}$$

where GM is the metacentric height, KB is the distance between the keel and center of buoyancy, BM is the distance between the center of buoyancy and metacenter, and KG is the distance between the keel and the center of gravity. In this case, the center of buoyancy is considered to be located at half the depth of the draft of the vessel. The center of gravity is constantly located at the geometric center of the barge. Lastly, BM is defined as the ratio between the inertia and the volumetric displacement of the vessel. Hence, the transverse and longitudinal metacentric height becomes

$$\begin{aligned} GM_T &= \frac{1}{2}H_d + \frac{I_x}{\nabla} - \frac{1}{2}H \\ GM_L &= \frac{1}{2}H_d + \frac{I_y}{\nabla} - \frac{1}{2}H \end{aligned} \tag{5.31}$$

Note that the inertias I_x and I_y are considered constant even though they vary with the orientation of the vessel. Considering small rotations in roll and pitch, the righting arm can be expressed as

$$\mathbf{GZ} = \begin{bmatrix} -GM_L sin(\theta) \\ GM_T sin(\phi) \\ 0 \end{bmatrix} \tag{5.32}$$

The cross product of the righting arm and the buoyancy force is implemented into a C-element that is connected to the 1-junction representing the rotational velocities of the vessel.

5.1.10 Vessel damping forces

As a simplification, only the nonlinear vortex shedding and the linear viscous damping are implemented in this model. The nonlinear vortex shedding is based on the expression given in Equation 2.106 and is implemented in an R-element that is connected to the 1-junction representing the linear velocity of the vessel. In addition, the linear viscous damping terms that are related to the linear velocities are included in the same R-element. The magnitudes of the linear viscous damping terms are based on the expressions given in Equation 2.108. As these expressions were derived as a tool for estimating the viscous damping terms, they are further tuned until the vessel obtains reasonable damping for surge, sway, and heave motions. Note that the relative velocity of the vessel is utilized when calculating the damping forces related to the linear velocities. Hence, a current model is included. In this case, the current is modeled as an incoming velocity with a magnitude in the north and east directions that ramp up to predefined values. Note that the current is defined in the inertial reference frame and must be rotated into the body-fixed vessel frame before including it in the R-element. Furthermore, linear viscous damping is implemented for roll, pitch, and yaw by connecting an R-element to the 1-junction representing the rotational velocities of the vessel. The estimates given in Equation 2.108 are used in the process of encountering damping terms that result in a logical vessel behavior. For an overview of the implementation, refer to Figure 5.6.

5.1.11 Wave excitation model

The wave excitation model is taken directly from the vessel model developed in Rokseth et al. (2017). It is based on the potential wave theory presented in Section 2.3.3 and applies a set of simplifications regarding the integration of the pressure field over the wetted surface of the vessel. The wetted surface is divided into small square elements where the sum of the contributions onto each individual element is used as an approximation of the wave excitation loads acting on the vessel. The partitioning of the wetted surface is limited to the bottom of the vessel. This is shown in Figure 5.5 where β is the angle between the heading of the vessel and the propagating waves. Note that the vessel is modeled as a rectangular barge to simplify the process of evaluating the hydrodynamic loads.

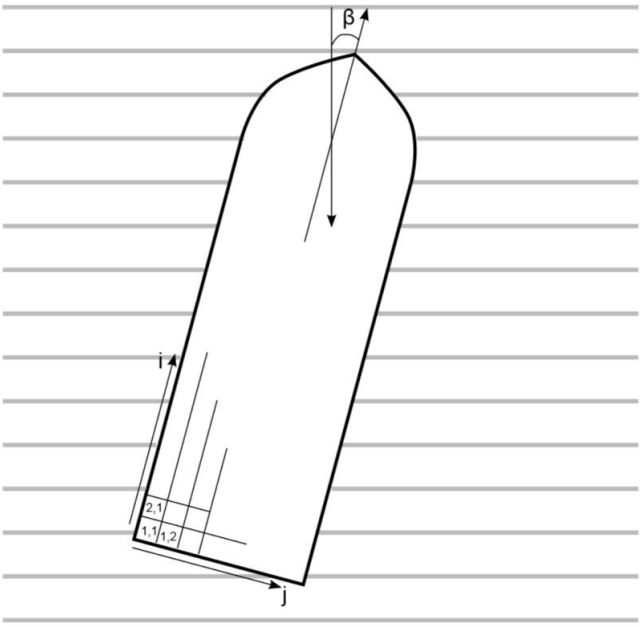

Figure 5.5: Partitioning of wetted surface. Taken from Rokseth et al. (2017)

With the proposed partitioning, Equation 2.113 is applied to express the wave excitation loads, as explained in Rokseth et al. (2017). The Froude-Krylov pressure is multiplied by the area of a wetted element to find the load contribution from the element. When it comes to the added mass, it is assumed equally distributed over the wetted elements. This implies that the added mass matrix $\mathbf{A}_{11}$, which was defined in Equation 2.105, is divided by the number of wetted elements. The wave acceleration terms are evaluated at the center of each individual wetted element. Hence, the wave excitation force contribution from a wetted element can be expressed as follows (Rokseth et al., 2017)

$$\begin{bmatrix} F^b_{surge_k} \\ F^b_{sway_k} \\ F^b_{heave_k} \end{bmatrix} = \begin{bmatrix} 0 \\ 0 \\ p_{FK}(x_i, z_i) \end{bmatrix} + \frac{1}{n_j n_i} \mathbf{A}_{11} \mathbf{R}^b_0(\boldsymbol{\Theta}) \begin{bmatrix} a_1(x_i, z_i) \\ a_2(x_i, z_i) \\ a_3(x_i, z_i) \end{bmatrix} \tag{5.33}$$

Here n_j and n_i are the numbers of wetted elements in the i- and j-directions depicted in Figure 5.5. The subscript k denotes an element of the wetted surface. Note that $a_2 = 0$ when the wave is modeled to propagate along the inertial x-axis. The total wave excitation force on the vessel is the

sum of the contribution of the wetted elements

$$\begin{bmatrix} F^b_{surge} \\ F^b_{sway} \\ F^b_{heave} \end{bmatrix} = \sum_{k=1}^{K} \begin{bmatrix} F^b_{surge_k} \\ F^b_{sway_k} \\ F^b_{heave_k} \end{bmatrix} \tag{5.34}$$

where K is the total number of wetted elements. The torques are found as the sum of the cross products of the wave excitation forces and the position vectors from the pivot point of the vessel to a wetted element

$$\begin{bmatrix} M^b_{surge} \\ M^b_{sway} \\ M^b_{heave} \end{bmatrix} = \sum_{k=1}^{K} \mathbf{r}^b_k \times \begin{bmatrix} F^b_{surge_k} \\ F^b_{sway_k} \\ F^b_{heave_k} \end{bmatrix} \tag{5.35}$$

These equations were implemented into a DLL-file in Rokseth et al. (2017), and that exact DLL-file is applied to calculate the wave excitation loads in this combined vessel and crane model. Note that second-order mean drift loads are included in the DLL-file, as explained in Rokseth et al. (2017).

5.1.12 Vessel mooring lines

The vessel is moored to prevent it from drifting from its initial configuration due to incident waves and current. In this case, the mooring lines are simplified to act as linear and rotational springs about the center of gravity of the vessel. The linear springs are related to the linear velocity of the vessel, hence a C-element is connected to the 1-junction that represents the linear velocities. On the other hand, the rotational springs are related to the angular velocity of the vessel and a C-element is therefore connected to the 1-junction that represents the rotational velocities. Note that the spring loads are defined in the inertial reference frame and must be rotated into the body-fixed vessel frame with MTF-elements. To tune the spring stiffnesses, the SIMA model provided by Subsea 7 is taken as a reference in regard to the vessel motion during different sea states. Since the mooring line forces are unavailable in the given SIMA model, the different spring stiffnesses are simply tuned to limit the vessel motion such that it resembles the motion of the ship in SIMA. Consequently, there are uncertainties regarding the effect the mooring lines have on the vessel response.

5.1.13 Complete vessel and crane system

The components that describe the kinematics and kinetics of the system are implemented in the bond graph language, as depicted in Figure 5.6. Note how the right-hand side of the bond graph model is identical to the crane simulation model as only the Jacobian matrices are replaced to comply with the new configuration. The crane is positioned port side of the vessel with its crane booms pointing along the positive y-axis. The complete system in its initial position is illustrated in Figure 5.7

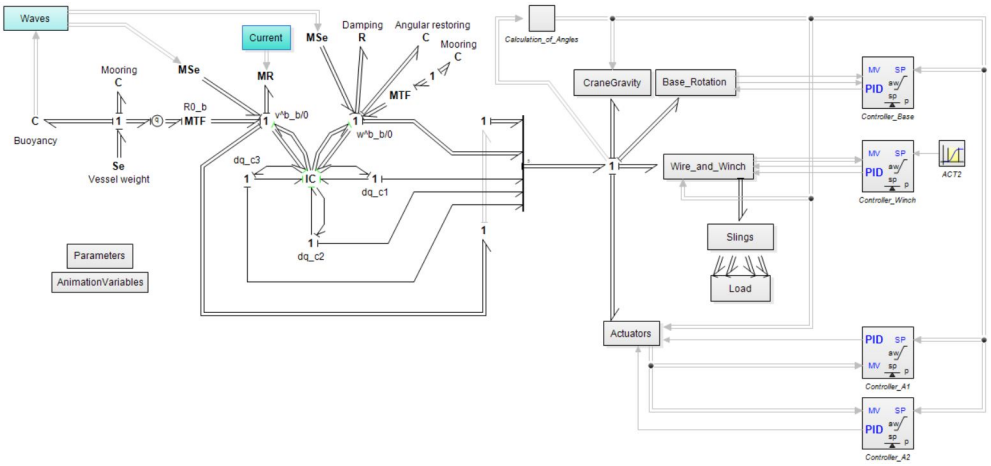

Figure 5.6: Vessel and crane bond graph model

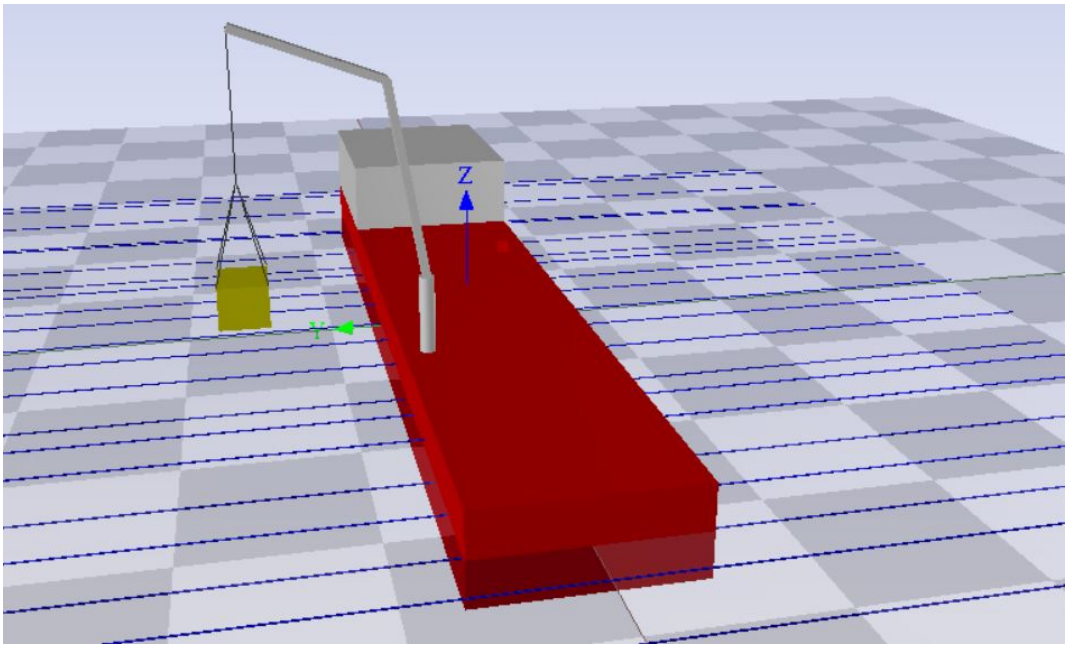

Figure 5.7: Vessel and crane 3D animation

5.2 Combined system results

As previously stated, the reader should be aware that the results presented in this section are given with respect to the scale of the model crane in the MCMR Lab. Consequently, the simulation data retrieved from the SIMA model are scaled according to the scaling laws defined in Chapter 4.

To begin with, the vessel is deployed in calm waters without waves or current. The vessel is anticipated to trim about the x-axis due to the torque that is generated by the crane when it is positioned at the port side of the ship. In Figure 5.8 it is shown that the vessel is trims to an angle of $-5.93°$, which with respect to a realistic scenario is larger than expected.

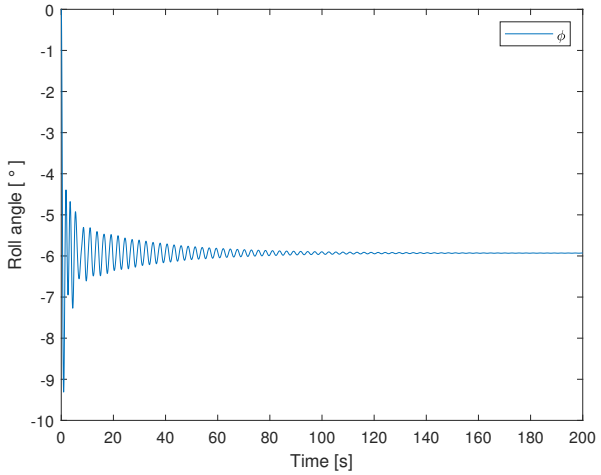

Figure 5.8: Roll angle with model crane masses

Hence, the mass of the crane is compared with data from a corresponding full-scale offshore knuckle boom crane. Considering that the model crane is designed with a maximum lifting capacity of 250 t in a full-scale scenario, the RL-K 7500 knuckle boom crane delivered by Liebherr (Liebherr, 2014) is a close fit with respect to maximum lifting capacity. A comparison of the relevant parameters is given in Table 5.1, where both full-scale and model scale values are presented.

Table 5.1: Crane comparison

Parameter	**RL-K 7500**	**Model crane**	**Unit**
Mass, model scale	42.56	111.1	kg
Main lift capacity, model scale	19.2	16	kg
Mass, full scale	665	1736	ton
Main lift capacity, full scale	300	250	ton

By evaluating the masses of the two cranes, it becomes evident that the model crane is significantly heavier than an actual offshore crane with similar lifting capacity. Hence, to evaluate the vessel response with respect to a realistic scenario, the mass of the model crane will be reduced. First, as the full-scale crane has a 20% larger lifting capacity, its mass is reduced according to the percentage difference of the lifting capacities, corresponding to $\frac{1}{6} \cdot 100\%$. Then, the mass of the model crane is reduced by the percentage difference between the masses of the two cranes. Hence, the mass of the model crane is reduced by the following percentage

$$p = \frac{111.1 - 42.56(1 - \frac{1}{6})}{111.1} = 0.6808 = 68.08\% \tag{5.36}$$

Considering that the model consists of five body parts of relevant masses, each one is reduced by the percentage p to generate an equally distributed reduction of the crane mass. With the decreased mass, the roll angle becomes $-2.77°$, as shown in Figure 5.9. In contrast to the previous roll angle, this is a more reasonable orientation when the crane booms are positioned directly port side with a payload of considerable mass. Furthermore, the SIMA model is simulated with an initial $-1.1°$ roll angle. Hence, the roll angle induced by the modified crane mass and payload is more suitable when comparing the two vessel responses. Another difference that should be pointed out is that the vessel is modeled as a barge, which implies the draft of the vessel is smaller in the 20-Sim model. The increased volume of the barge shape results in a draft of $H_d = 0.237m$ rather than the draft of $H_d = 0.320m$ that is present in SIMA. Consequently, differences are expected in the vessel and crane responses that are provided by the two simulation environments.

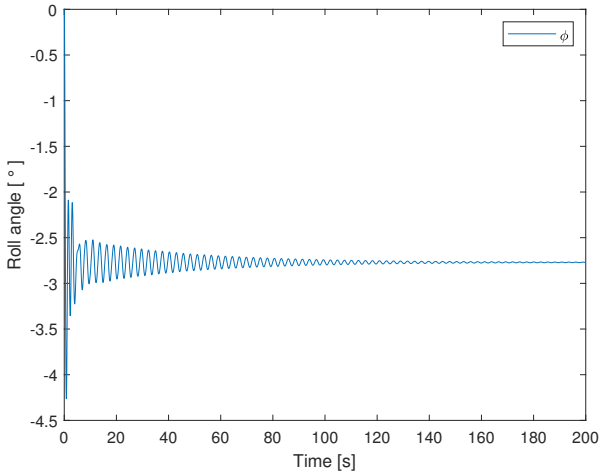

Figure 5.9: Roll angle with reduced model crane masses

With the reduced crane mass, the wave model is introduced to induce a vessel and crane motion. To begin with, the vessel is floating freely without mooring lines. To evaluate the response, a sea state with $H_s = 2.5m$ and $T_p = 10s$ is applied, which in model scale corresponds to $H_s = 0.1m$ and $T_p = 2.0s$. In Figure 5.10a it is shown that the vessel drifts in the negative x- and y-direction. This is expected when the incident wave is propagating in the negative x-axis and when the vessel has an initial roll angle due to the crane and payload. Furthermore, the vessel is rotated clockwise which is reasonable with the initial negative roll angle. To what extent the magnitudes of these translation and rotation motions correspond with a real scenario is unknown, but the overall behavior appears reasonable. When it comes to the heave motion, it oscillates in between magnitudes corresponding to the significant wave height with a frequency close to the peak period. Hence, the heave motion is deemed satisfactory. The oscillations in roll increase in magnitude when the vessel is turned with it broadside into the incoming waves, which is logical. Evidently, the vessel response appears to act according to the anticipated behavior, and the model seems to function properly.

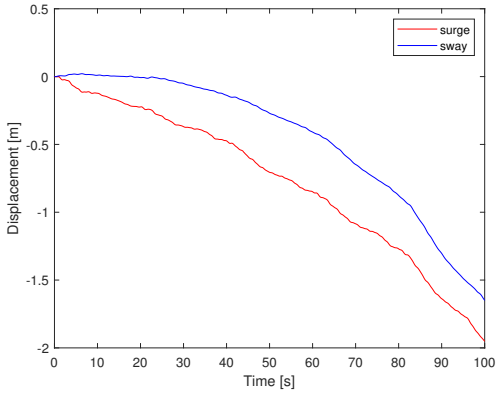

(a) Vessel surge and sway

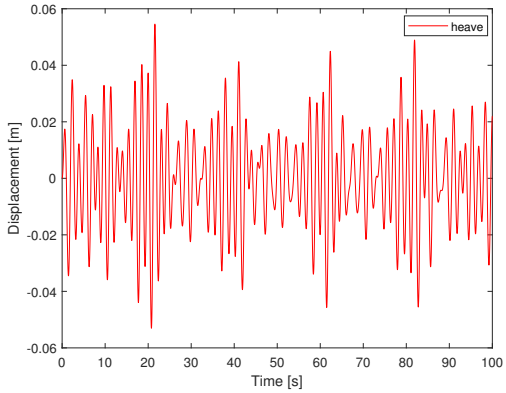

(b) Vessel heave

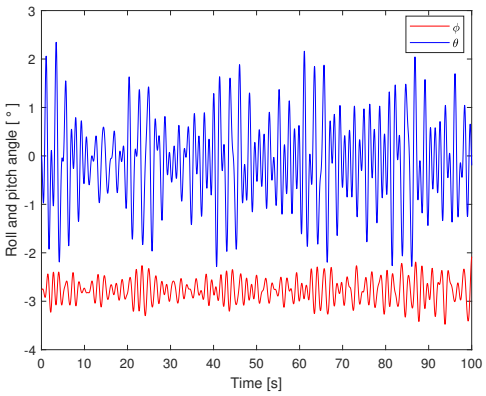

(c) Vessel roll and pitch

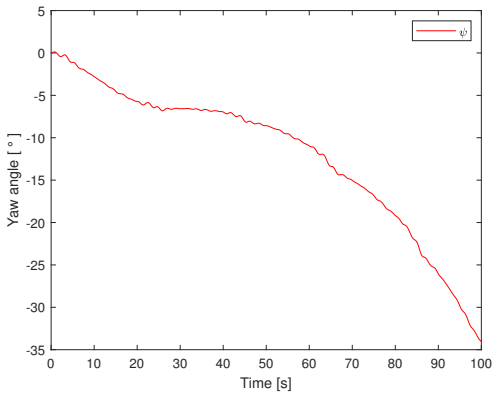

(d) Vessel yaw

Figure 5.10: Freely floating vessel motion

To further evaluate the vessel response, the simplified mooring line is attached to the vessel and the results are compared with the SIMA model provided by Subsea 7. The previously chosen sea state is applied to both simulation environments. The response of the two models is compared for all degrees of freedom in Figure 5.11. Note that all data are shifted such that the measurements begin at the origin of the plots, thus simplifying the comparison of the simulation models. Another important note is that the results are expected to be different when considering the simplifications that are applied in the 20-Sim model, e.g. modeling the vessel as a barge and approximating hydrodynamic coefficients. However, the comparison is carried out to ensure that the 20-Sim model behaves realistically.

The surge motion given in Figure 5.11a indicates that the amplitudes in surge are slightly smaller in the 20-Sim model compared to the SIMA model. Furthermore, the frequency of the surge motion appears to be lower in the 20-Sim model. The same is true for the sway motion, which additionally has significant differences in the motion pattern that initially tends to move in the negative y-direction. To improve the results, further adjusting the spring stiffnesses could lead to more accurate frequencies in the surge and sway motions since they are directly linked to the natural frequencies of the system. Furthermore, the implementation of the mooring line in 20-Sim is inaccurate compared to an actual mooring line configuration and a more precise model could lead to improved results. Additionally, since the parameters implemented in the 20-Sim model are based on simplified theories and approximations, deviations in the amplitudes of the motions are expected. Considering that the focus of the modeling process is not related to encountering correct parameters but rather verifying that the system has been implemented correctly, the results are deemed satisfactory. Hence, by obtaining more accurate hydrodynamic parameters and developing more

realistic mooring lines, the 20-Sim model is expected to behave in accordance with real vessels.

When evaluating the roll motion, Figure 5.11d indicates that the maximum peak-to-peak amplitudes of the motion in the two simulations are of the same magnitude. Regardless, the oscillation amplitudes are on average higher in the SIMA model. In this case, the frequency is observed to be roughly the same in the two cases. However, the roll motion in SIMA tends to favor rolling in the counter-clockwise direction, thus resulting in larger absolute values for the roll angles. The yaw angles have similar magnitudes, but the frequency in the 20-Sim model is slightly lower. Consequently, the simplified mooring line configuration could be responsible for the deviations in combination with the approximated hydrodynamic coefficients. Moving on to the motion in heave and pitch, they are both larger in the 20-Sim model. A reason could be related to the surface elevation that is generated in the two simulation models. In the SIMA model, the surface elevation is on average lower than the one produced in 20-Sim, which is shown in Figure 5.12. Note that both waves have maximum and minimum values within the specified significant wave height, but that the surface elevation generated in 20-Sim more frequently approaches the maximum values. Consequently, it is logical that the vessel is excited into greater heave and pitch motions. With unequal incident waves, it is difficult to compare the excitation of the two models. However, the comparison serves as a basis for evaluating the functionality of the vessel dynamics modeled in 20-Sim.

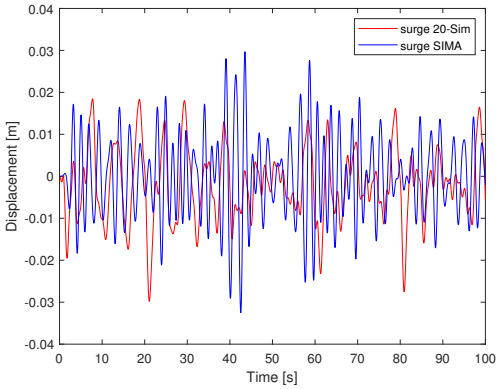

(a) Vessel surge

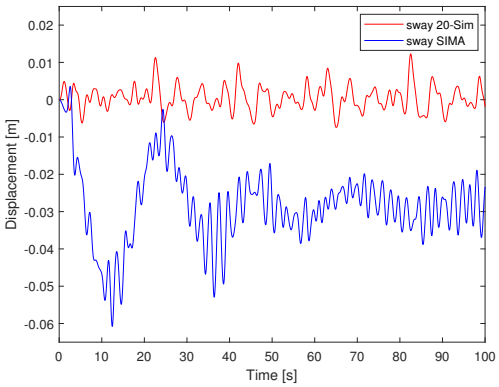

(b) Vessel sway

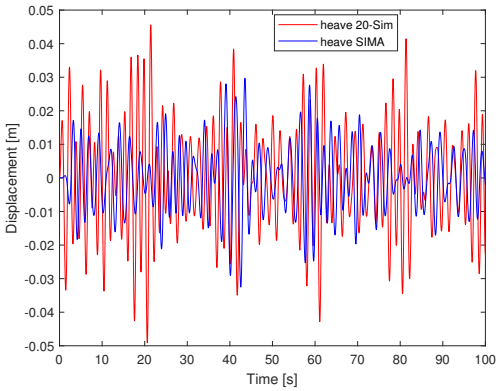

(c) Vessel heave

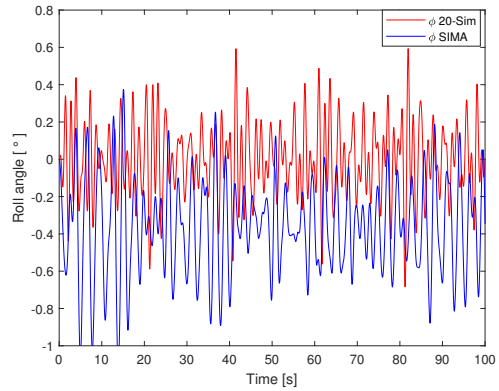

(d) Vessel roll

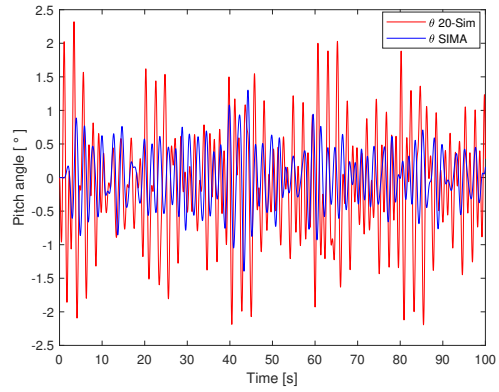

(e) Vessel pitch

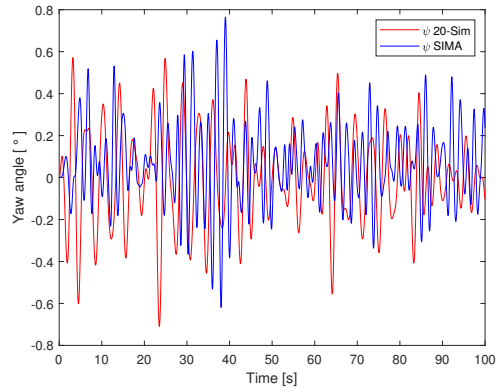

(f) Vessel yaw

Figure 5.11: Moored vessel in SIMA and 20-Sim

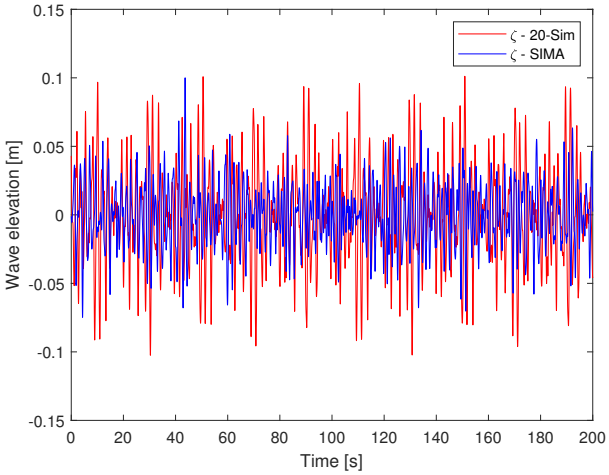

Figure 5.12: Comparison of surface elevations

With crane operations in mind, it is important to verify that the crane moves in accordance with the vessel motion. First, since the crane in the SIMA model remains fixed with respect to its initial configuration, PID-controllers are applied to the actuators that control the movement of the crane. They are designed to keep the crane angles close to their initial values during simulations. With the crane fixed to its initial configuration, the crane tip motion in the 20-Sim model is compared to the SIMA model. Note that the cranes in the two simulation models are not identical. This is because the crane in the 20-Sim model is related to the model crane in the MCMR Lab while the crane model in SIMA is of a real Huisman offshore crane. Hence, the crane tip in SIMA is located at a higher altitude relative to the vessel and additional deviations between the crane tip motions in the two models are expected. Regardless, they are compared to ensure that the results from the 20-Sim model are reasonable.

To begin with, the surge motion of the crane tip increase in both cases when compared to the surge motion of the vessel, which is expected due to the pitch motion of the vessels. Considering that the pitch motion is greater in the 20-Sim model, the surge motion of the crane tip is increased more in comparison to the surge motion of the vessel than in the SIMA model. On the other hand, the sway motion of the crane tips is increased with an equal magnitude, which is sensible when considering that the roll angles have similar peak-to-peak values. When it comes to the heave motion, the amplitudes of the crane tips are of greater magnitude than the response of the vessels. The increase is logical when considering that the cranes have been located a distance from the body-fixed vessel frame. Hence, they have the potential to be elevated further due to the pitch and roll motions of the vessel. Considering that the crane tip motion behaves as anticipated relative to the vessel motion, the system acts in a satisfactory manner. Therefore, the model is assumed to function properly. Hence, the model can be used as a basis for performing simulations in preparation for further testing of the model crane in the MCMR Lab on either a floating barge or a tripod system capable of imitating vessel motion.

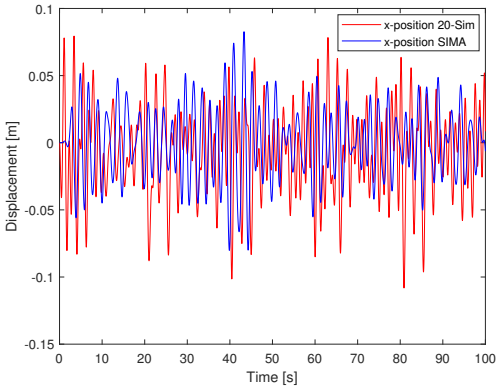

(a) Crane tip x-position

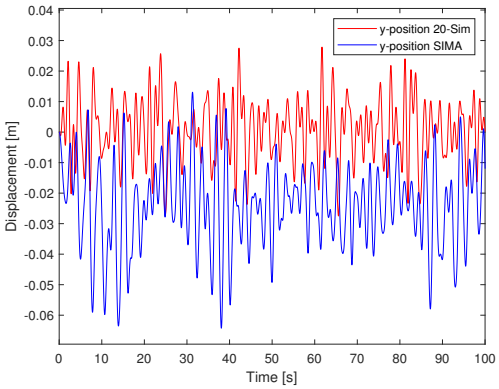

(b) Crane tip y-position

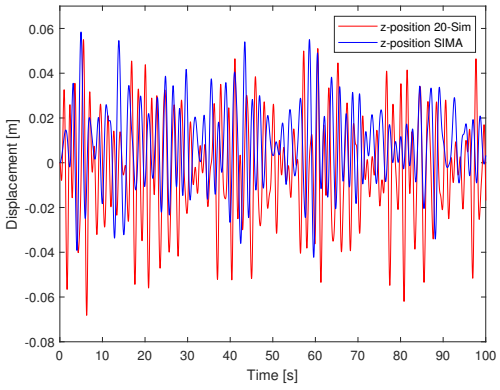

(c) Crane tip z-position

Figure 5.13: Crane tip displacement

6 | Conclusion and further work

6.1 Conclusion

This thesis has presented a comprehensive description of the theory that facilitates the extension and development of the crane simulation model. The derivation of the relevant system parameters and the procedures regarding their implementation into the simulation model have been systematically presented. In short terms, the process consisted of the derivation of rigid body models with Lagrangian mechanics, the development of DLL-files for reduced computational complexity, the inclusion of simplified wire and hydrodynamic models and the development of control algorithms for motion and tension control of the crane and tugger wires, respectively. All the models were derived through the development of mathematical models and implemented into a bond graph environment for testing and verification of the system behavior.

A case study was carried out to evaluate the effect of tugger winch systems. To induce a crane tip motion similar to the data obtained from a ship model in SIMA, an inverse dynamics controller was designed for the crane. By creating a simplified crane and payload model, the control algorithm was able to calculate the actuator forces that were required to move the crane tip according to a given crane tip reference signal. The reference signal consisted of the desired position, velocity, and acceleration, and was found with a mass-spring-damper reference model. Considering the filter properties of the reference model, a phase lag was generated, but since the motion pattern of the input and output remained similar, the results were deemed suitable for testing the tugger winch system. The scaling of the system and the response of the simplified wire dynamics were evaluated by a comparison of the snap loads that were induced with fixed length tugger wires. As expected, the two system responses were not identical due to the differences between the 20-Sim and SIMA models, but the tendencies were the same. Considering that the snap loads had larger peaks in the 20-Sim model, the effect of implementing an active tension controller in 20-Sim was assumed to be valid for a real case scenario. The active tension controller was able to prevent snap loads in rough sea states, but its capabilities related to motion control were not optimal. A phase lag between the crane tip and payload was induced, thus creating pendulum motions in the x- and y-directions that were larger than for the case with fixed length tugger wires. Consequently, more sophisticated control algorithms are required to improve the performance of the system. However, it should be noted that the motion was significantly smaller than for a case without tugger wires.

The second part of the thesis comprised of a case study related to extending the crane simulation model to include the dynamics of a floating vessel. The SIMA model served as a basis for verification of the combined vessel and crane system response. All model parameters were found in a combination of applied theory, tuning and comparison with the SIMA model. When the developed vessel and crane system was excited by incident waves, the system response appeared logical with respect to the applied sea state. Furthermore, when considering the uncertainties regarding the chosen hydrodynamic parameters and simplified mooring lines, the motion of the vessel and crane appeared to behave similarly to the ship and crane in the SIMA model. Consequently, the developed simulation tool should serve as a valid platform for further testing of the model crane in the scenario where it is deployed in a wave basin or mounted on a controllable tripod.

6.2 Further work

The extensions and modifications of the crane simulation model serve as a tool to further improve the model crane in the MCMR Lab. At this point in time, the Bachmann controller that was utilized in Gyberg (2017) and Evang (2017) is not connected to the crane. Furthermore, the current Bachmann controller lacks I/O ports with respect to the implementation of the suggested inverse dynamics controller. Thus additional ports must be added. For a comprehensive introduction to the Bachmann controller, refer to the guidelines developed in Gyberg (2017). Alternatively, the control algorithms can be implemented in LabVIEW, which is the software that currently is utilized when controlling the crane with joysticks. Another important note regarding the implementation of the inverse dynamics controller is the lack of force sensors on the actuators. Consequently, the desired forces that are calculated by the controller must be related to a voltage that sets the current drawn by the electric motors. Fortunately, considering that the output of the backstepping controller developed in Evang (2017) is a set of generalized forces, the applied method of controlling the actuators can be adapted. Furthermore, the inverse dynamics controller is susceptible to modeling errors and parameter uncertainties. Hence, the stability proof suggested in Appendix C could be implemented for a robust configuration.

The tugger winch system that was proposed in this thesis is a possible configuration, but a structural evaluation similar to the FEM analysis carried out in Gyberg (2017) is recommended to ensure structural integrity during operations. Furthermore, the tugger winch control algorithm must be further developed to improve the performance of the system regarding limiting pendulum motions. The method proposed in Ren et al. (2018) is of interest. Here, a model-based feedback linearization controller is developed to limit payload motion in the three planar motions surge, sway, and yaw. With an improved control algorithm, the requirements to pay-in speeds and pull-in forces can be reevaluated regarding the capabilities of the applied control system. Through further testing, the tugger winch system can be implemented in the MCMR Lab, together with the model crane. Then, model tests should be executed to verify the simulation model and the tensions that are induced in the tugger wires.

The interconnected crane and vessel simulation model was implemented with a variety of simplifications and estimations of hydrodynamic coefficients. Hence, potential theory software such as ShipX and WAMIT is suggested in the derivation of more accurate estimates. Furthermore, the mooring line system should be implemented in accordance with actual mooring line configurations to improve the behavior of the system with respect to a real scenario. Alternatively, a dynamic positioning system can be implemented as proposed in Rokseth et al. (2017). With the proposed improvements, the simulation model can serve as a platform for testing the crane and its auxiliary systems before employing it in a wave basin or mounting it on a controllable tripod.

Bibliography

Beard, R. W. (2012), *Small unmanned aircraft : theory and practice*, Princeton University Press, Princeton, N.J.

Borutzky, W. (2010), *Bond Graph Methodology: Development and Analysis of Multidisciplinary Dynamic System Models*, Springer London, London.

Chen, Q., Li, W. and Chen, G. (2017), 'Fuzzy p+id controller for a constant tension winch in a cable laying system', *Industrial Electronics, IEEE Transactions on* **64**(4), 2924–2932.

Deo, A. and Walker, I. (1992), Robot subtask performance with singularity robustness using optimal damped least-squares, *in* 'Proceedings - IEEE International Conference on Robotics and Automation', Vol. 1, Publ by IEEE, pp. 434–441.

DNV (2011), *Modelling and analysis of marine operations, recommended practice DNV-RP-H103*.

Driscoll, F., Nahon, M. and Lueck, R. (1998), 'A comparison between ship-mounted and cage-mounted passive heave compensation systems', *OCEANS '98 Conference Proceedings* **3**, 1449–1454.

Duindam, V., Macchelli, A., Stramigioli, S. and Bruyninckx, H. (2009), *Modeling and Control of Complex Physical Systems: The Port-Hamiltonian Approach*, Springer Berlin Heidelberg, Berlin, Heidelberg.

Evang, T. H. (2017), Marine crane dynamics lab - modelling and experimental validation, Master's thesis, NTNU.

Faltinsen, O. M. (1990), *Sea loads on ships and offshore structures*, Cambridge ocean technology series, Cambridge University Press, Cambridge.

Fossen, T. I. (2011), *Handbook of Marine Craft Hydrodynamics and Motion Control*, John Wiley and Sons, Ltd, Chichester, UK.

Ghosh, A. (2011), Scaling laws, *in* 'Mechanics over micro and nano scales', Springer, pp. 61–94.

Ginsberg, J. H. (1995), *Advanced engineering dynamics*, 2nd ed. edn, Cambridge University Press, Cambridge.

Groesen, E. v. and Molenaar, J. (2007), Dimensional analysis and scaling, *in* 'Continuum Modeling in the Physical Sciences', Society for Industrial and Applied Mathematics, pp. 1–1.

Gyberg, F. A. (2017), Design, modeling and control of a generic crane for marine applications, Master's thesis, NTNU.

Liebherr (2014), 'Ram luffing knuckle boom cranes RL - K'. Accessed: 2019-05-21.
URL: *https://www.liebherr.com/en/gbr/products/maritime-cranes/offshore-cranes/ram-luffing-knuckle-boom-cranes/ram-luffing-knuckle-boom-cranes.html*

Millikan, R. A. (1903), *Mechanics, Molecular Physics and Heat: A Twelve Weeks' College Course*, Boston, Ginn & Company.

Nakamura, Y. and Hanafusa, H. (1986), 'Inverse kinematic solutions with singularity robustness for robot manipulator control', *Journal of Dynamic Systems, Measurement and Control, Transactions of the ASME* **108**(3), 163–171.

Pedersen, E. and Engja, H. (2014), *Mathematical modelling and simulation of physical systems : lecture notes in course TMR4275 modelling, simulation and analysis of dynamic systems*, Department of Marine Technology. Norwegian University of Science and Technology, Trondheim.

Pedersen, T. and Pedersen, E. (2005), Bond graph modelling of marine seismic cables, *in* '2005 International Conference on Bond Graph Modeling and Simulation', SCS Publishing, pp. 92–98.

Pettersen, B. (2007), 'Marin teknikk 3 : hydrodynamikk'.

Razavy, M. (2006), *Classical and Quantum Dissipative Systems*, Published by Imperial College Press and distributed by World Scientific Publishing CO.

Ren, Z., Jiang, Z., Gao, Z. and Skjetne, R. (2018), 'Active tugger line force control for single blade installation', *Wind Energy* **21**(12), 1344–1358.

Rokseth, B. (2014), A bond graph approach for modelling systems of rigid bodies in spatial motion, Master's thesis, NTNU.

Rokseth, B., Skjong, S. and Pedersen, E. (2017), 'Modeling of generic offshore vessel in crane operations with focus on strong rigid body connections', *IEEE Journal of Oceanic Engineering* **42**(4), 846–868.

Sciavicco, L. and Siciliano, B. (2000), *Modelling and Control of Robot Manipulators*, Advanced textbooks in control and signal processing, second edition. edn, Springer-Verlag London, London.

Siciliano, B., Sciavicco, L., Villani, L. and Oriolo, G. (2009), *Robotics: Modelling, Planning and Control*, Advanced Textbooks in Control and Signal Processing, Springer London, London.

Skjong, S. and Pedersen, E. (2014), 'Modeling hydraulic winch system'.

Sørensen, A. J. (2013), *Marine control systems : propulsion and motion control of ships and ocean structures*, Vol. UK-2013-76 of *Kompendium (Norges teknisk-naturvitenskapelige universitet. Institutt for marin teknikk)*, Department of Marine Technology. Norwegian University of Science and Technology, Trondheim.

Vugts, J. (1968), 'The hydrodynamic coefficients for swaying, heaving and rolling cylinders in a free surface : by j. h. vugts'.

Woodacre, J., Bauer, R. and Irani, R. (2015), 'A review of vertical motion heave compensation systems', *Ocean Engineering* **104**, 140–154.

A | Simulation model parameters

A.1 Crane simulation model

The relevant parameters related to the model crane are given in Table A.1. For the remaining model parameters, refer to Appendix B.

Table A.1: Model crane parameters

Parameter	**Description**	**Value**	**Unit**
m_1	Mass of the crane base	67.0	kg
m_2	Mass of the lower crane boom	23.3	kg
m_3	Mass of the upper crane boom	5.5	kg
m_4	Mass of the lower actuator	8.5	kg
m_5	Mass of the upper actuator	6.8	kg
I_{1x}	Inertia of the crane base about the x-axis	0.0	kgm^2
I_{1y}	Inertia of the crane base about the y-axis	0.0	kgm^2
I_{1z}	Inertia of the crane base about the z-axis	1.8	kgm^2
I_{2x}	Inertia of the lower crane boom about the x-axis	9.2	kgm^2
I_{2y}	Inertia of the lower crane boom about the y-axis	0.0	kgm^2
I_{2z}	Inertia of the lower crane boom about the z-axis	9.4	kgm^2
I_{3x}	Inertia of the upper crane boom about the x-axis	1.6	kgm^2
I_{3y}	Inertia of the upper crane boom about the y-axis	0.0	kgm^2
I_{3z}	Inertia of the upper crane boom about the z-axis	1.5	kgm^2
I_{4x}	Inertia of the lower actuator about the x-axis	2.3	kgm^2
I_{4y}	Inertia of the lower actuator about the y-axis	0.0	kgm^2
I_{4z}	Inertia of the lower actuator about the z-axis	2.3	kgm^2
I_{5x}	Inertia of the upper actuator about the x-axis	1.1	kgm^2
I_{5y}	Inertia of the upper actuator about the y-axis	0.0	kgm^2
I_{5z}	Inertia of the upper actuator about the z-axis	1.1	kgm^2
Xcm_1	Distance to the crane base center of gravity, x-axis	0.0	m
Ycm_1	Distance to the crane base center of gravity, y-axis	-0.023	m
L_1	Length of lower crane boom	1.251	m
L_2	Length of upper crane boom	0.96	m
b	See Figure 3.1 for reference	0.461	m
a	See Figure 3.1 for reference	0.100	m
h	See Figure 3.1 for reference	0.495	m
w	See Figure 3.1 for reference	0.461	m
c	See Figure 3.1 for reference	0.190	m
u	See Figure 3.1 for reference	0.140	m
r	See Figure 3.1 for reference	0.140	m
s	See Figure 3.1 for reference	0.118	m
k	See Figure 3.1 for reference	0.533	m
n	See Figure 3.1 for reference	0.420	m
o	See Figure 3.1 for reference	0.324	m
p	See Figure 3.1 for reference	0.440	m
H	Height of the payload	0.2612	m
W	Width of the payload	0.4000	m
L	Length of the payload	0.3024	m
m	Mass of the payload	12.8	kg
I_x	Inertia of the payload about the x-axis	0.7607	kgm^2
I_y	Inertia of the payload about the y-axis	0.8153	kgm^2
I_z	Inertia of the payload about the z-axis	0.2749	kgm^2

A.2 Vessel and crane simulation model

Note that the crane parameters are identical to the one presented in Appendix A.1. The exceptions are the masses of the crane components that were reduced, as explained in Section 5.2.

Table A.2: Combined system parameters

Parameter	**Description**	**Value**	**Unit**
m_1	Reduced mass of the crane base	21.3864	kg
m_2	Reduced mass of the lower crane boom	7.4374	kg
m_3	Reduced mass of the upper crane boom	1.7556	kg
m_4	Reduced mass of the lower actuator	2.7132	kg
m_5	Reduced mass of the upper actuator	2.1706	kg
m_b	Mass of the barge	1973	kg
H_b	Height of the barge	0.540	m
B_b	Beam of the barge	1.280	m
L_b	Length of the barge	6.492	m
A_{11}	Added mass in surge	803.4	kg
A_{22}	Added mass in sway	803.4	kg
A_{33}	Added mass in heave	2510.6	kg
A_{44}	Added inertia in roll	83.7	kgm^2
A_{55}	Added inertia in pitch	2847.2	kgm^2
A_{66}	Added inertia in yaw	2905.7	kgm^2
B_{11}	Damping in surge	552.0	kg/s
B_{22}	Damping in sway	370.0	kg/s
B_{33}	Damping in heave	400.0	kg/s
B_{44}	Damping in roll	643.0	kgm^2/s
B_{55}	Damping in pitch	1500.0	kgm^2/s
B_{66}	Damping in yaw	300.0	kgm^2/s

B | Code and script attachments

This appendix gives an overview of the code and scripts that have been utilized in the development of the simulation models. Note that the Visual Studio projects are omitted since the content is generated directly by the attached MATLAB-Scripts. The relevant files are submitted in a zip-file that is organized with the following folders:

20-Sim models

- 3D models - Contains the STL-files made by Gyberg (2017) for the 3D visualization of the model crane.
- CraneAndVessel - Contains the 20-Sim EMX-file and the relevant DLL-files for the simulation of the combined crane and vessel system. Note that the emx-file contains the code for the IC-field, all the Jacobian matrices, and relevant system parameters.
- CraneAndTuggerWinch - Contains the 20-Sim EMX-file and the relevnat DLL-files for the simulation of the crane and tugger winch system. Additionally, a CSV-file with the crane tip motion for different sea states is included. Note that the EMX-file contains the code for the IC-field, all the Jacobian matrices, and relevant system parameters.
- SnapLoadsTesting.emx - Contains the simplified simulation model that is utilized to reduce the simulation time when evaluating the snap loads in the tugger wires.

MATLAB-scripts

- CraneAndBarge.m - Contains the MATLAB-script that processes the C-code generated by the Maple-script. Note that the code must be adjusted to comply with the setup in Maple if the crane and vessel model is modified.
- GeneralizedLoads.m - Contains the MATLAB-script that processes the C-code generated by the Maple-script related to the generalized forces of the actuators.

Maple-scripts

- BargeAndCrane.mw - Contains the Maple-script that generates the algebraic expressions of the combined crane and vessel system. Furthermore, it creates the C-code that must be processed by the MATLAB-scripts before building the DLL-files.
- Crane.mw - Contains the Maple-script that generates the algebraic expressions of the crane system. Furthermore, it creates the C-code that must be processed by the MATLAB-Scripts before building the DLL-files.
- Crane_MassAtCT.mw - Contains the Maple-script that generates the algebraic expressions of the crane system with a mass located at the crane tip. Furthermore, it creates the C-code that must be processed by the MATLAB-Scripts before building the DLL-files.

C | Robust inverse dynamics controller

This appendix presents a possible solution to the uncertainties regarding the dynamics developed for the simulation model and the actual dynamics of the model crane in the MCMR Lab. The derivation of a robust controller and its stability proof is based on the robust inverse dynamics controller developed for the joint space in Siciliano et al. (2009). Note that it is reasonable to assume that the assumptions that are applied in the proof must be modified before being valid for the model crane.

C.1 Robust controller stability proof

Recall that the general state-space model is expressed as follows

$$\mathbf{B}(\mathbf{q})\ddot{\mathbf{q}} + \mathbf{n}(\mathbf{q}, \dot{\mathbf{q}}) = \boldsymbol{\tau}$$

where

$$\mathbf{n}(\mathbf{q}, \dot{\mathbf{q}} = \mathbf{C}(\mathbf{q}, \dot{\mathbf{q}})\dot{\mathbf{q}} + \mathbf{g}(\mathbf{q})$$

With imperfect compensation, the control output $\boldsymbol{\tau}$ can be chosen as follows

$$\boldsymbol{\tau} = \hat{\mathbf{B}}(\mathbf{q})\mathbf{y} + \hat{\mathbf{n}}(\mathbf{q}, \dot{\mathbf{q}}) \tag{C.1}$$

where $\hat{\mathbf{B}}(\mathbf{q})$ and $\hat{\mathbf{n}}(\mathbf{q}, \dot{\mathbf{q}})$ are the estimates of the terms related to the model crane. Hence, the error of the estimates becomes the following

$$\begin{aligned} \tilde{\mathbf{B}} &= \hat{\mathbf{B}} - \mathbf{B} \\ \tilde{\mathbf{n}} &= \hat{\mathbf{n}} - \mathbf{n} \end{aligned} \tag{C.2}$$

Applying Equation C.1 as a nonlinear control law gives

$$\mathbf{B}\ddot{\mathbf{q}} + \mathbf{n} = \hat{\mathbf{B}}\mathbf{y} + \hat{\mathbf{n}} \tag{C.3}$$

Since $\mathbf{B}$ is invertible, the following is given

$$\ddot{\mathbf{q}} = \mathbf{y} + (\mathbf{B}^{-1}\hat{\mathbf{B}} - \mathbf{I})\mathbf{y} + \mathbf{B}^{-1}\tilde{\mathbf{n}} = \mathbf{y} - \boldsymbol{\eta} \tag{C.4}$$

where

$$\boldsymbol{\eta} = (\mathbf{B}^{-1}\hat{\mathbf{B}} - \mathbf{I})\mathbf{y} + \mathbf{B}^{-1}\tilde{\mathbf{n}} \tag{C.5}$$

By choosing $\mathbf{y}$ as previously proposed in Equation 2.138

$$\mathbf{y} = \mathbf{J}^{-1}(\ddot{\mathbf{r}}_d + \mathbf{K}_d\dot{\tilde{\mathbf{r}}} + \mathbf{K}_p\tilde{\mathbf{r}} - \dot{\mathbf{J}}\dot{\mathbf{q}})$$

and applying the expression for the generalized acceleration given in Equation 2.136

$$\ddot{\mathbf{q}} = \mathbf{J}^{-1}(\ddot{\mathbf{r}} - \dot{\mathbf{J}}\dot{\mathbf{q}})$$

the following error dynamics are derived

$$\ddot{\tilde{\mathbf{r}}} + \mathbf{K}_d\dot{\tilde{\mathbf{r}}} + \mathbf{K}_p\tilde{\mathbf{r}} = \mathbf{J}\boldsymbol{\eta} \tag{C.6}$$

Hence, the proposed linear PD controller is no longer sufficient since the described system is nonlinear because $\boldsymbol{\eta}$ is a nonlinear function. Therefore, the Lyapunov direct method is applied to derive a controller that ensures error convergence to zero while tracking a trajectory even with parameter uncertainties. Consequently, the following control law is proposed

$$\mathbf{y} = \mathbf{J}^{-1}(\ddot{\mathbf{r}}_d + \mathbf{K}_d\dot{\tilde{\mathbf{r}}} + \mathbf{K}_p\tilde{\mathbf{r}} - \dot{\mathbf{J}}\dot{\mathbf{q}} + \boldsymbol{\omega}) \tag{C.7}$$

where $\boldsymbol{\omega}$ is included to guarantee robustness with respect to the parameter uncertainties. In this case, the following error dynamics are given

$$\ddot{\tilde{\mathbf{r}}} = -\mathbf{K}_d\dot{\tilde{\mathbf{r}}} - \mathbf{K}_p\tilde{\mathbf{r}} - \boldsymbol{\omega} + \mathbf{J}\boldsymbol{\eta} \tag{C.8}$$

By choosing the system states as follows

$$\boldsymbol{\xi} = \begin{bmatrix} \tilde{\mathbf{r}} \\ \dot{\tilde{\mathbf{r}}} \end{bmatrix} \tag{C.9}$$

the following first order differential matrix equation is obtained

$$\dot{\boldsymbol{\xi}} = \mathbf{H}\boldsymbol{\xi} + \mathbf{D}(\mathbf{J}\eta - \boldsymbol{\omega}) \tag{C.10}$$

where $\mathbf{H}$ and $\mathbf{D}$ are $2n \times 2n$ and $2n \times n$ matrices, respectively, expressed as follows

$$\mathbf{H} = \begin{bmatrix} \mathbf{0} & \mathbf{I} \\ -\mathbf{K}_p & -\mathbf{K}_d \end{bmatrix}, \quad \mathbf{D} = \begin{bmatrix} \mathbf{0} \\ \mathbf{I} \end{bmatrix} \tag{C.11}$$

Here, the gain matrices are positive definite and given as follows

$$\begin{aligned} \mathbf{K}_p &= diag[\omega_{n1}^2, ..., \omega_{nn}^2] \\ \mathbf{K}_d &= diag[2\zeta_1\omega_{n1}, ..., 2\zeta_n\omega_{nn}] \end{aligned} \tag{C.12}$$

A Lyapunov function candidate is proposed to prove the stability of the controller

$$\mathbf{V}(\boldsymbol{\xi}) = \boldsymbol{\xi}^T\mathbf{Q}\boldsymbol{\xi} > 0, \quad \forall\ \boldsymbol{\xi} \neq \mathbf{0} \tag{C.13}$$

where $\mathbf{Q}$ is a $2n \times 2n$ positive definite matrix. By differentiating the Lyapunov function candidate and inserting the expression in Equation C.10, the following is obtained

$$\begin{aligned}\dot{\mathbf{V}}(\boldsymbol{\xi}) &= \dot{\boldsymbol{\xi}}^T\mathbf{Q}\boldsymbol{\xi} + \boldsymbol{\xi}\mathbf{Q}\dot{\boldsymbol{\xi}} \\ &= (\boldsymbol{\xi}^T\mathbf{H}^T + (\mathbf{J}\boldsymbol{\eta} - \boldsymbol{\omega}^T\mathbf{D}^T)\mathbf{Q}\boldsymbol{\xi} + \boldsymbol{\xi}^T\mathbf{Q}(\mathbf{H}\boldsymbol{\xi} + \mathbf{D}(\mathbf{J}\boldsymbol{\eta} - \boldsymbol{\omega})) \\ &= \boldsymbol{\xi}^T(\mathbf{H}^T\mathbf{Q} + \mathbf{Q}\mathbf{H})\boldsymbol{\xi} + (\mathbf{J}\boldsymbol{\eta} - \boldsymbol{\omega})^T\mathbf{D}^T\mathbf{Q}\boldsymbol{\xi} + \boldsymbol{\xi}^T\mathbf{Q}\mathbf{D}(\mathbf{J}\boldsymbol{\eta} - \boldsymbol{\omega}) \\ &= \boldsymbol{\xi}^T(\mathbf{H}^T\mathbf{Q} + \mathbf{Q}\mathbf{H})\boldsymbol{\xi} + 2\boldsymbol{\xi}^T\mathbf{Q}\mathbf{D}(\mathbf{J}\boldsymbol{\eta} - \boldsymbol{\omega})\end{aligned} \tag{C.14}$$

Note that the last two terms in the second to the last simplification are equal since the expressions are scalar values that are the transposed of one another. Obviously, a scalar value is equal to its transposed value. Furthermore, the matrix $\mathbf{H}$ is chosen such that it only has negative eigenvalues. Hence, the following definition can be applied

$$\mathbf{H}^T\mathbf{Q} + \mathbf{Q}^T\mathbf{H} = -\mathbf{P} \tag{C.15}$$

where any symmetric positive definite matrix $\mathbf{P}$ results in a unique positive definite matrix $\mathbf{Q}$. Consequently, the derivative of the Lyapunov function candidate becomes the following

$$\dot{\mathbf{V}}(\boldsymbol{\xi}) = -\boldsymbol{\xi}^T\mathbf{P}\boldsymbol{\xi} + 2\boldsymbol{\xi}^T\mathbf{Q}\mathbf{D}(\mathbf{J}\boldsymbol{\eta} - \boldsymbol{\omega}) \tag{C.16}$$

It is obvious that the first term is negative definite while the second term depends on the choice of the control parameter $\boldsymbol{\omega}$. By setting

$$\mathbf{z} = \mathbf{D}^T\mathbf{Q}\boldsymbol{\xi} \tag{C.17}$$

the second term is expressed as $\mathbf{z}^T(\mathbf{J}\boldsymbol{\eta} - \boldsymbol{\omega})$. The control parameter is then chosen to the following

$$\boldsymbol{\omega} = \frac{\rho}{||\mathbf{z}||}\mathbf{z}, \quad \rho > 0 \tag{C.18}$$

which gives

$$\begin{aligned}\mathbf{z}^T(\mathbf{J}\boldsymbol{\eta} - \boldsymbol{\omega}) &= \mathbf{z}^T\mathbf{J}\boldsymbol{\eta} - \frac{\rho}{||\mathbf{z}||}\mathbf{z}^T\mathbf{z} \\ &\leq ||\mathbf{z}||\,||\mathbf{J}\boldsymbol{\eta}|| - \rho||\mathbf{z}|| \\ &= ||\mathbf{z}||(||\mathbf{J}\boldsymbol{\eta}|| - \rho)\end{aligned} \tag{C.19}$$

Consequently, ρ must be chosen such that

$$\rho \geq ||\mathbf{J}\boldsymbol{\eta}||, \quad \forall\ \ddot{\mathbf{r}}_d,\ \mathbf{q},\ \dot{\mathbf{q}} \tag{C.20}$$

since $\boldsymbol{\eta}$ is a function of $\ddot{\mathbf{r}}_d$, $\mathbf{q}$ and $\dot{\mathbf{q}}$. Note that $\boldsymbol{\eta}$ contains terms related to $\mathbf{r}$ and $\dot{\mathbf{r}}$ but that they are directly related to the generalized coordinates and velocities. To ensure that the inequality holds, a set of assumptions are proposed in Siciliano et al. (2009). The first is given as follows

$$sup_{t\geq 0}\,||\ddot{\mathbf{r}}_d|| < \mathbf{Q}_M < \infty, \quad \forall\ \ddot{\mathbf{r}}_d \tag{C.21}$$

and it is satisfied by the fact that a reference trajectory cannot require an infinite acceleration. The second assumption is given by the following inequality

$$||\mathbf{I} - \mathbf{B}^{-1}\hat{\mathbf{B}}|| \leq \alpha \leq 1, \quad \forall\ \mathbf{q} \tag{C.22}$$

Since $\mathbf{B}$ is a positive definite matrix with upper and lower bound norms, the following inequality holds

$$0 < B_m \leq ||\mathbf{B}^{-1}|| \leq B_M < \infty, \quad \forall\ \mathbf{q} \tag{C.23}$$

Thus, a choice of $\hat{\mathbf{B}}$ that satisfies the assumption expressed in Equation C.22 always exists and is given as the following (Siciliano et al., 2009)

$$\hat{\mathbf{B}} = \frac{2}{B_M + B_m} \cdot \mathbf{I} \tag{C.24}$$

The resulting inequality of the second assumption becomes

$$||\mathbf{B}^{-1}\hat{\mathbf{B}} - \mathbf{I}|| \leq \frac{B_M - B_m}{B_M + B_m} = \alpha < 1 \tag{C.25}$$

Note that a more accurate estimate $\hat{\mathbf{B}}$ results in a smaller α. The last assumption is related to the fact that the joint ranges $\mathbf{q}$ are limited. Furthermore, even though unbounded joint velocities $\dot{\mathbf{q}}$ may arise in the limits of unstable systems, they are in reality saturated by the maximum velocities of the motors. Hence, the following inequality is proposed by assuming that the norm of the error estimate of the nonlinear function $\mathbf{n}$ is bounded (Siciliano et al., 2009)

$$||\hat{\mathbf{n}}|| \leq \Phi \leq \infty \tag{C.26}$$

With the suggested assumptions, the following is given

$$\begin{aligned} ||\mathbf{J}\boldsymbol{\eta}|| &= ||\mathbf{I} - \mathbf{B}^{-1}\hat{\mathbf{B}}||(||\ddot{\mathbf{r}}_d|| + ||\mathbf{K}||\,||\boldsymbol{\xi}|| + ||\boldsymbol{\omega}|| - ||\dot{\mathbf{J}}||\,||\dot{\mathbf{q}}||) - ||\mathbf{J}||\,||\mathbf{B}^{-1}||\,||\hat{\mathbf{n}}|| \\ &\leq \alpha Q_m + \alpha||\mathbf{K}||\,||\boldsymbol{\xi}|| + \alpha||\boldsymbol{\omega}|| - \alpha||\dot{\mathbf{J}}||\,||\dot{\mathbf{q}}|| - ||\mathbf{J}||B_m\Phi \end{aligned} \tag{C.27}$$

With $||\boldsymbol{\omega}|| = \rho$, the following is derived to satisfy the conditions defined in Equation C.20

$$\begin{aligned} \rho &\geq \alpha Q_m + \alpha||\mathbf{K}||\,||\boldsymbol{\xi}|| + \alpha||\boldsymbol{\omega}|| - \alpha||\dot{\mathbf{J}}||\,||\dot{\mathbf{q}}|| - ||\mathbf{J}||B_m\Phi \\ \Rightarrow \rho &\geq \frac{1}{1-\alpha}(\alpha Q_m + \alpha||\mathbf{K}||\,||\boldsymbol{\xi}|| - \alpha||\dot{\mathbf{J}}||\,||\dot{\mathbf{q}}|| - ||\mathbf{J}||B_m\Phi) \end{aligned} \tag{C.28}$$

Note that further assumptions might be necessary to ensure that the expression derived for ρ holds as it currently is dependent on $\dot{\mathbf{q}}$. By replacing the dependency on the generalized velocities with upper limits related to the saturation of the motor velocities, the expression could be improved. However, by enforcing a value of ρ that fulfills the given inequality, the derivative of the Lyapunov function candidate is negative definite, and stability is proven with the suggested control law

$$\dot{\mathbf{V}}(\boldsymbol{\xi}) = -\boldsymbol{\xi}^T\mathbf{P}\boldsymbol{\xi} + 2\mathbf{z}^T(\mathbf{J}\boldsymbol{\eta} - \frac{\rho}{||\mathbf{z}||}\mathbf{z}) < 0, \quad \forall\ \boldsymbol{\xi} \neq \mathbf{0} \tag{C.29}$$

Nicolas Fredhall Holguin

Rigid body modeling and motion control of offshore cranes performing heavy lift operations

NTNU
Norwegian University of
Science and Technology